AD-A279 871

2

WL-TR-93-4125

EDDY CURRENT FOR DETECTING SECOND-
LAYER CRACKS UNDER INSTALLED FASTENERS

GARY L. BURKHARDT   EDITH A. CREEK
ROBERT E. BEISSNER   JAY L. FISHER

SOUTHWEST RESEARCH INSTITUTE
P.O. DRAWER 28510
SAN ANTONIO, TX 78228-0510

FEBRUARY 1994

FINAL REPORT FOR 09/30/91–10/31/93

DTIC
ELECTE
S   D
JUN 03 1994
F

APPROVED FOR PUBLIC RELEASE; DISTRIBUTION IS UNLIMITED.

94–16501

94 6 2 076

NOTICE

WHEN GOVERNMENT DRAWINGS, SPECIFICATIONS, OR OTHER DATA ARE USED FOR ANY PURPOSE OTHER THAN IN CONNECTION WITH A DEFINITELY GOVERNMENT-RELATED PROCUREMENT, THE UNITED STATES GOVERNMENT INCURS NO RESPONSIBILITY OR ANY OBLIGATION WHATSOEVER. THE FACT THAT THE GOVERNMENT MAY HAVE FORMULATED OR IN ANY WAY SUPPLIED THE SAID DRAWINGS, SPECIFICATIONS, OR OTHER DATA, IS NOT TO BE REGARDED BY IMPLICATION OR OTHERWISE IN ANY MANNER CONSTRUED, AS LICENSING THE HOLDER OR ANY OTHER PERSON OR CORPORATION, OR AS CONVEYING ANY RIGHTS OR PERMISSION TO MANUFACTURE, USE, OR SELL ANY PATENTED INVENTION THAT MAY IN ANY WAY BE RELATED THERETO.

THIS REPORT IS RELEASABLE TO THE NATIONAL TECHNICAL INFORMATION SERVICE (NTIS). AT NTIS, IT WILL BE AVAILABLE TO THE GENERAL PUBLIC, INCLUDING FOREIGN NATIONS.

THIS TECHNICAL REPORT HAS BEEN REVIEWED AND IS APPROVED FOR PUBLICATION.

LAURA L. MANN
Nondestructive Evaluation Branch
Metals and Ceramics Division
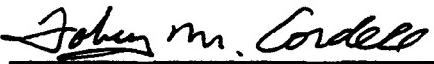
TOBE' M. CORDELL, Chief
Nondestructive Evaluation Branch
Metals and Ceramics Division

NORMAN M. GEYER, Acting Asst Chief
Metals and Ceramics Division
Materials Directorate

IF YOUR ADDRESS HAS CHANGED, IF YOU WISH TO BE REMOVED FROM OUR MAILING LIST, OR IF THE ADDRESSEE IS NO LONGER EMPLOYED BY YOUR ORGANIZATION, PLEASE NOTIFY, WL/MLLP, WRIGHT-PATTERSON AFB OH 45433-7817 TO HELP US MAINTAIN A CURRENT MAILING LIST.

COPIES OF THIS REPORT SHOUL.D NOT BE RETURNED UNLESS RETURN IS REQUIRED BY SECURITY CONSIDERATIONS, CONTRACTUAL OBLIGATIONS, OR NOTICE ON A SPECIFIC DOCUMENT.

REPORT DOCUMENTATION PAGE

Form Approved
OMB No. 0704-0188

1. AGENCY USE ONLY (Leave blank)	2. REPORT DATE	3. REPORT TYPE AND DATES COVERED
	February 1994	Final Report, 9/30/91 to 10/31/93

4. TITLE AND SUBTITLE

Eddy Current for Detecting Second-Layer Cracks Under Installed Fasteners

5. FUNDING NUMBERS

C   F33615-91-C-5661
PE 62102F
PR 2418
TA 02
WU 51

6. AUTHOR(S)

Gary L. Burkhardt   Edith A. Creek
Robert E. Beissner   Jay L. Fisher

7. PERFORMING ORGANIZATION NAME(S) AND ADDRESS(ES)

Southwest Research Institute
6220 Culebra Road
San Antonio, Texas 78238-5166

8. PERFORMING ORGANIZATION REPORT NUMBER

17-4665

9. SPONSORING/MONITORING AGENCY NAME(S) AND ADDRESS(ES)

Materials Directorate
Wright Laboratory
WL/MLLP
Wright-Patterson AFB, Ohio 43433-6533

10. SPONSORING/MONITORING AGENCY REPORT NUMBER

WL-TR-93-4125

11. SUPPLEMENTARY NOTES

12a. DISTRIBUTION/AVAILABILITY STATEMENT

Approved for public release;
distribution unlimited.

DTIC QUALITY INSPECTED 2

12b. DISTRIBUTION CODE

A

13. ABSTRACT (Maximum 200 words)

Southwest Research Institute developed an eddy current (EC) laboratory breadboard inspection system to detect second-layer cracks around installed fasteners in two-layer airframe structures with the probe positioned on the first layer (outside surface). Probe design considered both cup- and segment-core configurations as exciter coils and various orientations and positions of sensor coils. Highest sensitivity was obtained with a segment-core exciter covering an 85-degree segment with the sensor oriented normal to the specimen surface and placed near the core outer leg. EC data were presented in two-dimensional color images. The goal of detecting a 2.5-mm second-layer flaw through a first-layer thickness of 6.4 mm was achieved in eight of nine specimen configurations which contained simulated cracks. The specimens included structure geometries containing second-layer edges, first-layer edges, adjacent fasteners, different fastener sizes, different flaw orientations around the hole, and fasteners of different materials (titanium and steel). In fatigue crack specimens supplied by WL/MLLP, where adjacent fasteners were spaced more closely and caused interfering signals, flaw detection was more difficult; however, a 2.5-mm flaw was detected through a 4.5-mm first layer by comparing the signal patterns from adjacent holes.

14. SUBJECT TERMS

Aircraft, fastener hole, two-layer structure, wing, eddy current, nondestructive inspection.

15. NUMBER OF PAGES

110

16. PRICE CODE

17. SECURITY CLASSIFICATION OF REPORT	18. SECURITY CLASSIFICATION OF THIS PAGE	19. SECURITY CLASSIFICATION OF ABSTRACT	20. LIMITATION OF ABSTRACT
Unclassified	Unclassified	Unclassified	

NSN 7540-01-280-5500

Standard Form 298 (Rev. 2-89)
Prescribed by ANSI Std. Z39-18
298-102

EXECUTIVE SUMMARY

BACKGROUND OF THE PROBLEM

Detection of second-layer cracks around fastener holes in two-layer airframe structures is a high-priority need of the United States Air Force. The desired inspection mode is an eddy current approach that can be accomplished with the fasteners in place and that positions the probe on the outside surface of the first layer. This approach presents a challenging problem because second-layer cracks must be detected through the first layer, and the first layer attenuates the eddy currents. In addition, the geometrical configuration of the layers and of the subsurface structure complicates the inspection because they can result in signals that mask the flaw signals.

PROJECT OBJECTIVES

Southwest Research Institute was funded by the Air Force to address the problem by developing a second-layer inspection technique to be applied with the fasteners in place. The primary objectives were to (1) develop a laboratory breadboard eddy current inspection device for second-layer structure, (2) optimize the eddy current technique, and (3) demonstrate reliable detection of second-layer 2.54-mm radial-length, fastener-hole cracks in realistic airframe structure with a first-layer thickness of 6.35 mm.

TECHNICAL APPROACH

The technical approach involved (1) optimization of probe design using three-dimensional electromagnetic field models of probes, (2) investigation of probe excitation modes and signal processing to discriminate among flaw signals and structure noise, (3) application of two-dimensional scanning combined with color imaging of the data to allow spatial patterns of structural indications to be more easily separated from crack indications, (4) development of a laboratory breadboard inspection system for evaluation of the above approaches, and (5) evaluation of the breadboard using specimens typical of aircraft structure and containing common structural variations.

SCOPE OF WORK

Probe design considered both cup- and segment-core configurations as excitation coils and various orientations and positions of sensor coils with respect to the exciter. The highest sensitivity

to second-layer flaws and best discrimination among flaws and structure were obtained with a segment-core exciter with the outer leg of the core covering an 85-degree segment, along with a sensor oriented normal to the specimen surface and placed near the core outer leg. This probe was used in a mode where circumferential scans around the fastener were made at different radial positions to form a two-dimensional scan. Presentation of the data in two-dimensional color images improved discrimination among flaws and structure. An alternate approach using a symmetrical cup-core exciter and linear raster scans, combined with color imaging, showed potential for a rapid inspection that requires essentially no probe alignment. The sensitivity, however, is reduced compared to the circumferential scans.

CONCLUSIONS

In the breadboard evaluation, the project goal of detecting a 2.5-mm second-layer flaw through a first-layer thickness of 6.4 mm was achieved in eight of the nine specimen configurations evaluated with this layer thickness. The evaluation included structure geometries containing second-layer edges, first-layer edges, adjacent fasteners, different fastener sizes, different flaw orientations around the hole, and fasteners of different materials (titanium and steel). In the case of a first-layer edge, where detection of a 2.5-mm flaw was marginal, a 3.8-mm flaw was readily detectable. In specimens supplied by WL/MLLP, where adjacent fasteners were spaced more closely and caused interfering signals, a 2.5-mm flaw was detected through a 4.5-mm first layer by comparing the signal patterns from adjacent holes. In a similar specimen with a 6.9-mm first layer, a 2.5-mm flaw was not detected. Also, a 2.5-mm first-layer flaw was detected.

RECOMMENDATIONS

Results of the project demonstrated that detection of second-layer flaws using eddy current is feasible and can be applied to many aircraft structure configurations. It is recommended that the circumferential scan technique be validated on a larger specimen set consisting of actual aircraft structure and then developed into a field breadboard system. An improved multifrequency mixing approach and an improved probe design for magnetic fasteners should also be investigated. The feasibility of combining linear raster-scan technology for second-layer inspection with the McDonnell Douglas MAUS III system (currently being developed for WL/MLLP) should be investigated. This system could provide the mechanical scanning and possibly the instrumentation for implementation of a high-speed, second-layer linear raster-scan inspection.

TABLE OF CONTENTS

LIST OF FIGURES

LIST OF FIGURES (CONT'D)

PREFACE

Many of the figures used in this report were originally color images. The black and white reproduction process causes a loss of quality. Color copies of these figures may be obtained by contacting the contractor.

1. INTRODUCTION

1.1 BACKGROUND OF THE PROBLEM

The United States Air Force has an operational need to reliably detect second-layer cracks around fastener holes in two-layer airframe structures. Inspection techniques such as removal of the fastener and insertion of a rotating eddy current probe in the fastener hole or the use of radiography have significant disadvantages. Therefore, the Air Force has recognized the importance of developing an eddy current (EC) inspection that can be accomplished with the fasteners in place. This presents a difficulty because second-layer cracks must be detected through the first layer, and penetration through the first layer causes significant attenuation of the eddy currents. In addition, the geometry of the second layer and underside of the first layer are typically nonuniform in the region of the fasteners; these geometric variations complicate the inspection.

Typical configurations of two-layer aircraft structures, T-38 and C-5A wings, are shown in Figs. 1 and 2, respectively. The T-38 configuration is for the fastener connection between the skin and a spar, and the C-5A configuration is for a wing-skin splice joint. Many other configurations, some more complex, exist in these and other aircraft. The EC responses to structural features, such as those shown in these figures, typically limit the sensitivity of the EC inspection because they can produce large signals which mask or complicate the response from cracks. For example, the T-38 structure has a very significant change in first-layer thickness in the fastener regions; the edges of the second layer are also in this region. The C-5A structure has edges of both the first and second layers in proximity to the fastener; an integral rib in the second layer is also present. All of these features can result in large background signals. Other factors can also interfere with the inspection. These include the thickness of the layers, presence of adjacent fastener holes, type of fastener material, and size of the fastener.

1.2 PROJECT OBJECTIVES

The project had three objectives.

(1) Develop a laboratory breadboard EC inspection device.

(2) Optimize the EC technique for the inspection of second-layer structures while the fasteners are in place.

1
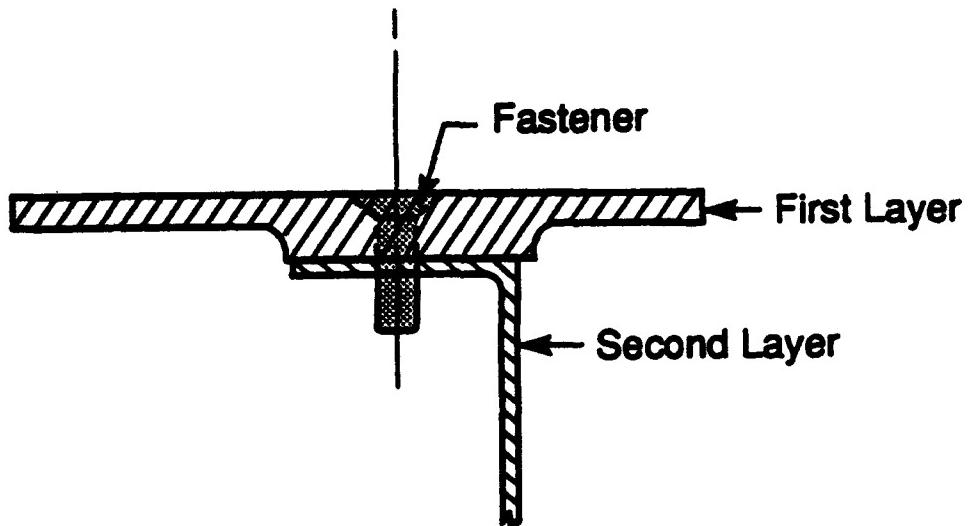
Figure 1. Typical T-38 two-layer wing-skin configuration.
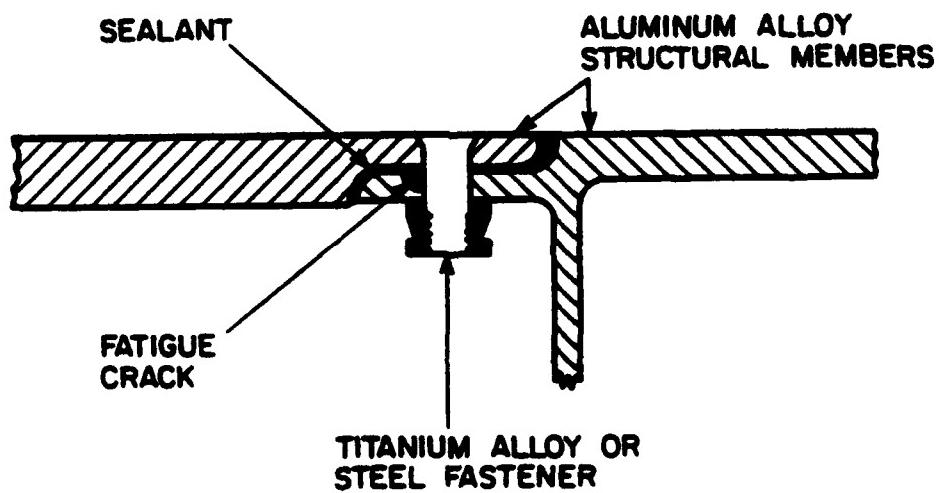
Figure 2. Typical C-5A two-layer structural fastener configuration.

(3) Reliably detect 2.54-mm radial length cracks emanating from the fastener hole in the second layer where the first-layer thickness is 6.35 mm.

The inspection had to be performed with a probe placed on the surface of the first layer and with the fastener in place. A crack at any angular location around the fastener hole also must be detected. Display of crack indications must include the angular position of the crack, depth of the crack in the structure, and layer in which the crack is located; and the display should be shown in real time. In order to accomplish these objectives in actual aircraft structures, the EC inspection system had to suppress the variations in EC response caused by nonrelevant background sources, which can strongly interfere with flaw detection. These sources include the shape of the structure; the presence of first- and second-layer edges and ribs or spars in the second layer; variations in the thicknesses of both layers; and variations in the distance between fastener holes, in the distance between the holes and the edge of the layers, and in the hole diameters. In addition, the system must be able to compensate for the differences in sensitivity caused by different fastener materi: : (e.g., steel, aluminum, and titanium).

1.3 TECHNICAL APPROACH

The technical approach employed the following five elements given in 1.3.1 through 1.3.5.

1.3.1 <u>Development of Three-Dimensional Electromagnetic Field Models of Probes</u>—To ensure the best signal-to-background ratio, it was essential that the exciter and sensor be optimized for second-layer crack detection. This was accomplished using a computer model to study exciter core configurations and sizes, sensor location and orientation, and excitation frequencies.

1.3.2 <u>Investigation of Probe Excitation Modes</u>—Probe excitation modes were investigated for obtaining multiple-frequency data. These included time-dependent frequency (chirp) and multiple, discrete-frequency excitation. [Previous work showed that multifrequency as well as pulsed data can be easily realized by chirp waveform excitation (1,2).] The multiple-frequency data from the excitation modes were coupled with computerized multifrequency mixing. Multifrequency excitation and mixing takes advantage of the frequency-dependent penetration of ECs into the structure. The low-frequency signals are necessary to penetrate into the second layer to detect flaws, but they also are sensitive to first-layer structure and to other variables such as off-centering of the probe (for circumferential scans). The high-frequency signals do not penetrate into the second layer, so they contain only the first layer and other (e.g., off-centering) responses. Computer mixing of these

3

signals can help remove the responses contained in the high frequency from those in the low frequency and, thus, can help remove extraneous signals.

1.3.3 Application of Two-Dimensional Scanning Combined with Color Imaging—Although structure and other extraneous signals can be reduced by probe design and mixing, they cannot be eliminated. An imaging technique, therefore, was used that allows tolerance of structural indications. This approach relies on two-dimensional scanning and presents the data in a two-dimer al, color image. The image allows spatial patterns of structural indications to be more easily se d from crack indications than if only one-dimensional data (e.g., from a single scan around the fastener) were presented.

1.3.4 Development of a Laboratory Breadboard Inspection System for Evaluation of the Approach—A laboratory breadboard system consisting of probes, instrumentation, and mechanical scanner was developed. Probes were designed based on the computer model. The instrumentation consisted primarily of existing laboratory equipment, and the computer-controlled scanner was based on existing equipment modified as required.

1.3.5 Evaluation of the Breadboard Using Specimens Typical of Aircraft Structure and Containing Typical Structural Variations—The breadboard system was optimized and evaluated using specimens typical of aircraft structure. The specimens included structural variables such as first- and second-layer edges, adjacent fasteners, fasteners of different sizes, fasteners of different materials (titanium and steel), and different flaw orientations with respect to edges.

2. MODELING

The purpose of the modeling was to

(1) Define a probe configuration (excitation coil and sensor) that maximized the signal from a second-layer flaw while minimizing unwanted signals from surrounding structure such as first- and second-layer edges and

(2) Determine optimum excitation frequencies and method of excitation.

A commercially available, three-dimensional, finite-element computer program (Electromagnetic Analysis System from MacNeal-Schwendler Corp.) was leased and installed on a Sun-4 workstation for modeling calculations. Details of the modeling are described in section 2.1 for probe design and 2.2 for frequency determination.

2.1 PROBE DESIGN

The probe configuration consisted of an exciter to induce eddy currents in the structure and a sensor to detect variations in the eddy current flow caused by flaws. The objectives of the exciter design were (1) to obtain a high current density in the second layer because the flaw signal is proportional to the current density and (2) to confine the current to an area immediately adjacent to the fastener and away from edges in the structure to reduce the response from the structure. The objectives of the sensor design were to determine the optimum sensor location and orientation to maximize the flaw response and minimize the structure response. The probe design considered the following items:

(1) Comparison of axisymmetric (cup-core) and nonaxisymmetric (segment-core) exciter configurations

(2) Variations in the radial and arc lengths of the segment-core arm

(3) Response from a crack in the second layer

(4) Response from second-layer geometry (presence of a second-layer edge)

5

(5) Sensor position and orientation

(6) Type of fastener material (magnetic or nonmagnetic)

2.1.1 Exciter—The exciter consisted of a coil and a magnetic (ferrite) core. Both axisymmetric (cup-core) and nonaxisymmetric (segment-core) configurations were considered in the model. The model geometries for both cores are shown in Fig. 3 along with simple wing-structure geometry. Views in the figure are for a slice through the cross section, so only half of the probe and structure geometry is shown. Initially, titanium fastener material was used; for the segment core, an initial arc length of 45 degrees was selected. In the figure, blue represents the core; yellow, the coil; orange, the fastener; and green, the wing structure. Fig. 4 shows the physical dimensions used in the model.

Fig. 5 shows the current distributions (frequency of 500 Hz) in the structure, with red equal to the highest current density and magenta the lowest. The cup core gives a larger region of high current density near the surface (red area). The segment core produces a current density that falls off less with depth. (At the bottom of the structure near the fastener, the current density with the cup core has decreased to dark green; the segment core has only decreased to light green.) This current-density distribution suggests that the segment core will provide a better response from cracks in the second layer.

For radial distances further from the fastener (e.g., under the outer leg of the core), current densities in the second layer are about the same (dark green) for both core types, so the presence of second-layer structure (e.g., an edge) in this region would produce about equal responses. The segment core produces a localized region of high current density in the circumferential direction compared to the cup core, which produces high current density around the entire fastener circumference. For circumferential scanning of the probe, therefore, the segment core will produce a more localized flaw response. For these reasons, the segment core should produce a stronger, more localized flaw response compared to the cup core, without a penalty of an increased response from second-layer structure. Thus, the segment-core configuration was selected for further modeling.

Additional modeling of the segment core involved variations in the radial length and angular width of the outer arm of the core. Figs. 6 and 7 show the results for arms having the maximum and minimum radial lengths (dimension L in Fig. 4 of 4.0 and 10.4 mm, respectively) considered in the study; both arms in this case have an angular width of 45 degrees (again, only half of

6
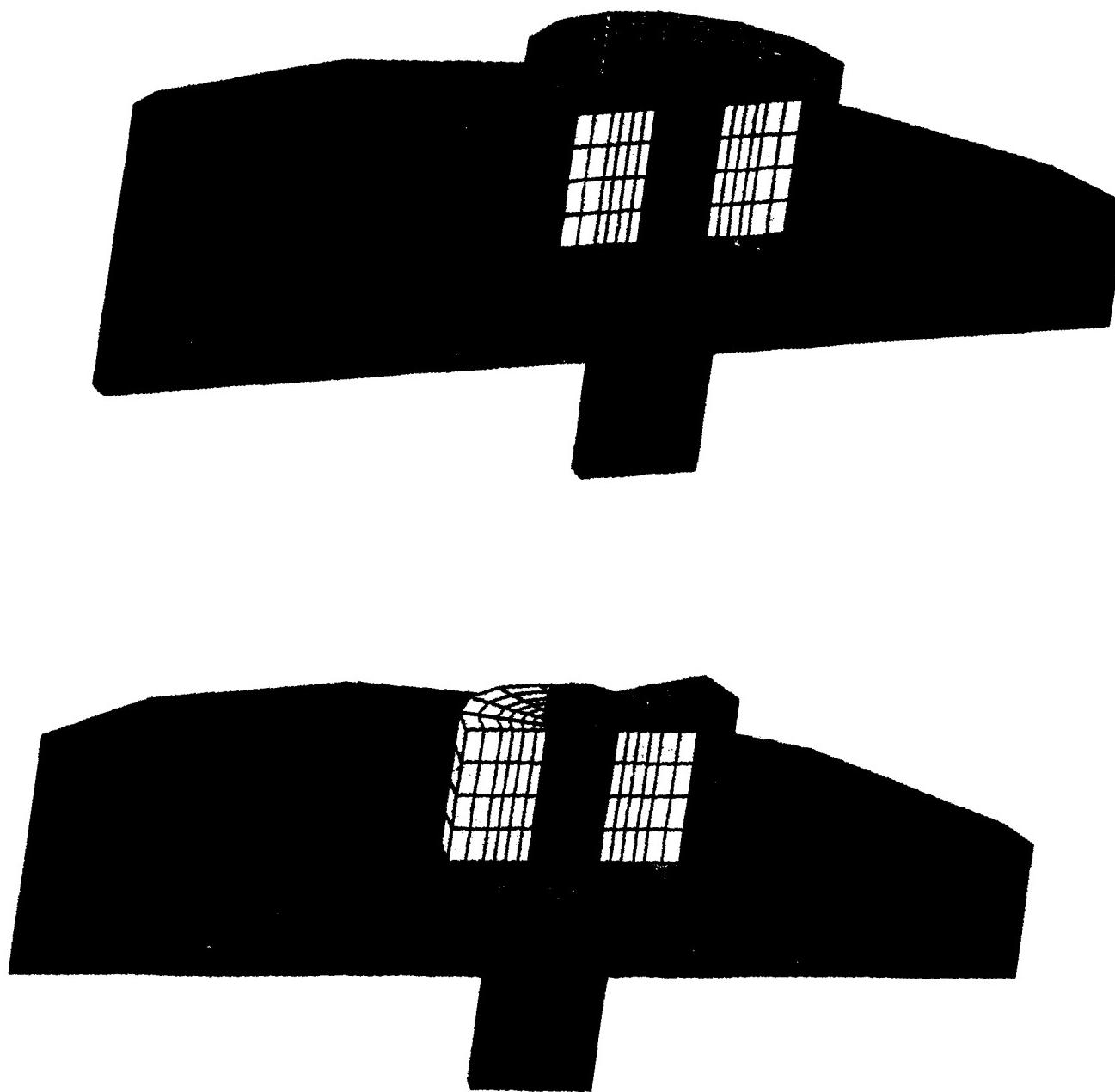
Figure 3. Finite-element model for cup (top) and 45-degree segment (bottom) core probes with simple geometrical structure. Components are designated by colors as follows: blue-core, yellow-coil, orange-fastener, green-structure.

(NOTE: COLOR COPY AVAILABLE FROM CONTRACTOR)
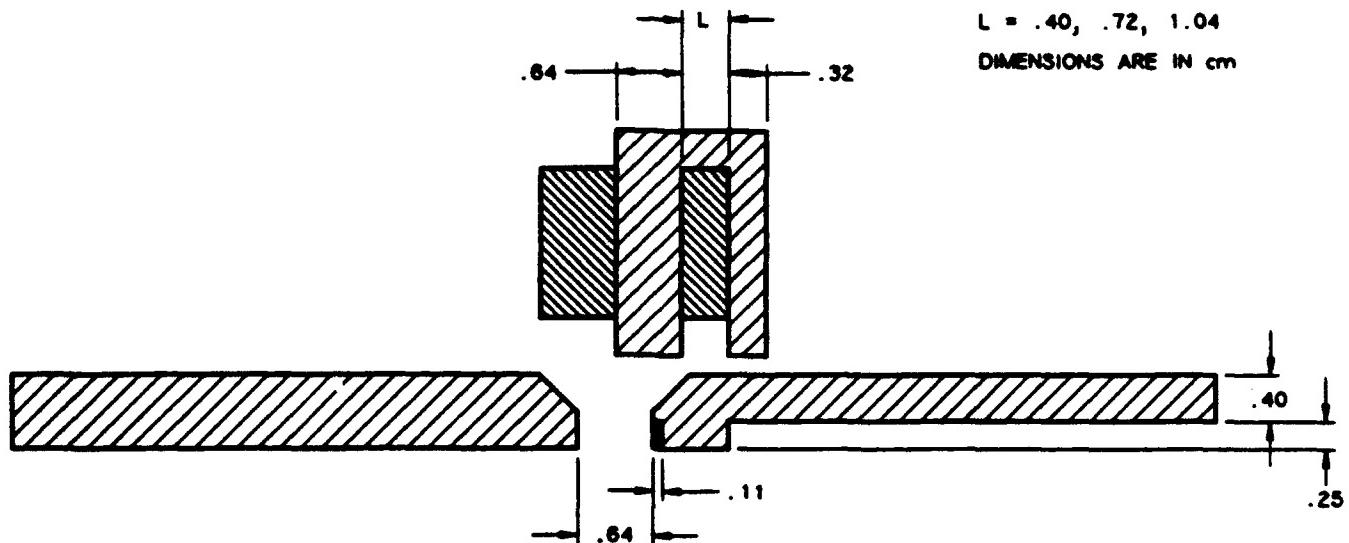
Figure 4. Physical dimensions of the probe and structure used in the model.

the probe is shown in the plots). The shorter core (Fig. 7) produces a higher current density near the fastener that is deeper within the structure compared to the longer core (Fig. 6). Note that the region of medium current density (yellow) extends to the bottom of the structure for the short arm, where the long arm only produces a smaller current density, as represented by light green in the same area. Thus, the shorter arm should produce a stronger signal from flaws in this area compared to the long arm. In addition, the radial extent of the current is less for the short arm, which should reduce the response from structure.

Fig. 8 shows the current-density calculations for the short arm length, but with the angular width increased from 45 to 90 degrees. The 90-degree width produces a somewhat broader region of high current density in the angular direction, but a higher current density deeper within the skin than did the 45-degree width. The moderately high current-density region (orange) extends to the bottom of the layers for the 90-degree segment, but ends well below the bottom for the 45-degree segment. No angular widths greater than 90 degrees were modeled because this would have extended the high current-density region over a larger angle, thus resulting in a broader response from

8
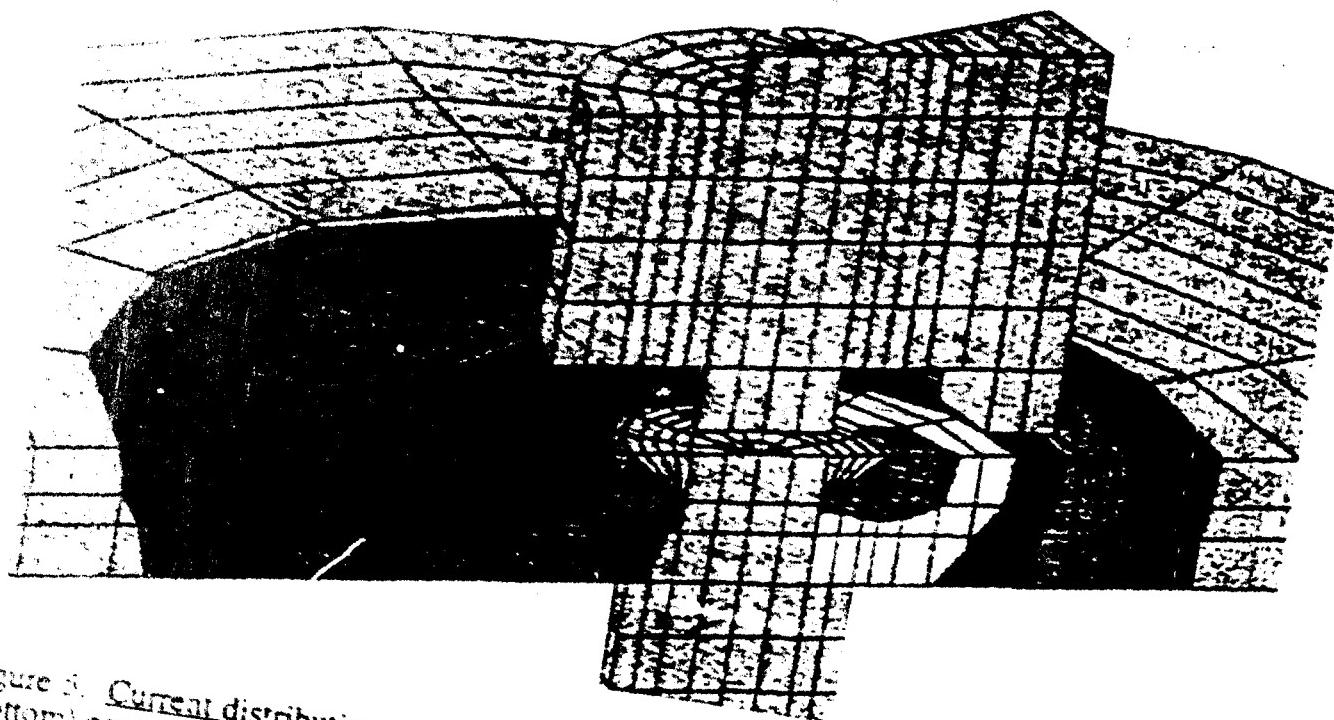
Figure 5. Current distributions in a structure (frequency of 500 Hz) for cup (top) and segment (bottom) cores. Red is highest current density and magenta is lowest.

(NOTE. COLOR COPY AVAILABLE FROM CONTRACTOR)

9
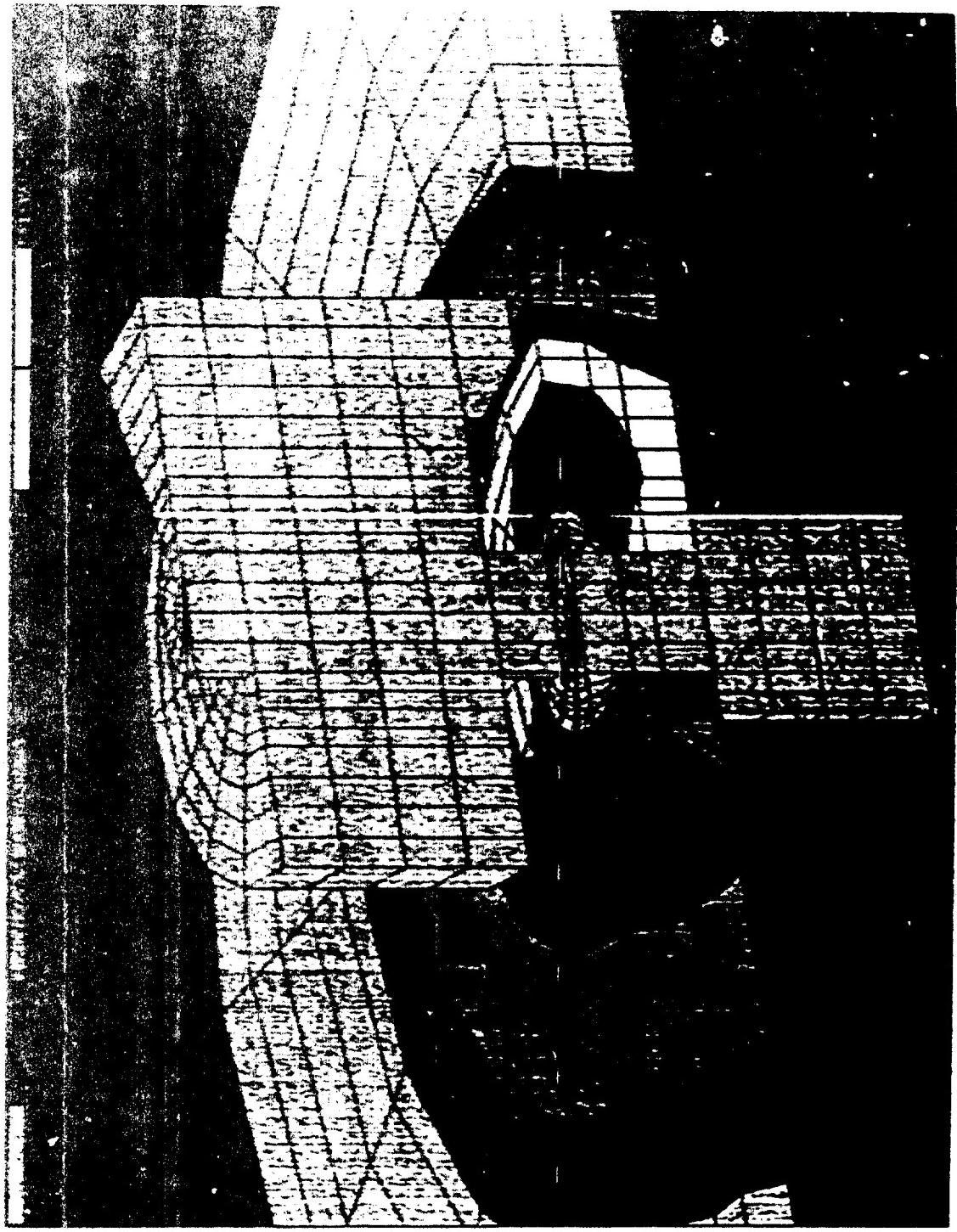
Figure 6. Current-density contour plot for a 45-degree segment-core probe with the segment arm at its maximum radial length. The maximum current density in the red region is 3.9×10^5 A/m²; the minimum current density in the magenta region is 3.9×10^4 A/m²; each color represents a current-density range of approximately 4×10^4 A/m².

(NOTE: COLOR COPY AVAILABLE FROM CONTRACTOR)
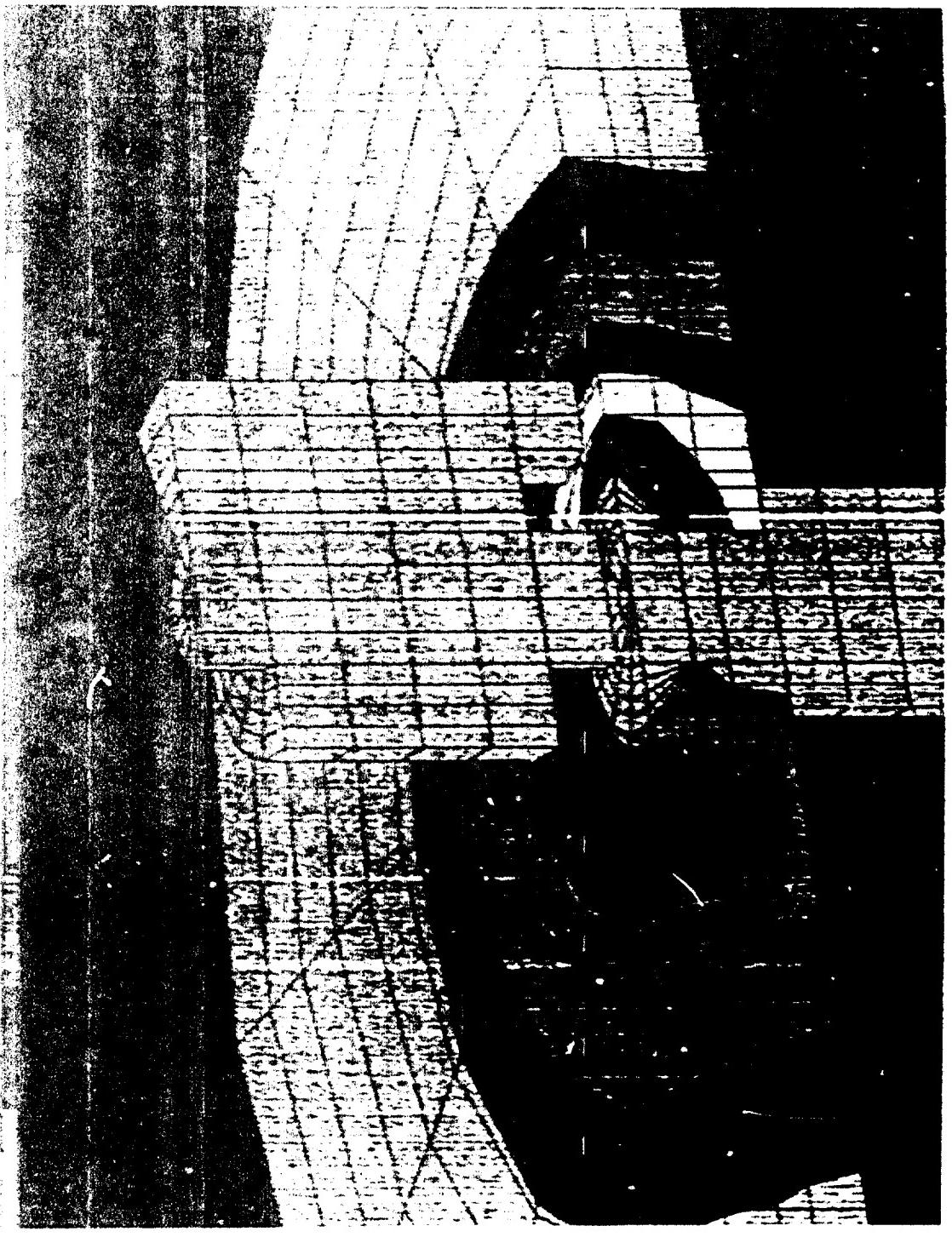
Figure 7. Current-density contour plot for a 45-degree segment core probe with the segment arm at its minimum radial length. The maximum current density in the red region is 3.8×10^6 A/m²; the minimum current density in the magenta region is 3.8×10^4 A/m²; each color represents a current-density range of approximately 4×10^4 A/m².

Figure 8. Current-density contour plot for a 90-degree segment-core probe with the segment arm at its minimum radial length. The maximum current density in the red region is 5.1×10^{5} A/m²; the minimum current density in the magenta region is 5.1×10^{4} A/m²; each color represents a current-density range of approximately 5×10^{4} A/m².

(NOTE: COLOR COPY AVAILABLE FROM CONTRACTOR)

12

the flaw as the probe was scanned circumferentially. Based on these results, a core having a short arm length and an angular width of 90 degrees was determined to be the best choice for an exciter design, with a core having a width of 45 degrees a secondary choice.

Exciter models were also performed using a steel fastener, which is ferromagnetic. Fig. 9 is the current-density plot for the same probe configuration and excitation frequency as in Fig. 7. Comparison of these two figures shows that the use of a magnetic fastener causes a major change in the current distribution. This happens because the magnetic fastener provides a low reluctance path for the magnetic flux leaving the central core of the probe. Flux is conducted down through the fastener and then up around the edges of the fastener and back to the probe. This produces a current density that is more uniformly distributed around the fastener than was the case with a nonmagnetic fastener.

Fig. 10 is another view of the same calculation with the probe and fastener removed so that the current density on the inside of the fastener hole can be seen. The unexpected result shown here is that the magnetic fastener causes the current density to peak away from the segment-core arm and away from the crack region. If, therefore, the segment-core probe is used with a magnetic fastener, the signal should be influenced more by the unflawed area around the fastener in the first layer than by a crack under the segment-core arm and at the bottom of the second layer.

A new probe configuration was investigated in an attempt to improve the situation with magnetic fasteners. The probe shown in Fig. 11 is a shielded version of the basic segment-core design. Ferrite shielding was added across the top of the probe and around the sides except for an air gap near the top. Additional shielding was added on the bottom except for the region next to the arm. The idea was to shunt the flux from the central core to the outside shield, thus preventing induction in the magnetic fastener except under the segment-core arm. The partial air gap near the top is intended to force more flux through the arm and down into the crack region.

Current-density plots for the shielded segment-core probe are shown in Figs. 12 and 13. The ferrite shielding served its intended purpose, as the current density now peaks in the crack region and falls off rapidly away from the crack region. A price is paid, however, for this improved localization of the current density. The peak current density with the shielded probe is reduced by about a factor of 3 relative to the unshielded probe, which would reduce the flaw response. Also, when the shielded probe is used with a nonmagnetic fastener, the current magnitude and localization
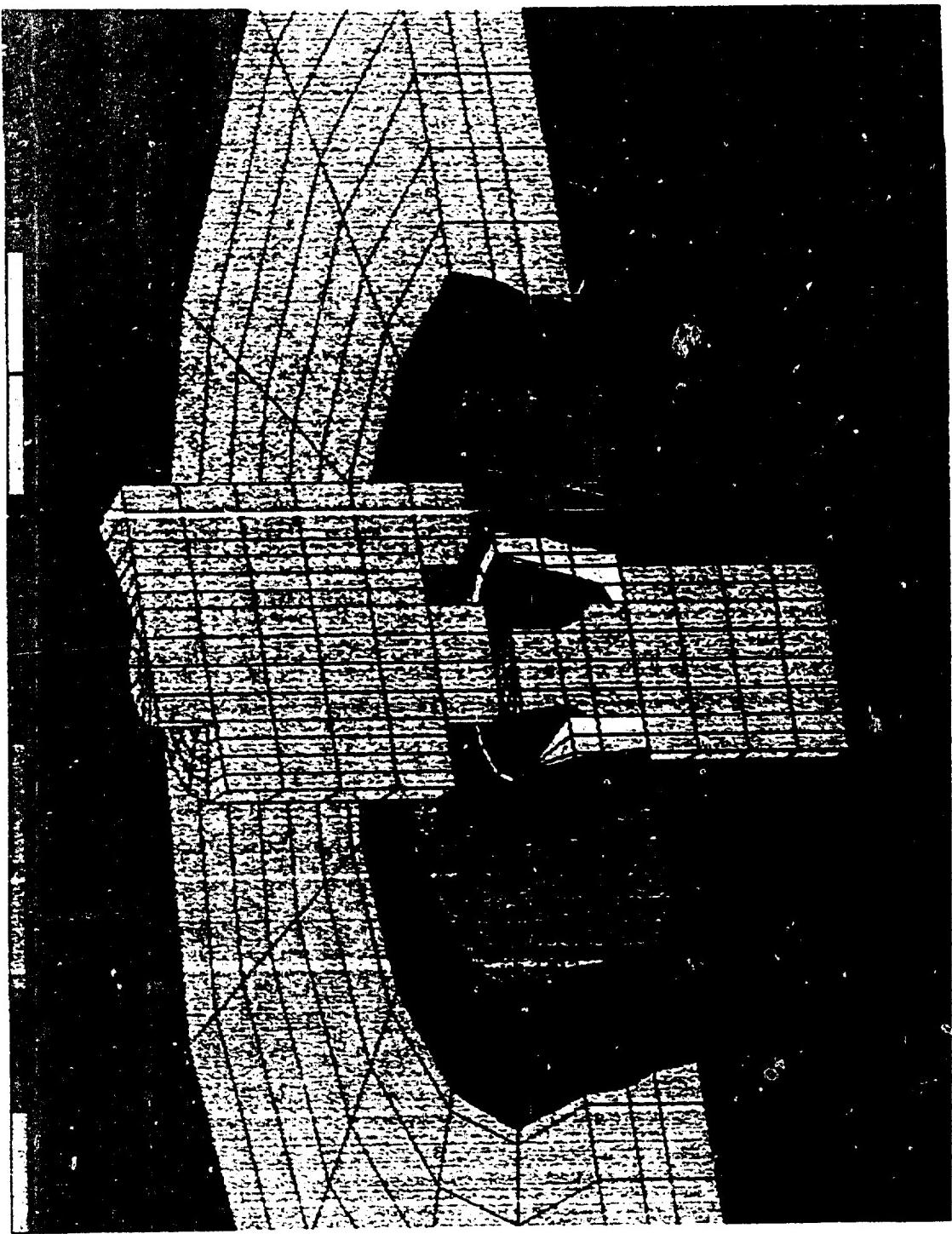
Figure 9. Current-density contour plot with a magnetic steel fastener. The probe is the same as in Fig. 7. The maximum current density in the red region is 5.2×10^5 A/m²; the minimum current density in the magenta region is 5.2×10^4 A/m²; each color represents a current-density range of approximately 5×10^4 A/m².

(NOTE: COLOR COPY AVAILABLE FROM CONTRACTOR)

14
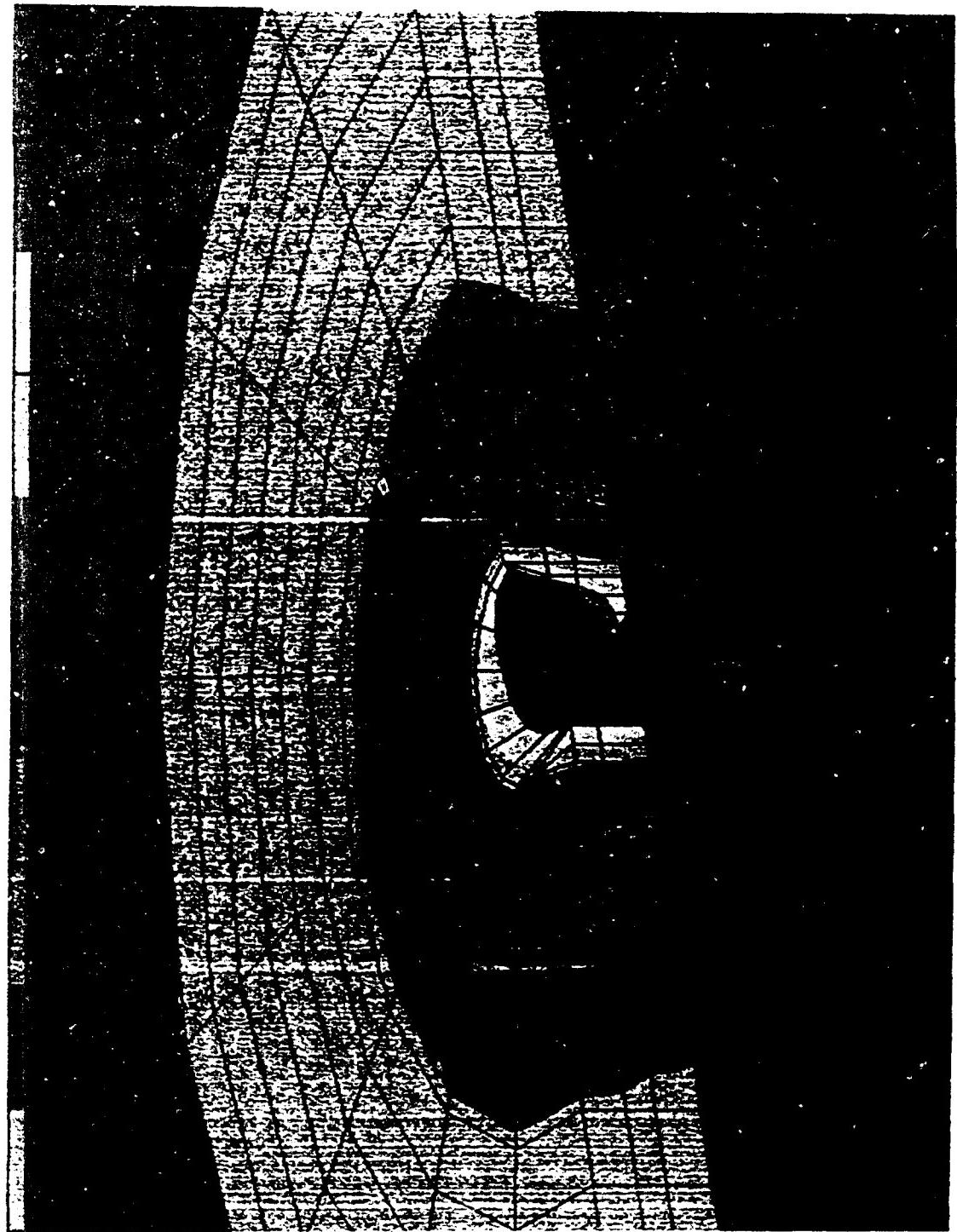
Figure 10. Current-density contour plot inside the fastener hole. Conditions are the same as in Fig. 9.
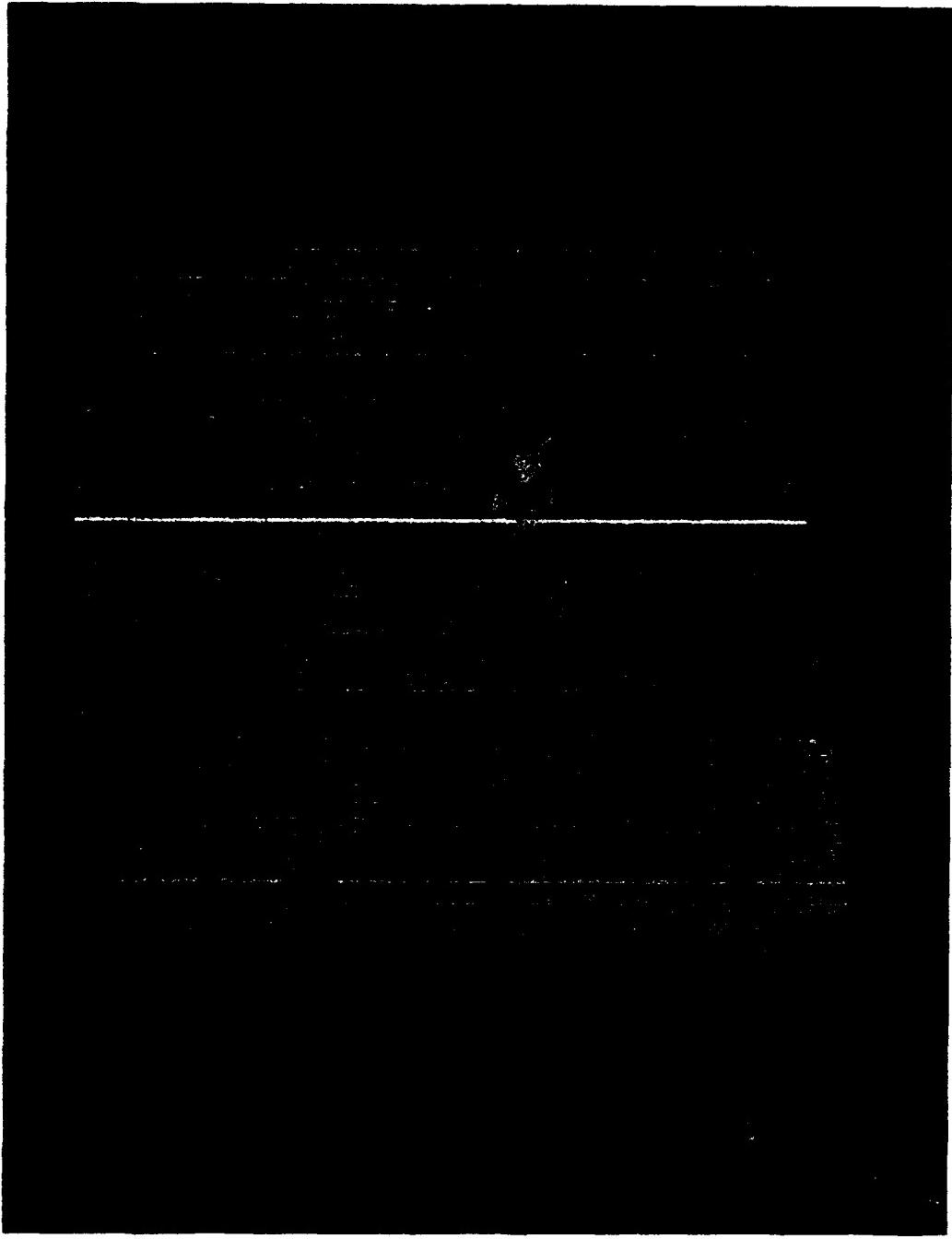
Figure 11a. Front view of the shielded segment-core probe for use with magnetic fasteners. Only half of the probe is shown.

(NOTE: COLOR COPY AVAILABLE FROM CONTRACTOR)

16
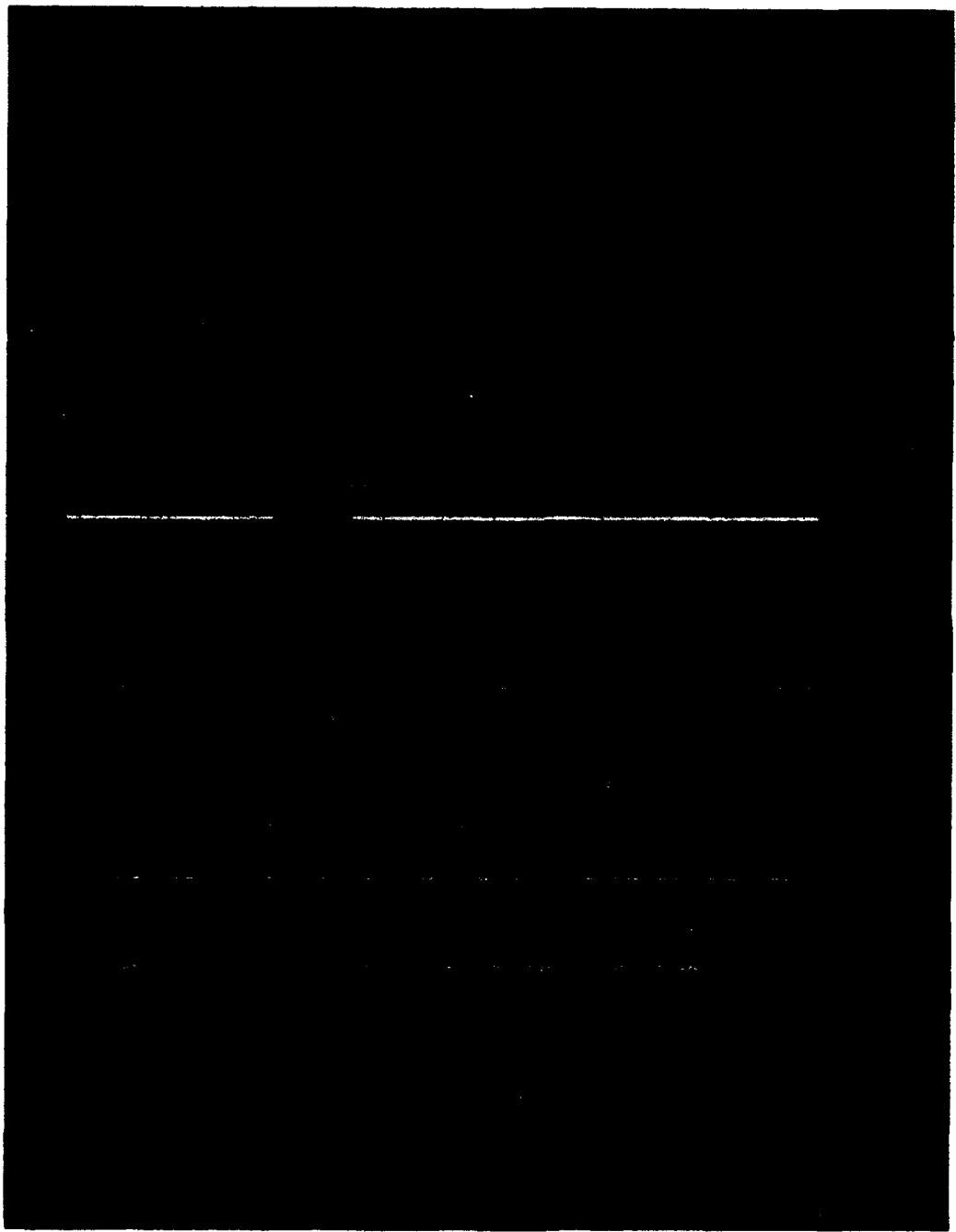
Figure 11b. Back view of the shielded segment-core probe for use with magnetic fasteners. Only half of the probe is shown.

(NOTE: COLOR COPY AVAILABLE FROM CONTRACTOR)

17
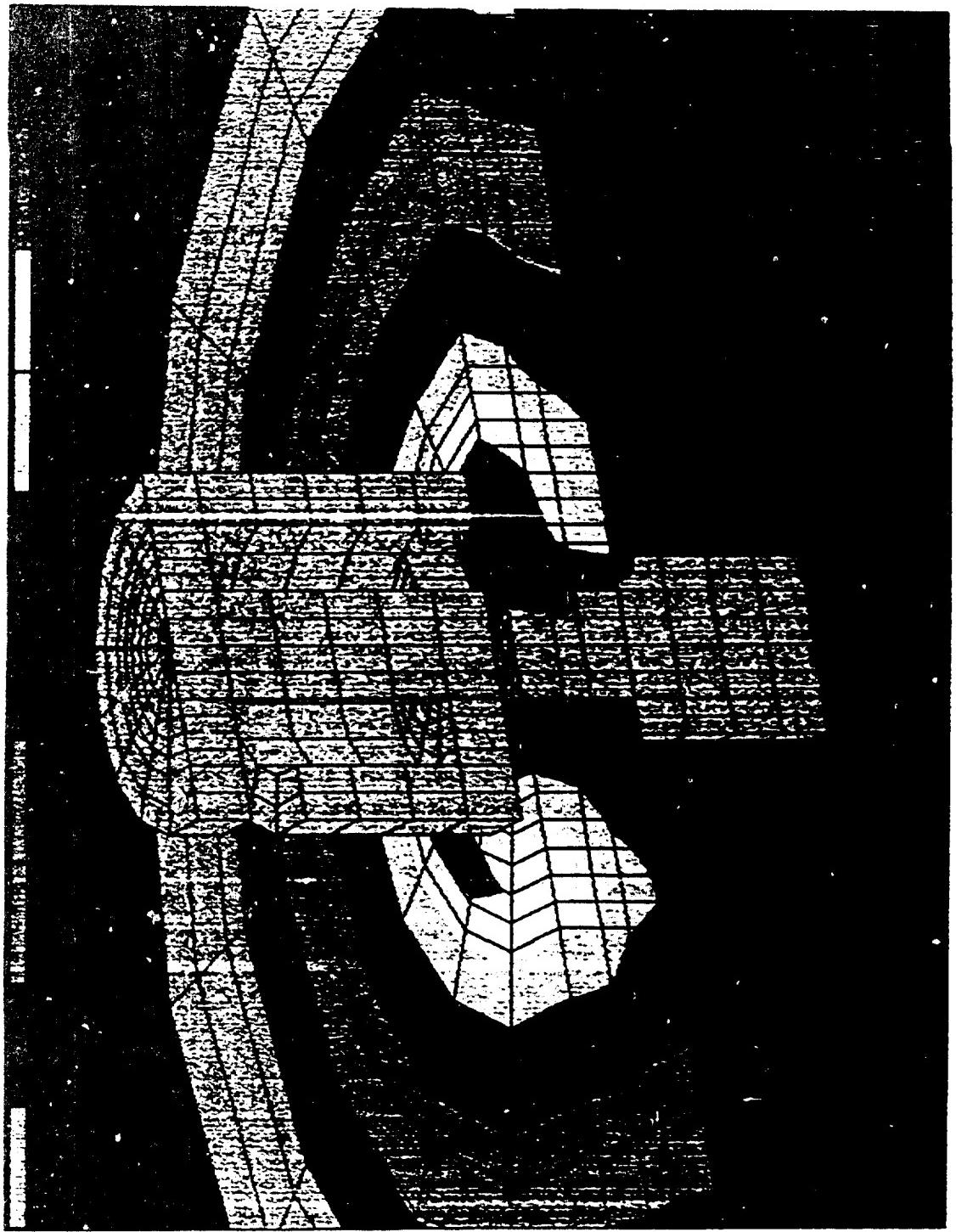
Figure 12. Current-density contour plot for a shielded segment-core probe with a magnetic steel fastener. The maximum current density in the red region is 1.5×10^6 A/m²; the minimum current density in the magenta region is 1.5×10^4 A/m²; each color represents a current-density range of approximately 2×10^4 A/m².

(NOTE: COLOR COPY AVAILABLE FROM CONTRACTOR)
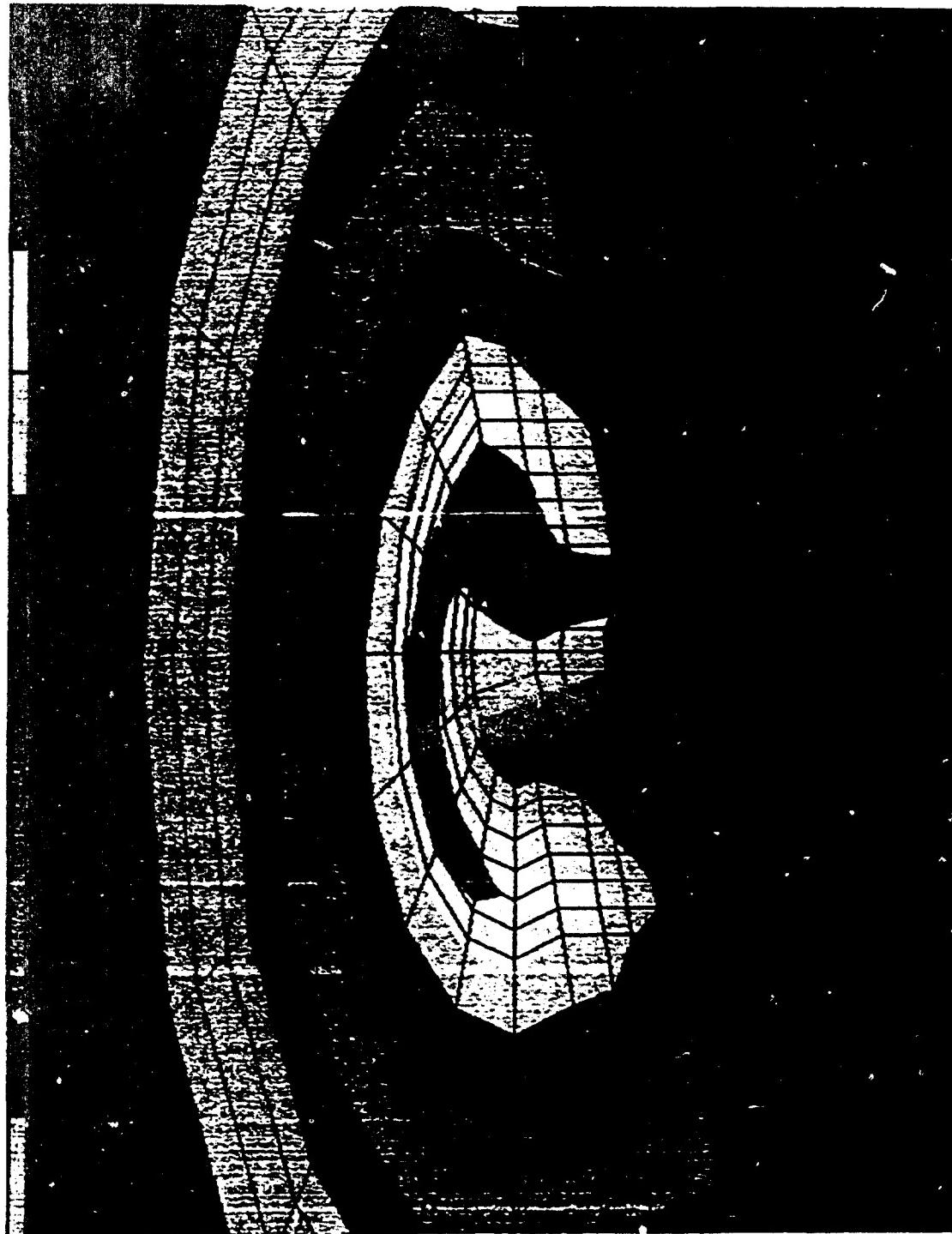
Figure 13. Current-density contour plot inside the fastener hole. Conditions are the same as in Fig. 12.

(NOTE: COLOR COPY AVAILABLE FROM CONTRACTOR)

are poorer than with the unshielded probe. In addition, the shielded coil is a difficult configuration to fabricate. Thus, while the shielded core offers some advantages, it also has some significant disadvantages, and testing would be required to determine how well it actually performs.

2.1.2 Sensor—Calculations were performed to determine the best orientation and position of the sensing coil with respect to the exciter for both cup- and segment-core configurations. This was done by determining the ratio of the flaw response with respect to the response from a second-layer edge for different sensor orientations and positions. The objective was to determine the best sensor placement by maximizing this ratio.

Fig. 14 shows the geometry for a second-layer edge, and Fig. 15 is an enlarged view of the geometry for a second-layer crack. Calculations were performed for the simple geometry (Fig. 3 bottom) and the geometries in Figs. 14 and 15 (frequency of 500 Hz). The purpose was to determine the current densities in the structure and the associated magnetic-field densities above the structure where the sensor would be located. Because the sensor output is proportional to the magnetic-field density, the field density is representative of signal levels from the flaw and structure. The field density was calculated at the positions shown by the red blocks in Fig. 16 to determine the effect of sensor radial position.

The response from the crack was determined by subtracting the flux density for the simple geometry (Fig. 3 bottom) from the geometry with the crack (Fig. 15). The response of the second-layer edge was determined in a similar manner [by subtracting the flux density for the simple geometry from the geometry with the second-layer edge (Fig. 14)]. Because the primary interest is in maximizing the crack signal with respect to the geometric signal, these data were used to compute a ratio of the flaw signal to the second-layer edge signal. These ratios are shown in Figs. 17 and 18 for the segment-core and cup-core configurations, respectively. These figures show the ratio vs. radial position of the sensor for both the vertical and radial components of the magnetic field. (Because of the low level of the circumferential component, meaningful results were not obtained for this component.)

For the segment core (Fig. 17), the maximum ratio was obtained with the radial component for sensor positions near the center portion of the core (small-sensor radial positions). The vertical component was relatively insensitive to sensor position, as the ratio was similar for all sensor positions. For the cup core (Fig. 18), the maximum ratio for the radial component was also
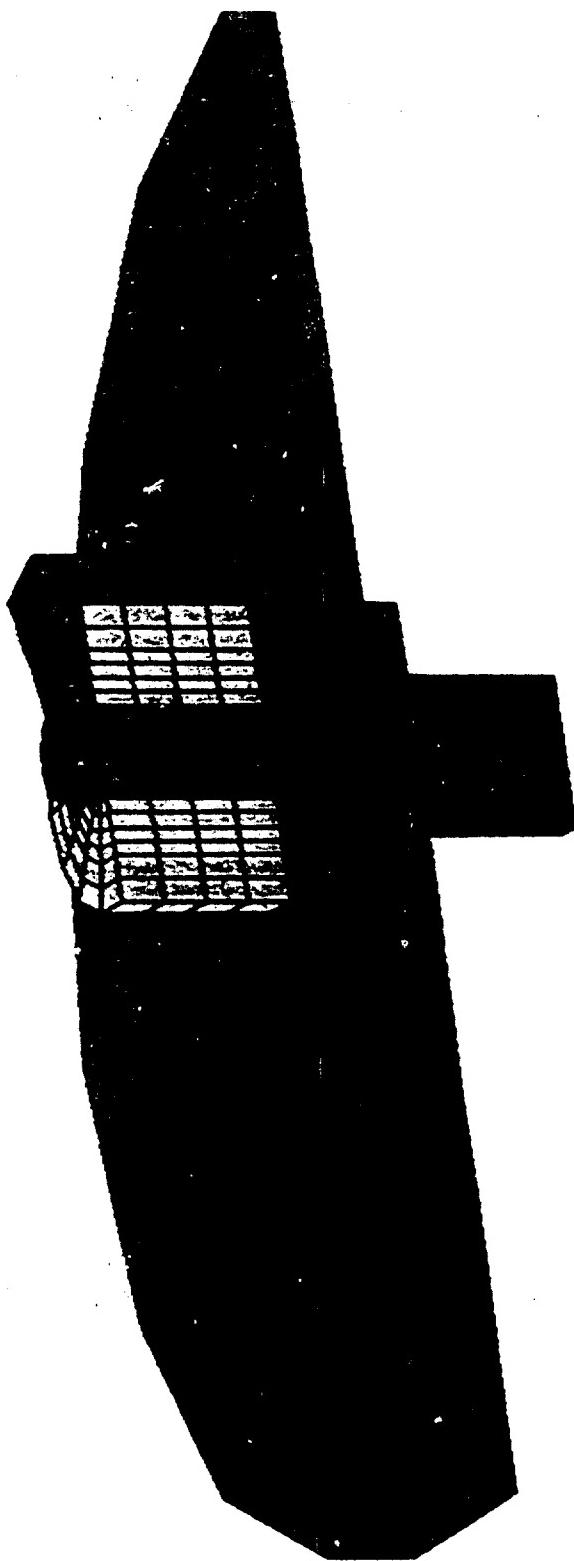
Figure 14. Finite-element model for a segment core and edge in second layer.
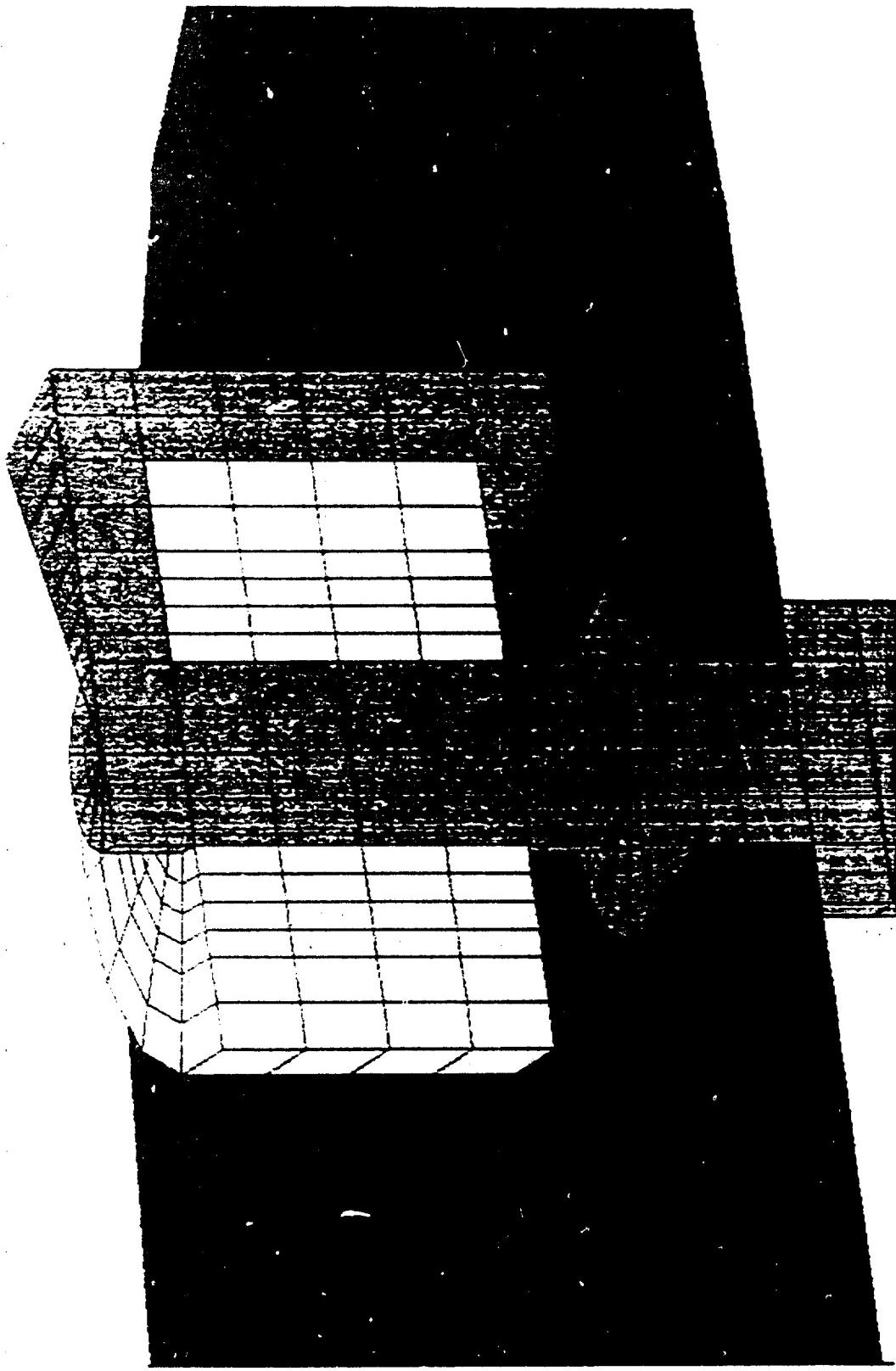
Figure 15. Finite-element model for a segment core and crack in second layer. Crack is represented by dark blue.
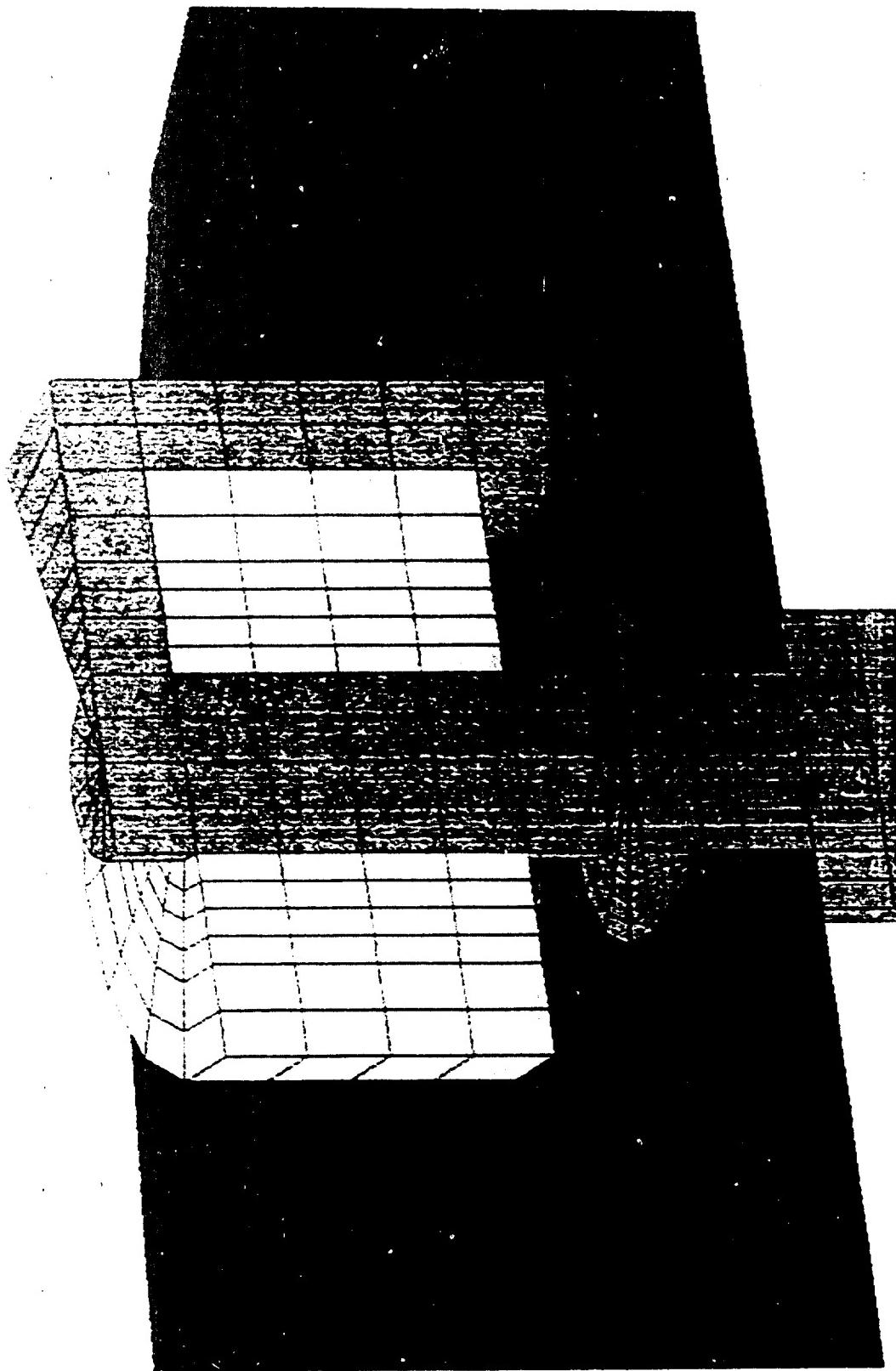
Figure 16. Finite-element model for a segment core showing sensor locations (red blocks).

(NOTE: COLOR COPY AVAILABLE FROM CONTRACTOR)

23
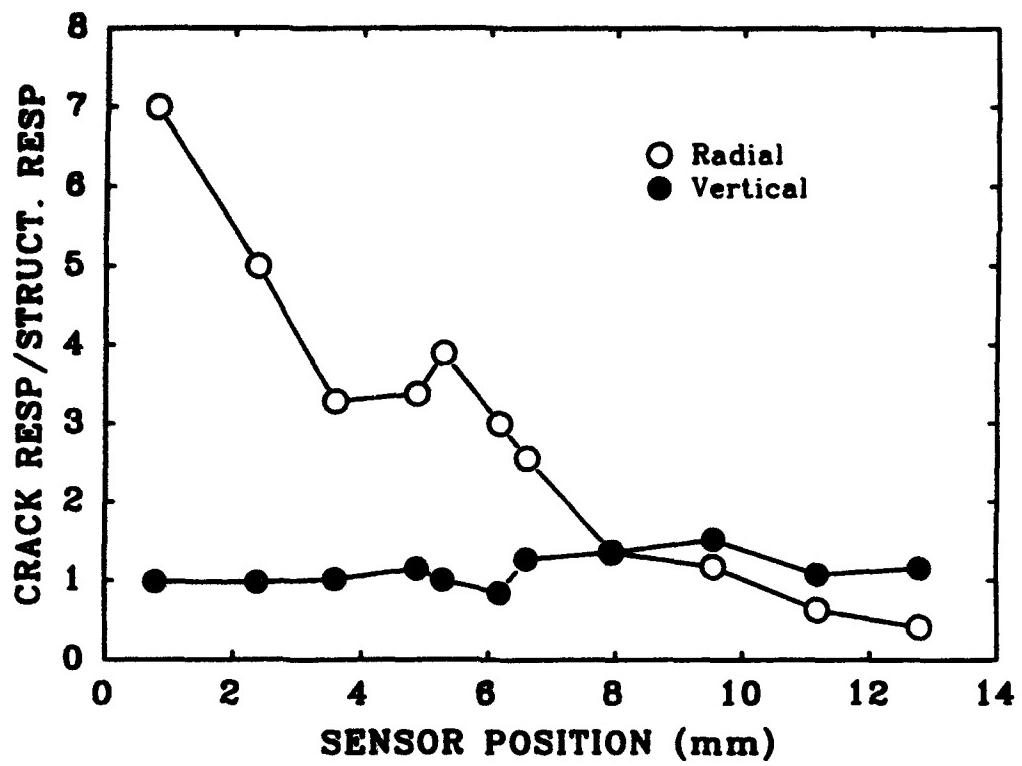
Figure 17. Ratio of crack response to structure response (edge in second layer) for 45-degree segment-core probe.
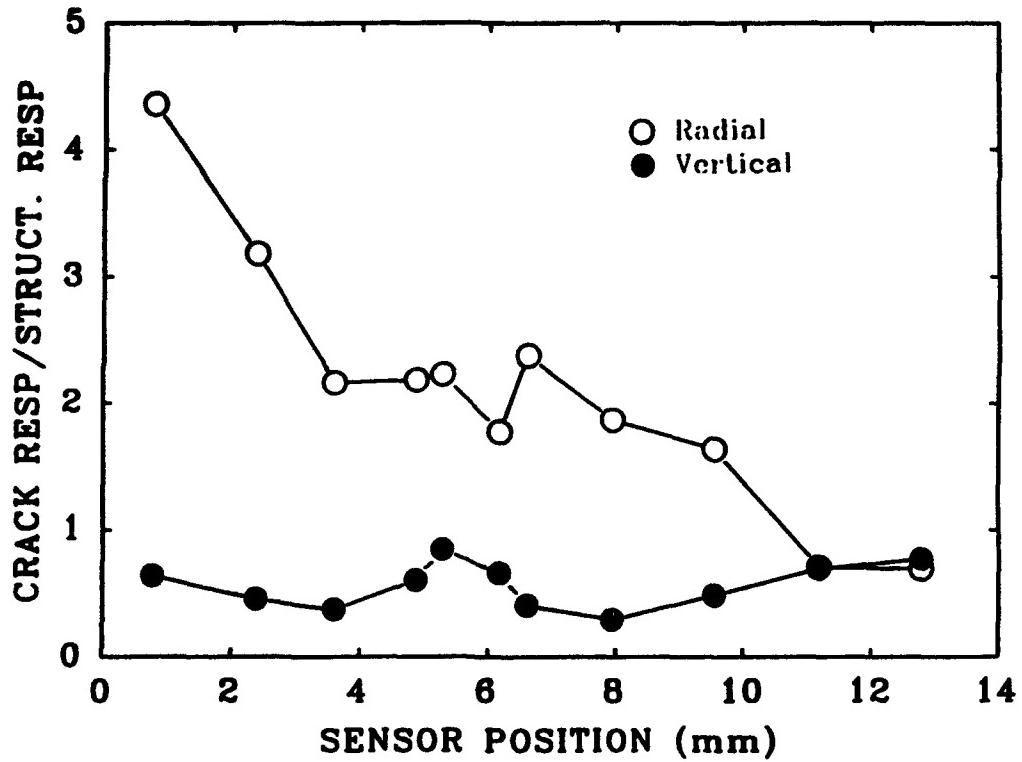
Figure 18. Ratio of crack response to structure response (edge in second layer) for cup-core probe.

24

obtained near the center portion of the core, but the ratios were somewhat smaller than for the segment core. This suggests that the segment core would provide somewhat better results than the cup core.

2.1.3 Excitation Frequency—The optimum excitation frequency range was determined by calculating the response from a crack as a function of frequency for different sensor orientations and positions. Figs. 19 and 20 illustrate the effect of varying the excitation frequency. The data plotted here are the changes in magnetic-flux density caused by the presence of a second-layer crack as a function of sensor position. The sensors are oriented so as to measure either the radial or vertical flux; sensors are positioned along the line from the center of the probe to the center of the segment-core arm, as indicated by the red areas in Fig. 16.

At lower frequencies, the radial flux component shown in Fig. 19 has a strong peak for sensor positions about 2 to 5 mm from the central core. The peak response for this sensor orientation is about 500 to 1000 Hz. At the highest frequencies (5000 and 10,000 Hz), the flaw signal is approximately zero, as expected, because the skin depth at these frequencies is too small to allow the field to penetrate to the flaw position.

Fig. 20 is a similar plot for the vertical flux. Once again, the maximum flaw signal is obtained for sensor positions near the central core. The optimum frequency seems to be in the 500- to 2000-Hz range, although it is not as clear in this case as for the radial flux because the vertical component data have more scatter. At the highest frequencies, the signal was again about zero, as expected.

2.1.4 Modeling Verification—All calculations of flaw signals and all results on the effects of geometric variations involved two steps: Calculate the sensor response first for the unflawed case with a simple planar geometry. Next, repeat the calculation with the flaw in place or with some change in geometry. The predicted changes caused by the flaw or by a variation in geometry are the differences in calculated sensor response for the two cases. Unfortunately, the differences are almost always a very small fraction of the total signals, and the precision of the result is therefore suspect. To verify that the calculated flaw and geometric signals give at least the correct trends and may therefore be used for probe-design purposes, a new approach for calculating signal changes caused by flaws and geometric changes was developed. In addition to the first two steps, the new method requires a third calculation with boundary conditions derived from the results of the first pair of calculations. The third calculation provides a direct prediction of the change in signal caused by the

25

radial flux component

frequency dependence of crack signal
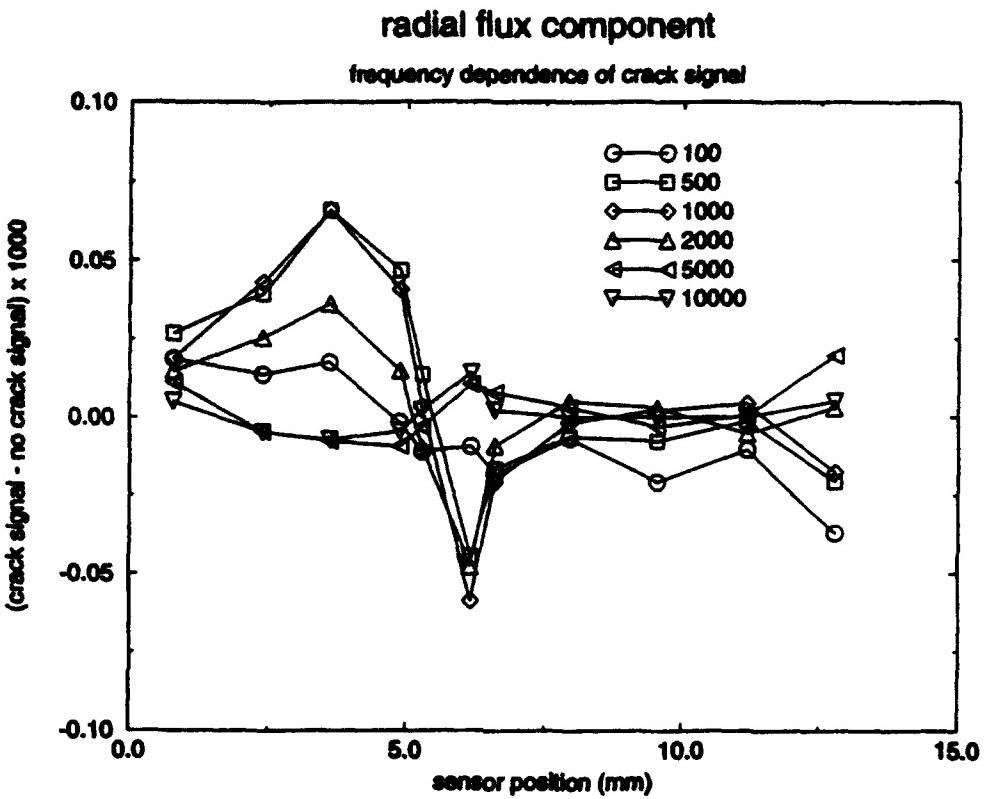
Figure 19. Radial component of the magnetic-flux density as a function of sensor position at frequencies from 100 to 10,000 Hz.

vertical flux component

frequency dependence of crack signal
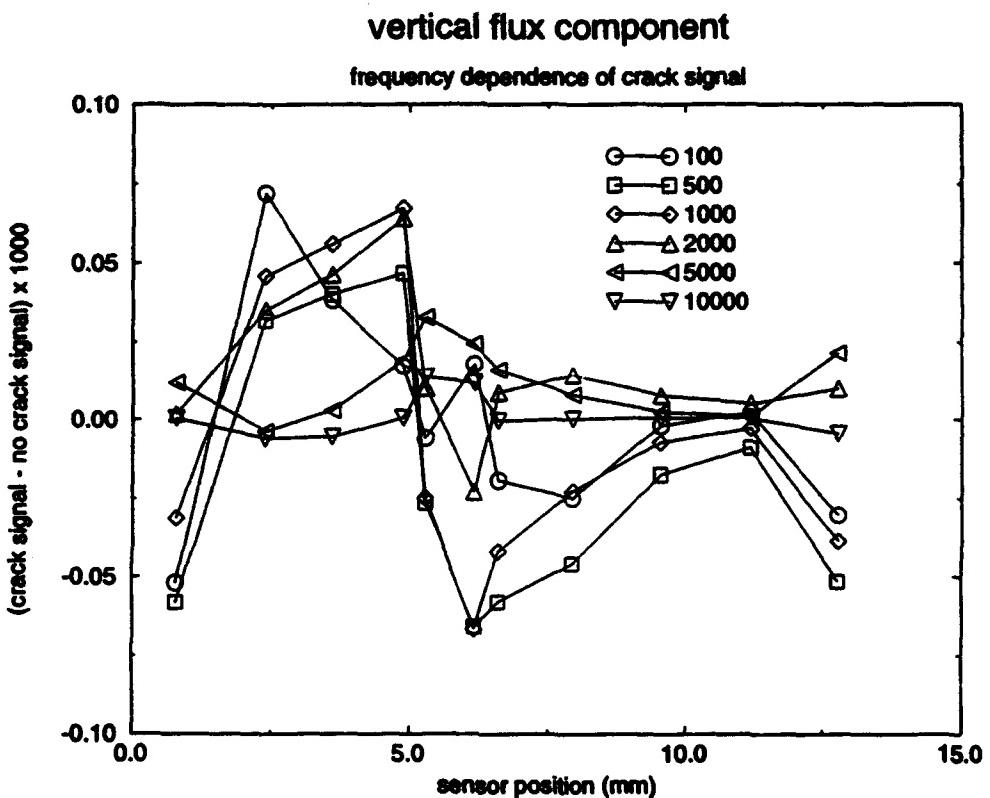
Figure 20. Vertical component of the magnetic-flux density as a function of sensor position at frequencies from 100 to 10,000 Hz.

26

flaw or geometric change and should therefore be much more accurate than the differencing method. Application of the proper boundary conditions is, however, a time-consuming task; and it was not feasible to use this approach for all cases. Instead, a few cases of flaw-signal calculations were performed to compare with data obtained by the differencing method.

To provide an estimate of the uncertainty in the previous results, calculations of flaw signals were performed with the new method as a function of frequency and sensor position for the conditions corresponding to those of Fig. 16. The new results confirmed earlier results as far as sensor position was concerned, but the frequency dependence was much stronger than that obtained earlier. In particular, flaw signals at higher frequencies were much smaller in the new calculations than in the results obtained by the differencing method. Although the high frequency error is significant, it has no bearing on the course of the experimental work because flaw-signal measurements are conducted only at low frequencies.

3. EXPERIMENTAL ARRANGEMENT/LABORATORY BREADBOARD

3.1 SPECIMENS

The specimen set used for the laboratory experiments consisted of preliminary specimens for preliminary tests, specimens containing structural variables typical of those encountered on aircraft structure, and specimens containing laboratory-grown fatigue cracks supplied by WL/MLLP. The specimens are described below.

3.1.1 **Preliminary Specimens**—A set of preliminary specimens was fabricated for initial experiments to evaluate probe response. The second layer consisted of a 6.4-mm-thick aluminum plate and various thicknesses of plates (from 1.6 to 6.4 mm thick) were used as first layers. The plates could be configured to obtain the following geometries: (1) fastener hole away from any edges and a simulated crack emanating from the second-layer hole, (2) fastener hole located 9.5 mm from the edge of the second layer to simulate a second-layer edge in an aircraft structure, and (3) the same configuration as (2) but with a crack emanating from the hole (crack orientation perpendicular to the edge direction). Two simulated cracks (saw slots) with dimensions of 2.8 and 5.2 mm radial length were used. A side view of the specimen configurations is shown in Fig. 21.

3.1.2 **Specimens with Structure Variables**—A specimen set was designed and fabricated to simulate aircraft structure and allow determination of the effects of fastener material, hole size and spacing, hole-to-edge spacing, flaw orientation, and layer thickness. The specimens are shown in Figs. 22 and 23. In the figures, Fn, Fs, and Fl designate fastener holes with no flaw, small flaw (2.5 mm radial length), and large flaw (3.8 mm radial length), respectively; all flaws are saw slots in the second layer. Specimen A, shown in Fig. 22, has three different hole-to-edge spacings for both the first and second layers and has holes with flaws of two sizes as well as unflawed holes. Note that the hole-to-edge spacings for the second layer (edge of second layer shown by dashed lines) are the same as those shown for the first layer (solid lines). Specimen B, shown in Fig. 23, has three hole sizes, three hole spacings, and two flaw orientations; a third flaw orientation is obtained from specimen A in Fig. 22. One set of flaws in holes with different spacings between the holes is placed toward the adjacent holes, since this is where the largest effect from the adjacent hole would be encountered; another set is placed 90 degrees from the adjacent hole to determine the effect or
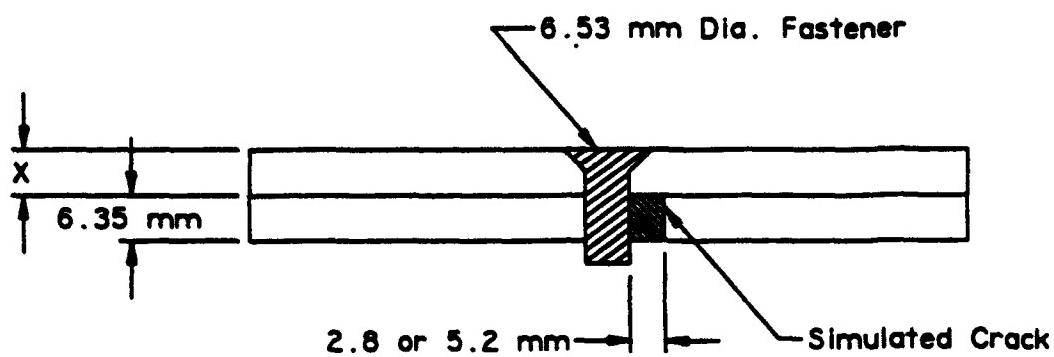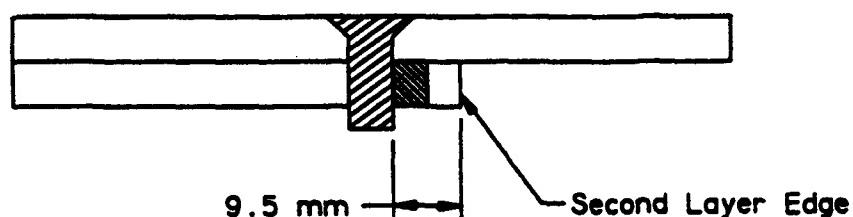
Figure 21. Preliminary specimen configuration: (A) fastener hole away from edges; (B) simulated aircraft structure geometry with second-layer edge close to fastener.
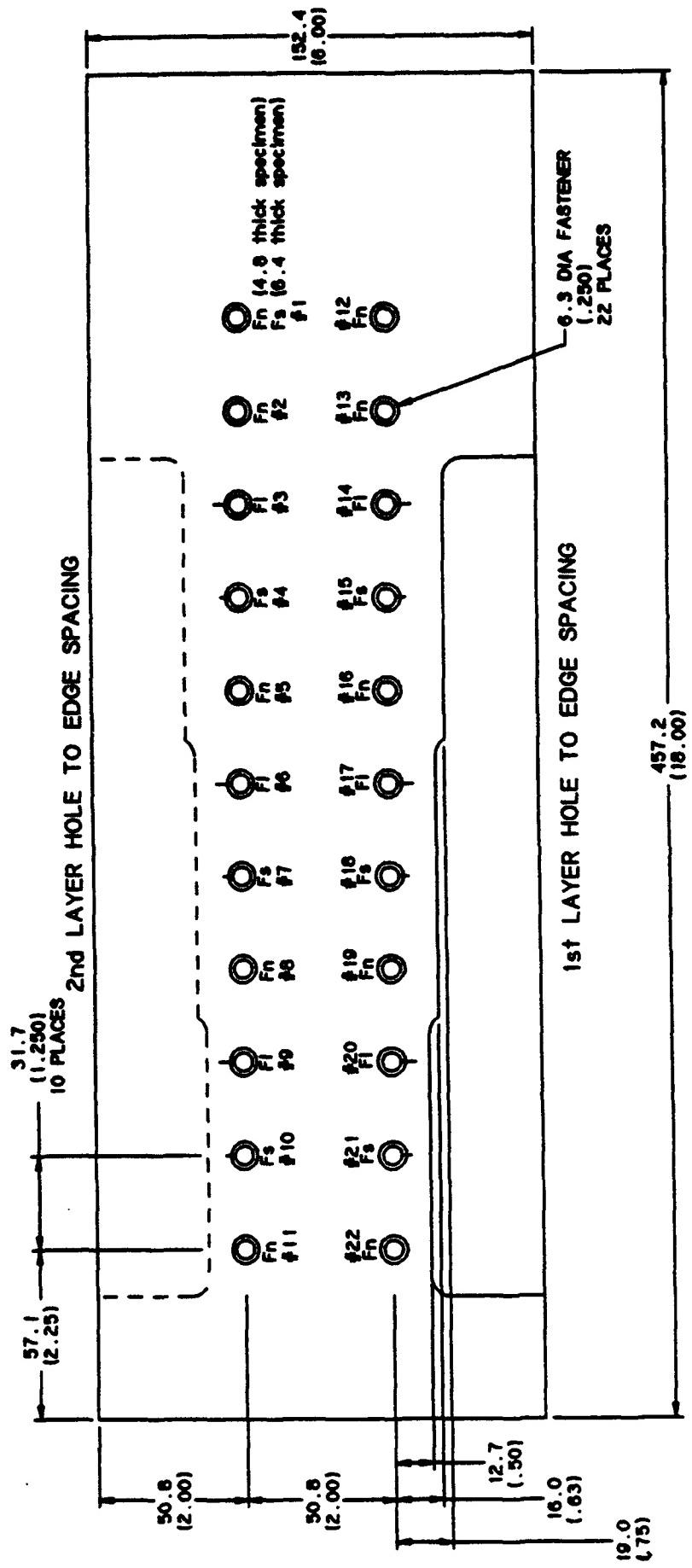
Figure 22. Configuration of specimen A for hole-to-edge spacing
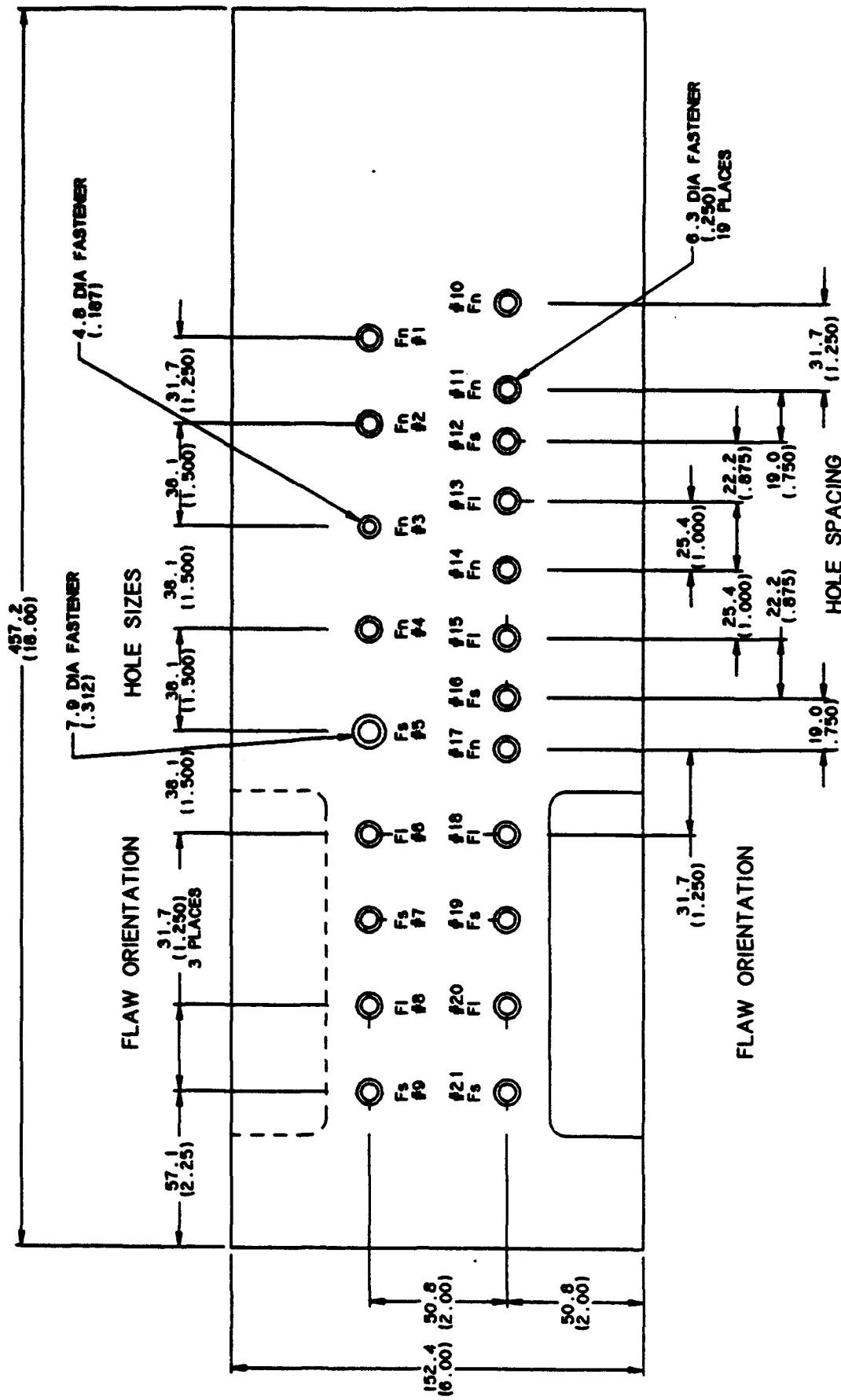
KEY

Fn = NO FLAW
Fs = SMALL FLAW = 2.5 (.10) RADIAL LENGTH
Fl = LARGE FLAW = 3.8 (.15) RADIAL LENGTH

NOTES:
1. DIMENSIONS ARE IN MILLIMETERS (INCHES).
2. 1 EACH SPECIMEN WITH 4.8 (.187) THICK LAYERS
   1 EACH SPECIMEN WITH 6.4 (.250) THICK LAYERS

Figure 23. Configuration of specimen B for flaw orientation, hole size, and hole-to-hole spacing.

KEY

Fn = NO FLAW

Fs = SMALL FLAW = 2.5 (.10) RADIAL LENGTH

Fl = LARGE FLAW = 3.8 (.15) RADIAL LENGTH

NOTES:

1. DIMENSIONS ARE IN MILLIMETERS (INCHES).

2. 1 EACH SPECIMEN WITH 4.8 (.187) THICK LAYERS
   1 EACH SPECIMEN WITH 6.4 (.250) THICK LAYERS

31

orientation. Specimens were fabricated in both 4.8- and 6.4-mm thicknesses from 7075 T6 aluminum alloy. Titanium and steel fasteners could be interchanged in the specimens to determine the effect of fastener material. Hi-Lok fasteners with a 100-degree countersunk head (HL11 and HL19 for titanium and steel, respectively) were used.

3.1.3 WL/MLLP Specimens—Four two-layer fastener specimens (sample numbers A1-4, A3-19, B2-17, and B3-20) were provided by WL/MLLP for use in the project. The specimen configuration is shown schematically in Fig. 24, and specimen and flaw dimensions are shown in Table 1; additional details are provided in the appendix. The "A" specimens have first- and second-layer thicknesses of 4.0 and 2.5 mm, respectively; the "B" specimens have thicknesses of 6.9 and 4.5 mm, respectively.

3.2 PROBES

The two probe configurations that the model showed to be the best choice for circumferential scans were the 45- and 90-degree angular widths with a radial length of 4 mm. These probe designs were chosen for the experiments, and the resulting probe configurations are described below.
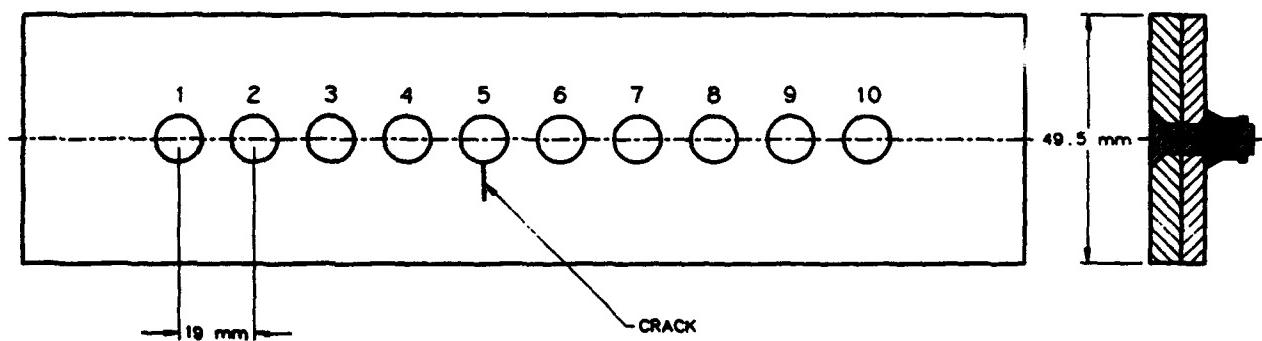
Figure 24. WL/MLLP specimen configuration: layer dimensions and crack sizes are given in Table 1; fastener diameter is 6.4 mm.

TABLE 1. WL/MLLP Specimen Configuration and Crack Sizes

Specimen	First-Layer Thickness [mm (inch)]	Second-Layer Thickness [mm (inch)]	Cracked Surface	Cracked Hole No.–Crack Size[a] [mm (inch)]
A1-4	3.96 (0.156)	2.54 (0.100)	First Layer, Faying Surface	1–0.711 (0.028)
A3-19	3.96 (0.156)	2.54 (0.100)	Second Layer, Outside Surface	6–2.56 (0.101), 8–2.67 (0.105)
B2-17	6.86 (0.270)	4.47 (0.176)	First Layer, Countersink Surface	6–2.46 (0.097), 7–2.44 (0.096)
B3-20	6.86 (0.270)	4.47 (0.176)	Second Layer, Faying Surface	4–2.51 (0.009), 10–2.44 (0.096)

[a]Remainder of holes not cracked.

33

In addition, a symmetrical cup-core probe was fabricated for linear raster scan experiments. Because of the limited availability of ferrite core shapes and difficulty in machining the ferrite to desired dimensions, the core configurations were based on the closest available ferrite cores, which required a minimum amount of machining.

3.2.1   85-Degree Probe—The 90-degree angular-width probe was approximated with a "PQ" type core with an angular width of approximately 85 degrees, as shown in Fig. 25. The center post of the as-purchased core was too large and too far from the outer leg; it was, therefore, cut from the core and replaced by a smaller post cemented in place at the desired radial distance. An excitation coil was wound around the center post, as shown in the figure.

Sensor coils with and without ferrite cores were fabricated; the coils were designed so that their position and orientation with respect to the exciter core could be changed in investigated optimum sensor locations. The sensor position shown by the solid lines in Fig. 25 is oriented to detect the vertical component of the magnetic field, and the sensor shown by the dashed lines is
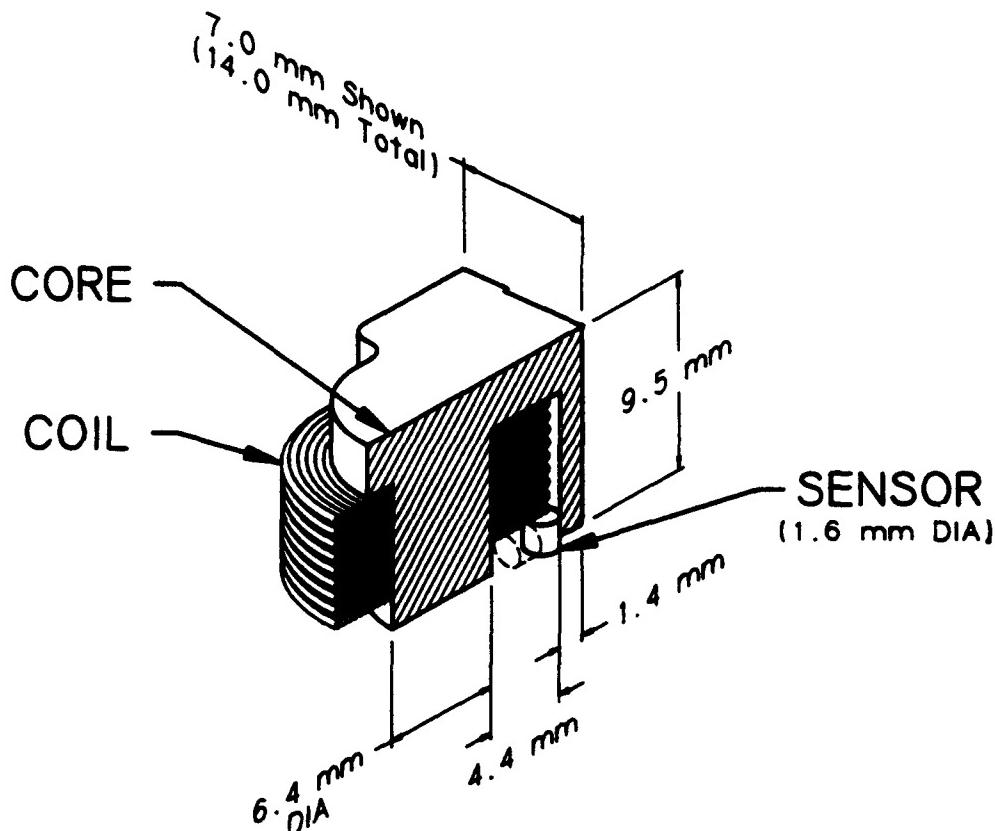
Figure 25. Cross-sectional view of the 85-degree segment probe. Vertical and radial sensor orientations are shown by solid and dashed lines, respectively.

34

oriented to detect the radial component. The sensor could also be positioned to detect the circumferential component; this orientation is now shown, but the sensor axis would be in the same plane as, and perpendicular to, the radial sensor axis.

For tests with magnetic fasteners, centering difficulties were encountered because of the nonuniform magnetic response of the fastener [subsection 5.2.2(6)]. It was believed that the magnetic flux path from the exciter center core, through the fastener head, and to the outer leg (and thus the sensor coil) produced strong coupling directly into the sensor, and thus aggravated this problem. One approach which was undertaken to address the problem was to add conductive shielding to reduce this direct flux path. Eddy currents induced in the conductive shield produce a magnetic field having the opposite sign of the main field, and thus some cancellation of the main field occurs in the region of the shield. The probe was modified by adding a copper ring concentric with the center leg of the exciter core and located between the center leg and the sensor.

3.2.2   35-Degree Probe—The 45-degree angular-width probe was approximated by a U-shaped core of constant width which was cut from an E-core. The probe is shown in Fig. 26. The width of the core outer leg was equivalent to an arc of approximately 35 degrees. The coil was
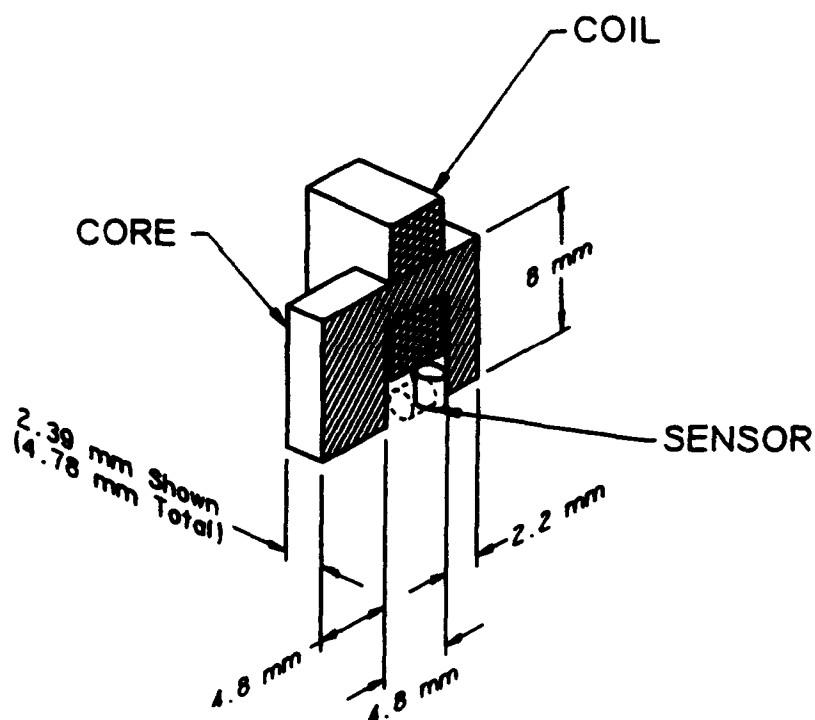
Figure 26. Cross-sectional view of the 35-degree segment probe. Vertical and radial sensor orientations are shown by solid and dashed lines, respectively.

wound on the upper portion of the core, which connected the center post and outer leg. Although this configuration was not modeled, it was reasoned that by placing the coil on the upper portion of the core instead of the center leg (as with the 85-degree probe), the induced current in the specimen on the opposite side of the fastener would be reduced and the current would be more localized under the outer leg. The same sensors as described above were used with the 35-degree probe.

3.2.3 Cup-Core Probe for Linear Scans—Although the model showed the above probe designs to be better than a symmetrical cup-core configuration, interpretation of linear raster scan data was greatly simplified if the probe were symmetrical and thus produced a symmetrical response. In addition, a symmetrical probe was needed for raster scanning in order to have sensitivity to flaws in all orientations around the fastener hole. The cup-core probe configuration is shown in Fig. 27. The sensor coil was wound on the center post. The relatively large-diameter post in the commercially available core was removed and replaced by a smaller diameter rod in order to improve sensor resolution.

3.3 SCANNING SYSTEM

Mechanical fixturing was fabricated to adapt an existing mechanical scanning system for use as the laboratory breadboard system. A drawing of the breadboard is shown in Fig. 28, and a photograph is shown in Fig. 29. Adjustable clamps held the specimen in place and allowed accommodation of different specimen sizes and configurations. The specimen was positioned vertically, as shown in the figure. The eddy current probe was mounted on a stepper-motor-driven rotary turntable, which allowed it to be rotated around the fastener under computer control. The rotary turntable was mounted on a linear scanning system with stepper-motor-driven motion in the horizontal and vertical directions to allow the probe to be positioned over the fastener. The linear motion could also be used to perform a raster scan of the probe over the specimen surface. Liftoff of the probe from the specimen surface was controlled by a manual adjustment.

3.3.1 Circumferential-Radial Scan—The primary scanning mode was to scan the probe circumferentially around the fastener as shown in Fig. 30, which is a view looking down on the probe and fastener hole. Initially, a single scan in the direction of the arrows with the probe center leg centered over the fastener (radial position 1) was used. (Centering was accomplished using a 5-kHz excitation to eliminate subsurface response and by moving the probe center of rotation to minimize the response while scanning circumferentially.) Later, a two-dimensional scan approach
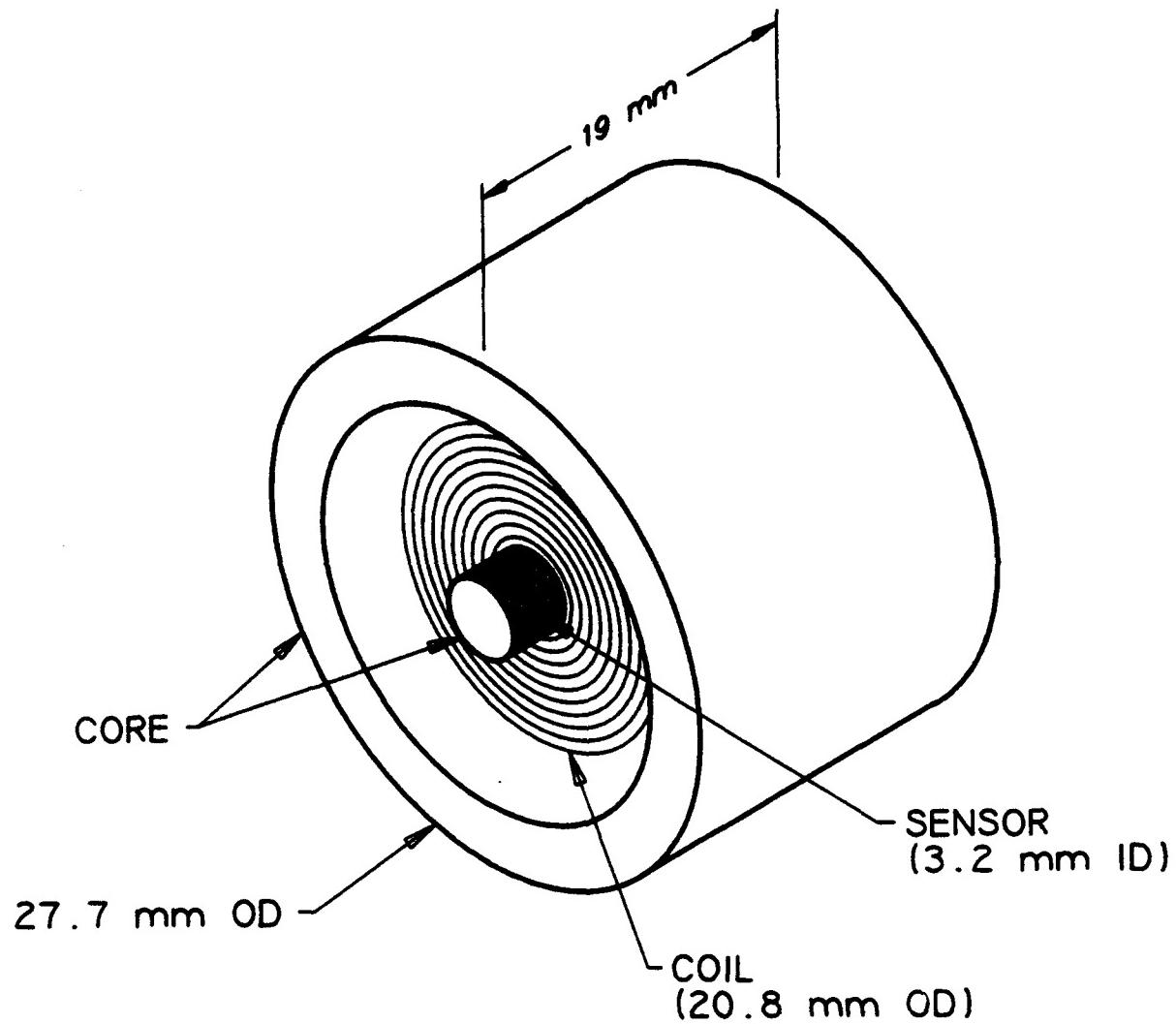
Figure 27. Cup-core probe configuration.
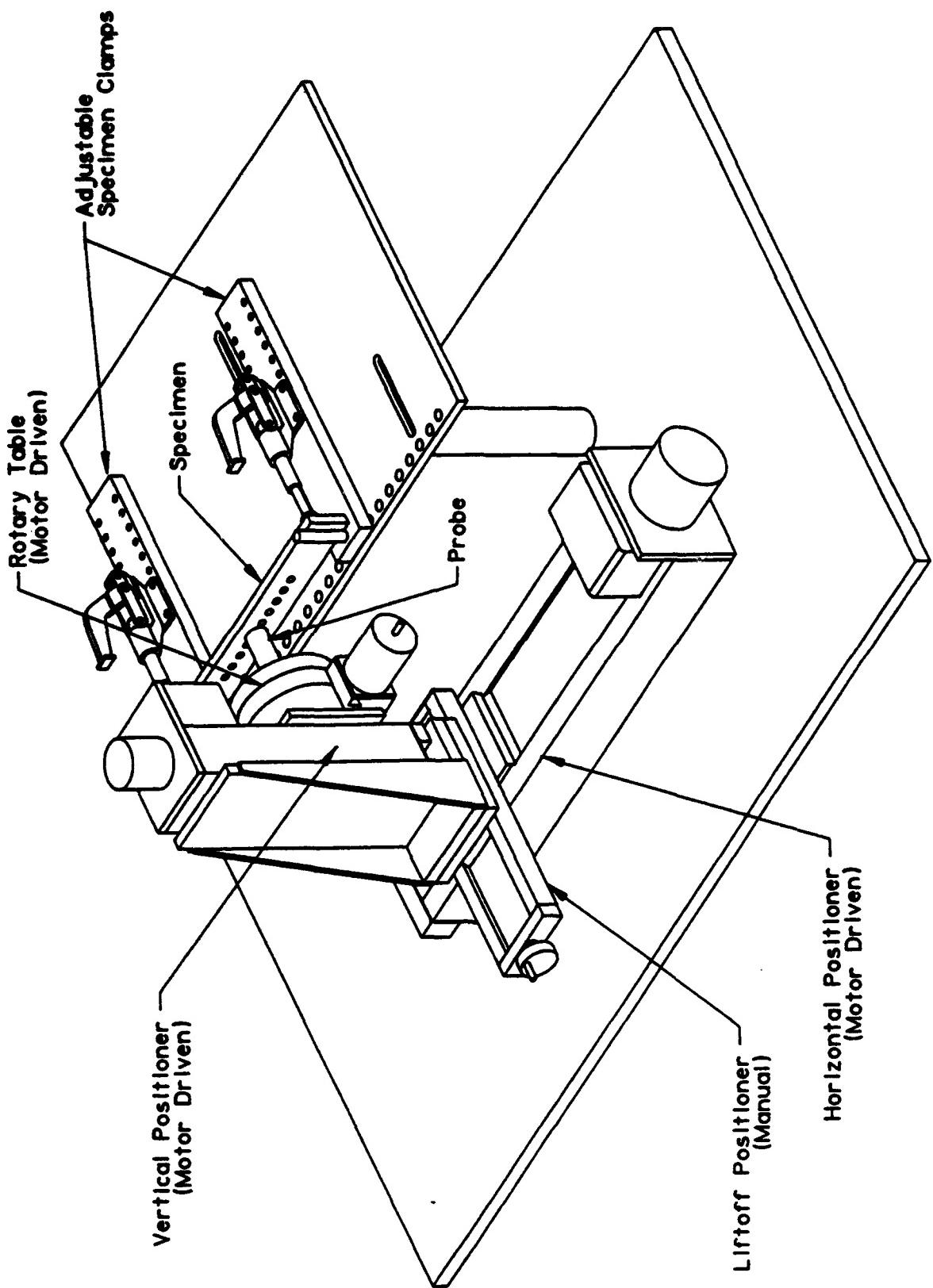
Figure 28. Laboratory breadboard scanning system.

38
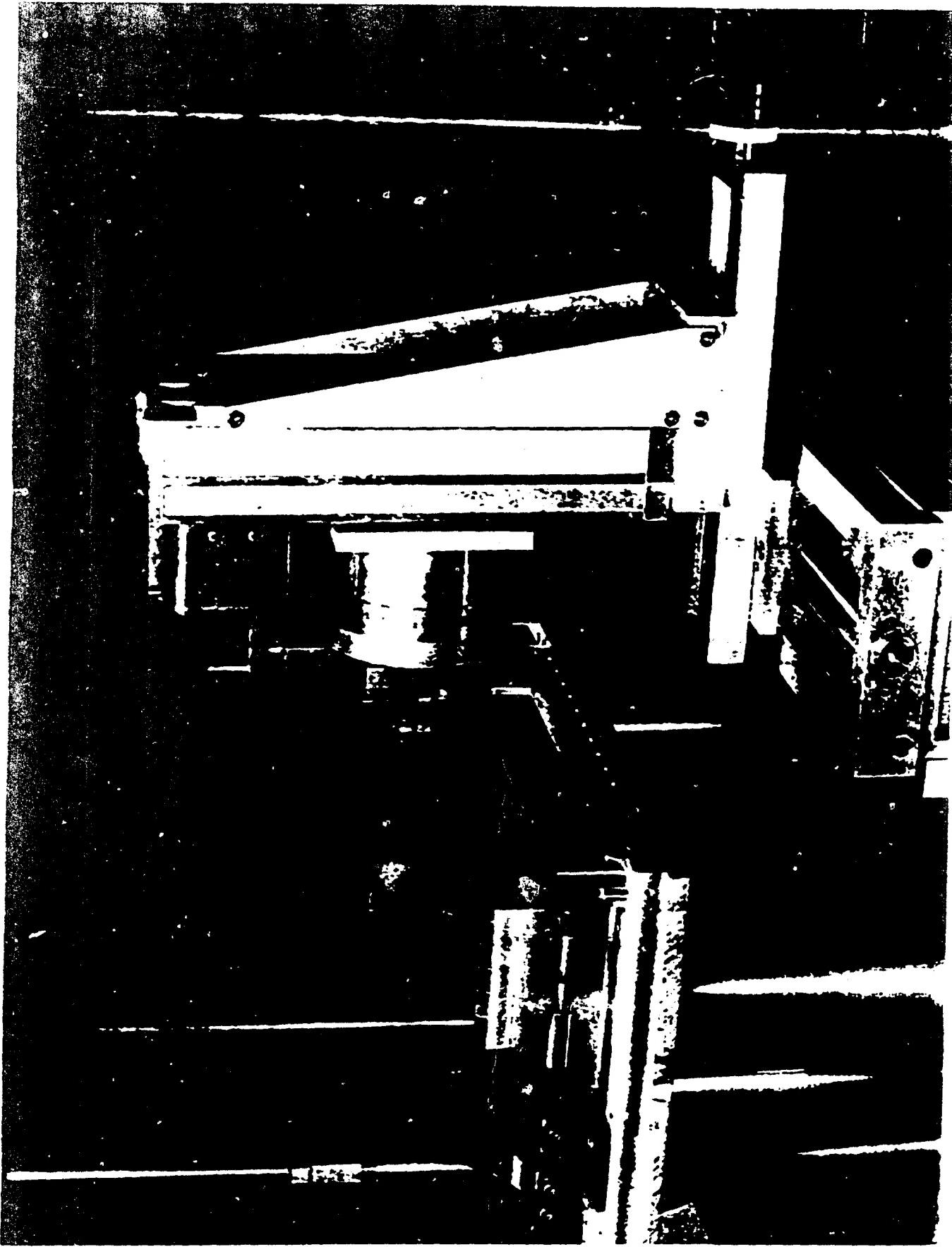
Figure 29. Photograph of laboratory breadboard scanning system.

39
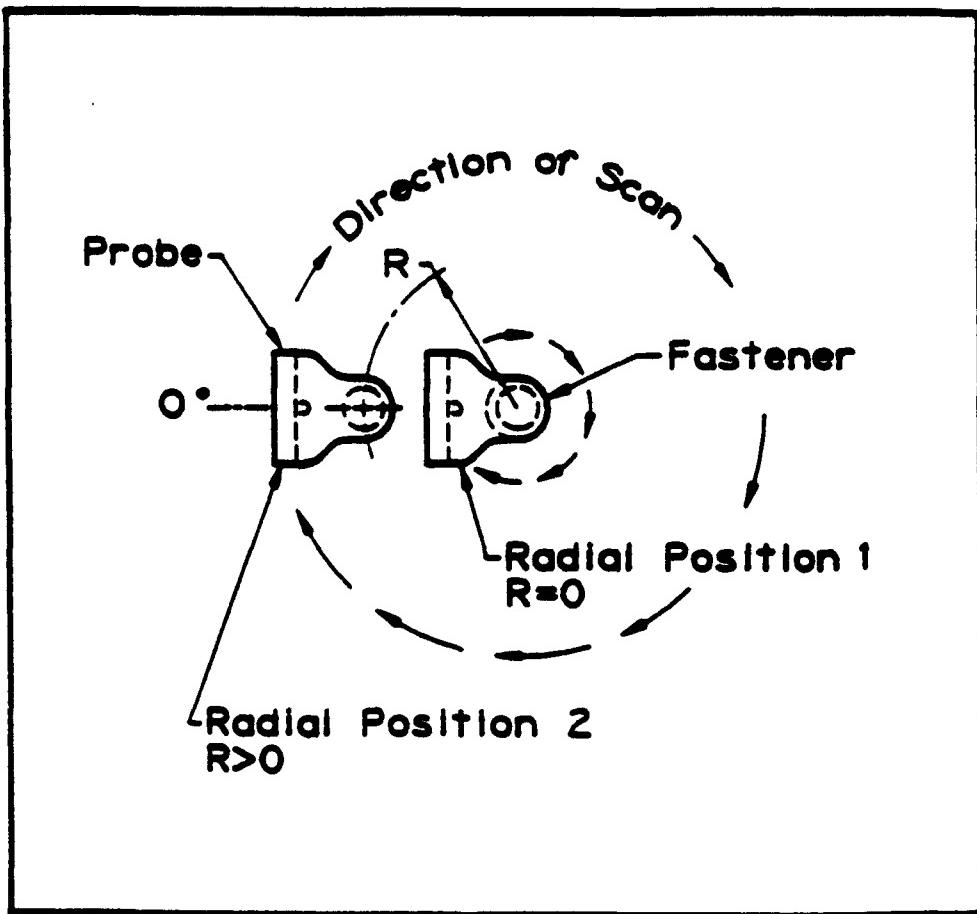
Figure 30. Probe scanning configuration for circumferential scans with radial increments. (Note: Radial position 2 exaggerated for illustration purposes.)

was investigated to determine if improved flaw detection and discrimination from structure geometry could be accomplished using two-dimensional imaging. In order to generate two-dimensional data, additional data had to be taken at increasing radii. This was accomplished by moving the probe to a new radial position (position 2, radius R>0; note that the step to the new radius was exaggerated for illustration purposes), as shown in Fig. 30. The probe was then scanned as shown by the arrows. This was repeated for additional radii; typically, scans were made for 11 different radii in increments of 0.64 mm. Note that all scans are concentric about the center of the fastener.

The eddy current distribution obtained with the probe centered over the fastener (radius R=0) is concentrated under the probe arm and near the fastener (see Fig. 8). Although modeling was not done for larger radii, it is expected that as the radius is increased, the current distribution remains under the probe arm but becomes somewhat redistributed since the relationship between the probe and fastener hole is changed. This results in an offset (change in dc level) in the detected eddy

current signal as the probe is stepped to a new scan row; this offset is removed by either renulling the eddy current instrument or using a dc level removal computer algorithm. The redistribution of the eddy current pattern does not interfere with analysis of the data since the resulting offset is removed and since the redistribution is consistent from one fastener hole to the next. Thus, comparing the response from one hole to another to determine the presence of flaws is based on responses having the same current distribution.

3.3.2 **Linear Raster Scans**—Limited data were taken using a linear raster scan. This scan approach is similar to the circumferential-radial scan, except that the probe was scanned linearly instead of circumferentially and indexed perpendicular to the scan direction instead of in the radial direction. The scans started at a position away from the fastener hole and were indexed so that they passed over the hole and finally to the opposite side, as shown in Fig. 31. The advantage of this approach is that it is not necessary to align the scan with respect to the fastener hole, as is the case with the circumferential-radial scan.

3.4 INSTRUMENTATION

Experiments were performed using both chirp waveform excitation as well as single-frequency excitation. Instrumentation consisted of existing laboratory equipment. Instrumentation setups for both arrangements are described below.

3.4.1 **Chirp Excitation**—Fig. 32 shows a block diagram for the chirp excitation instrumentation. A chirp waveform was defined using computer software and was used to program an arbitrary waveform generator (LeCroy 9112), which produced an analog output of the waveform. This signal was amplified using a power amplifier (Techron 7540) and then was used to drive the probe excitation coil. The sensor-coil output was amplified and low-pass filtered (using the preamp and filter in an EG&G PARC Model 5302 lock-in amplifier). The resulting signal was digitized using an analog-to-digital converter (National Instruments AT-MIO-16F) in a personal computer (486, 25 MHz). A reference waveform from the arbitrary waveform generator was also digitized along with the sensor-coil signal. The signals were digitized at a rate of 100K samples/second. The digitized data were then stored and analyzed on a Unix workstation computer (Sun-4). The probe scanning system was controlled by the personal computer.
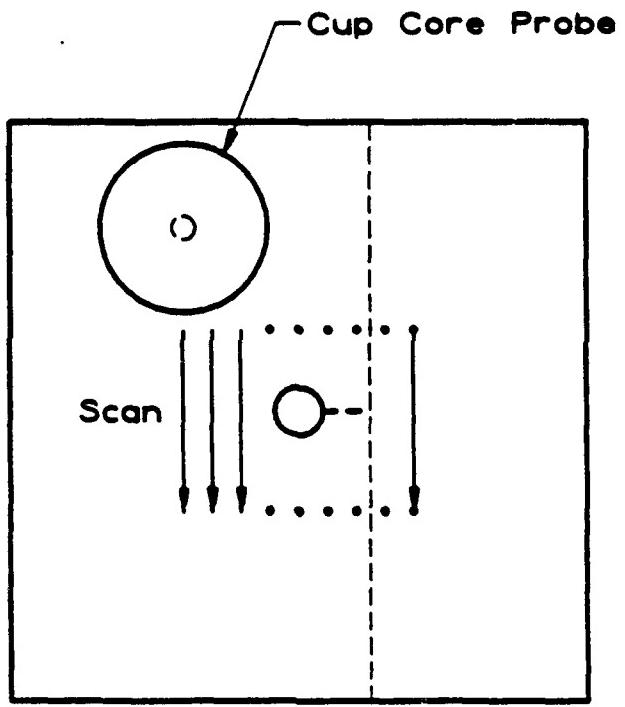
Figure 31. Scan configuration for linear raster scan using cup-core probe.

The digitization of the chirp was synchronized with respect to the circumferential scanning of the probe using the stepper-motor-drive pulses so that a single chirp was digitized every degree of the scan. The scan speed was limited to 0.83 rev./minute because of the data transfer rate from the computer memory to the disk drive for storage.

3.4.2 **Single-Frequency Excitation**—Experiments using single-frequency excitation were also performed. Because of the need for multiple-frequency data (e.g., for centering and investigating multifrequency mixing to reduce effects of first-layer structure geometry), a multifrequency eddy current instrument (Zetec MIZ-40) was used. This allowed data at four frequencies (typically 250, 500, 1000, and 2000 Hz) to be acquired simultaneously. Also, centering was typically accomplished by switching to 5000 Hz. A block diagram of the instrumentation is shown in Fig. 33; the instrumentation was similar to that for the chirp excitation. The power amplifier was used between the eddy current instrument and probe to drive the excitation coil, and the preamp was used to amplify the sensor-coil signal for input to the eddy current instrument. Both horizontal (in-phase) and vertical (quadrature) components of the signal were digitized for all four frequencies with respect to the scan position as determined by the stepper-motor-drive pulses. The horizontal component is derived from the component of the eddy current signal which is in phase with the excitation coil voltage. The vertical component is derived from the component which is in quadrature (90 degrees out of phase) with the excitation coil voltage. The scan speed was 1.7 rev./minute.
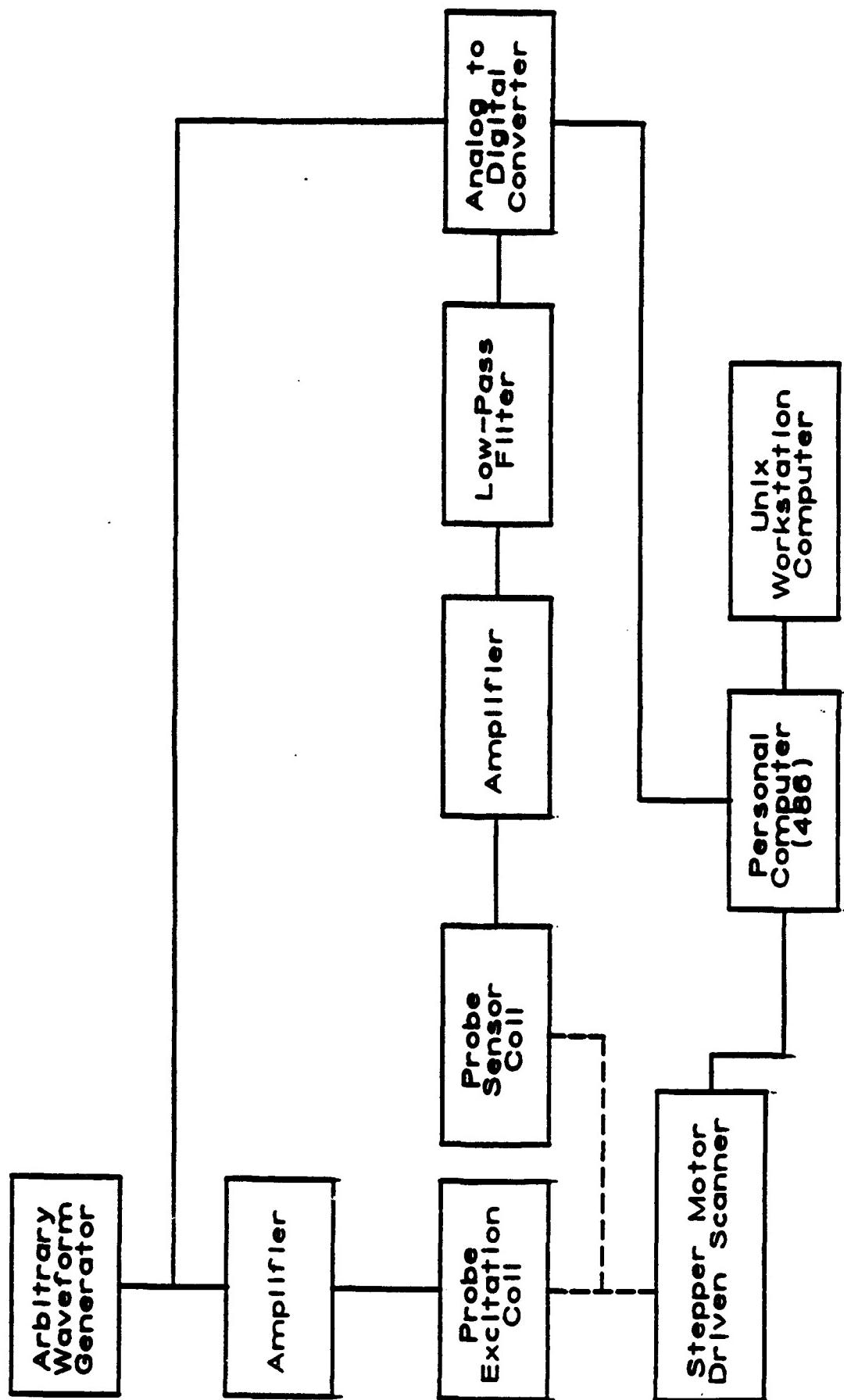
Figure 32. Block diagram of instrumentation for chirp excitation.
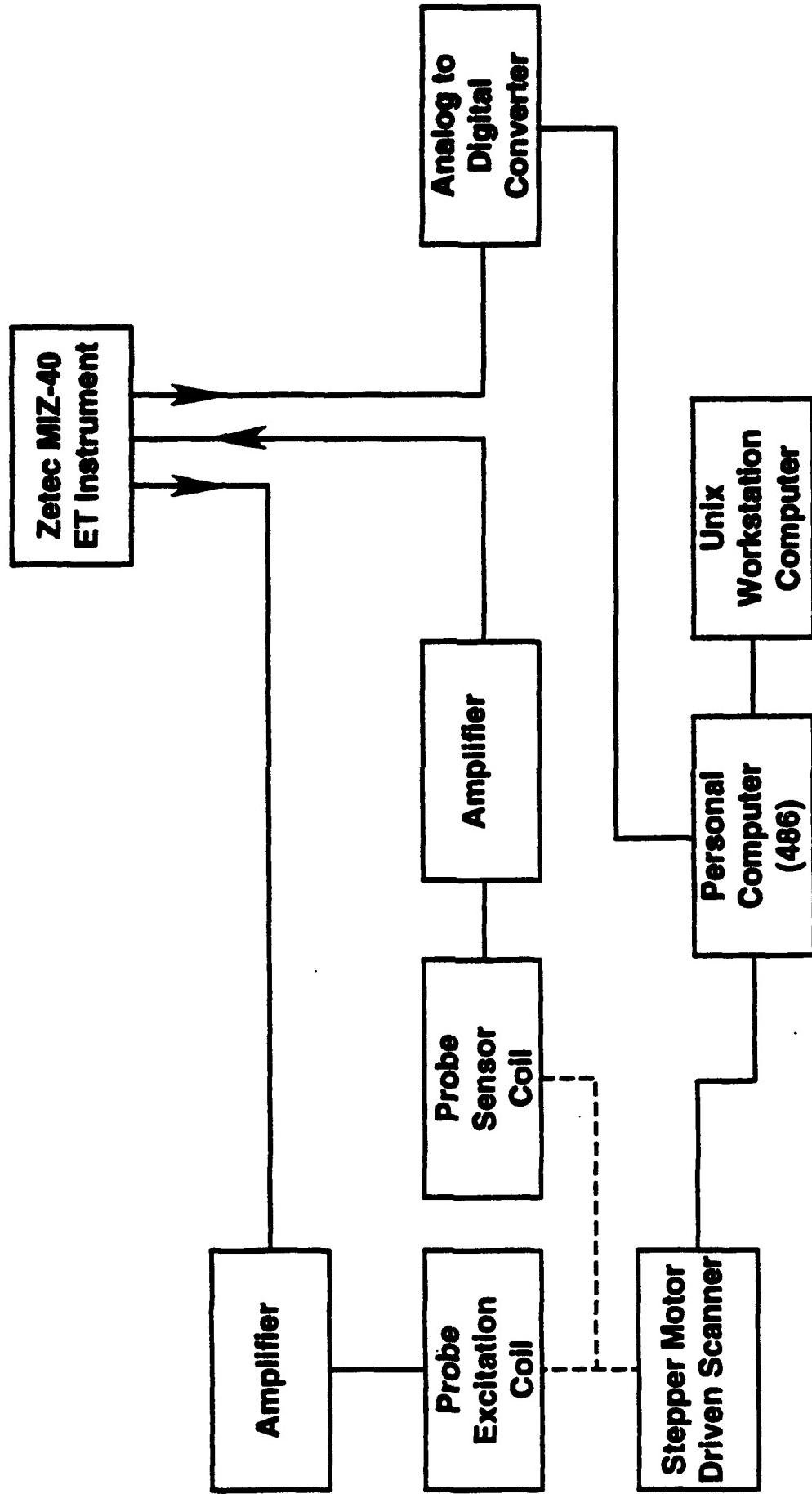
Figure 33. Block diagram of instrumentation for single-frequency experiments.

44

4. SIGNAL PROCESSING

4.1 CHIRP ANALYSIS

A chirp waveform is a burst of energy within which the frequency varies continuously between minimum and maximum limits. For the experiments using a chirp excitation, the signals were processed to obtain the frequency spectrum of the chirp and the equivalent of a time domain impulse response as described below. The purpose of the frequency spectrum analysis was to determine if better discrimination could be obtained between flaw signals and nonrelevant geometry signals by examining their effects on the frequency spectrum. The frequency spectrum would also provide guidance as to the best frequencies for single-frequency excitation experiments. The purpose of the impulse response analysis was to determine if discrimination between flaw signals and nonrelevant geometry signals could be obtained by examining their effects on the shape of the time domain pulse.

4.1.1 **Chirp Frequency Spectrum**—The chirp excitation was an exponential frequency sweep from 200 to 10,000 Hz. The frequency spectrum of the chirp response was obtained by taking the Fourier transform of the signal and computing the absolute value of each spectral coefficient. In order to make changes in the spectrum more apparent, the spectrum at the 0-degree probe position in the scan was subtracted from the spectrum at all circumferential positions.

4.1.2 **Chirp Impulse Response**—The principle of impulse simulation with a chirp waveform is illustrated in Fig. 34. An impulse is an ideal function with finite energy that occurs in an infinitely short time period. To the extent that an impulse can be simulated, the excitation signal is separated in time from received signals, and received signals from different locations would be separated in time. Since it is impossible to create an impulse-like signal in an eddy current coil, a signal-processing approach to gain the same information was chosen. As is well known in the field of radar signal processing (3), the autocorrelation function of a chirp is a time domain pulse with characteristics determined by the duration and bandwidth of the chirp. Thus, time domain signals equivalent to pulsed excitation can be synthesized by computing the autocorrelation function for data with a chirp excitation.

The chirp responses from the experimental data were filtered with a cosine-squared window in order to reduce ripple in the autocorrelation, and the autocorrelation functions of the

| (A) | (B) |
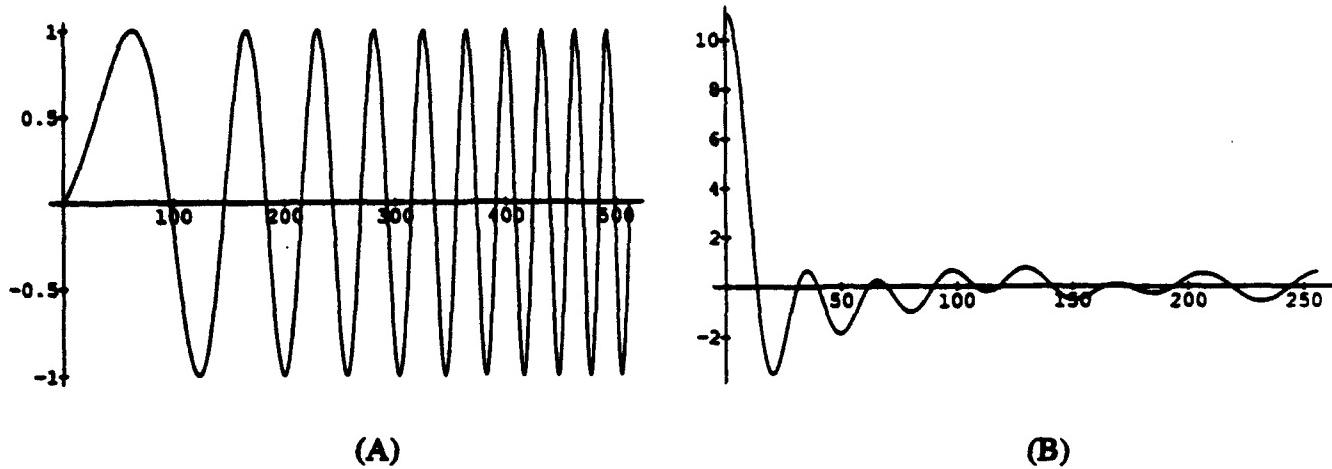
Figure 34. A chirp waveform (A) and its autocorrelation function (B). Autocorrelation of a chirp which synthesizes a short, time-domain pulse.

filtered chirp responses were calculated. The magnitude of the autocorrelation is then displayed as a function of time. In order to make changes in the impulse response more apparent, the response at the 0-degree probe position in the scan was subtracted from the spectrum at all circumferential positions.

4.2 DISCRETE FREQUENCY ANALYSIS

Discrete frequency data were analyzed by changing the phase to look at a particular component of the eddy current signal relative to the in-phase and quadrature components and by using multifrequency mixing. The purpose in both cases is to help separate flaw signals from nonrelevant signals.

4.2.1 Phase Rotation—This approach is based on the fact that the phase of the currents flowing in the specimen is a function of depth. Therefore, signals from flaws and structure at different depths occur at different phase angles. Phase rotation can, therefore, be used to distinguish between signals at different phases and, thus, different depths.

The phase rotation procedure is illustrated in Fig. 35. A signal from a subsurface flaw is represented by the vector M_1 at a phase angle α_1 with respect to the in-phase axis (Fig. 35a), and the signal from near-surface geometry is shown by M_2 at a phase angle α_2. These signals have components I_1 and I_2 on the in-phase axis. If the axes are rotated by an angle of $90° - \alpha_2$ as shown in Fig. 35b, the geometry signal is aligned with the quadrature axis and has no component along the in-phase axis ($I_2 = 0$). The flaw signal does, however, have a component (I_1) on the in-phase axis. If only this signal component along the in-phase axis is measured (after rotating the axes), the geometry signal component aligned with the quadrature axis is minimized.

46
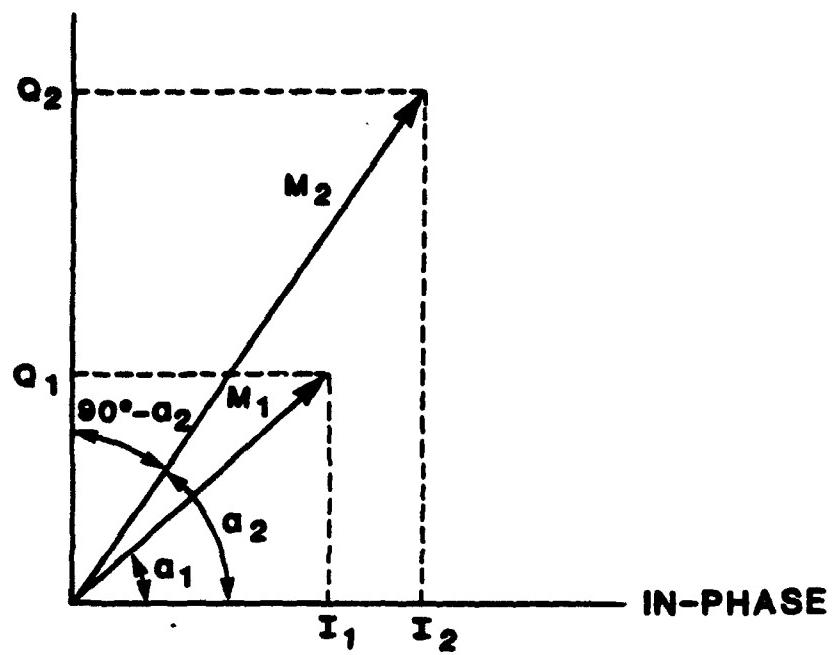
(A) Before rotation of axes
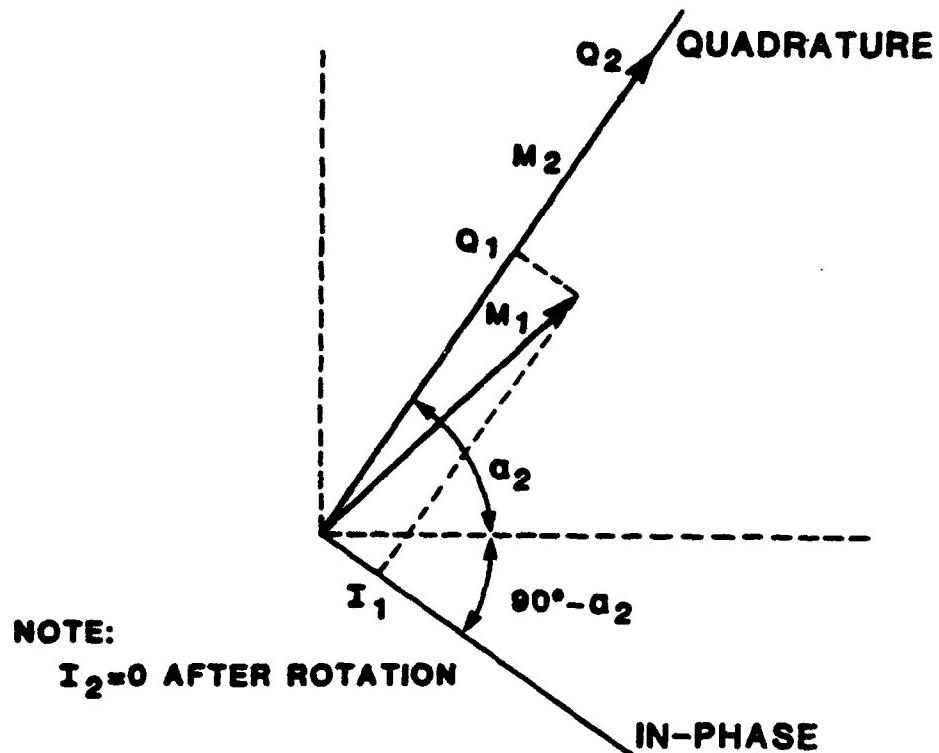
(B) After rotation of axes by $90° - \alpha_2$

Figure 35. Representation of in-phase and quadrature ECP signal components before and after rotation of axes.

47

4.2.2 Multifrequency Mixing—The multifrequency mixing approach uses an equation to transform the data at the higher frequency to the same shape as the data at the lower frequency by using all data points from the scans. The coefficients for the transform equation are generated on a fastener hole with no flaw and then applied to unknown fastener holes. The transformed high-frequency data can then be subtracted from the low-frequency data to remove undesired signals (such as those from off-centering) and reveal the flaw signal provided the undesired and flaw signals have sufficiently different responses to the two frequencies.

Separate transforms are applied to the in-phase and quadrature components of the signals. The transform equation for the in-phase component is

$$I_t = C_1 + C_2 I_1 + C_3 Q_1 + C_4 Q_2 \tag{1}$$

where I_t is the transformed in-phase signal component, I_1 is the in-phase signal component at frequency 1, Q_1 is the quadrature signal component at frequency 1 (high frequency), Q_2 is the quadrature signal component at frequency 2 (low frequency), I_2 is the in-phase signal component at frequency 2, and $C_1 .. C_4$ are constants.

The transform equation for the quadrature component is

$$Q_t = k_1 + k_2 I_1 + k_3 Q_1 + k_4 I_2 \tag{2}$$

where Q_t is the transformed quadrature signal component, I_1 and Q_1 are the same as above, and I_2 is the in-phase signal component at frequency 2.

The coefficients of the transform equation are determined by a least squares solution; for example, C_1, C_2, C_3, and C_4 of equation (1) are determined by minimizing the error function

$$e \, (C_1, C_2, C_3, C_4) = \Sigma \, (C_1 + C_2 I_1 + C_3 Q_1 + C_4 Q_2 - I_2)^2 \tag{3}$$

where the summation is over all of the data generated on a fastener hole without a flaw. In this way, the transformation is optimized to minimize the undesired effects at all scan positions. The in-phase flaw signal is then just $I_t - I_2$.

4.3 COLOR IMAGING OF TWO-DIMENSIONAL SCAN DATA

The purpose of the color imaging was to provide a means for analyzing two-dimensional spatial data taken from raster scans. This approach takes advantage of the human ability to perform pattern recognition and thus provide discrimination between signal patterns from flaws and those from structure.

The color images are derived as follows: Fig. 36 shows a typical set of data obtained from a two-dimensional circumferential scan of fastener hole 9 in specimen A which contains a 3.8-mm second-layer flaw. At the bottom of the figure is a strip-chart plot of the horizontal or in-phase component of the eddy current signal versus circumferential probe position for a circumferential scan at a radius of 0.6. (Note that phase rotation has been applied to maximize the flaw signal and minimize second-layer edge response.) The color image shown immediately above the strip chart is derived from the amplitudes of the signals (such as the one shown in the strip chart) for circumferential scans at each radial position of the probe. Radial position zero corresponds to the probe being centered over the fastener (radial position R=0 in Fig. 30). The narrow rectangle in the color image shows the single scan corresponding to the actual signal shown in the strip chart in the figure. The color in the image is related to the amplitude of the signal. The vertical scale in the strip chart is in relative units, which are percent of full scale for the eddy current instrument display. The color scale, as shown at the bottom of the figure, ranges from dark red for the most positive signal amplitude to dark blue for the most negative signal amplitude (with approximately 120 colors in between) and is keyed to the scale units and can be adjusted to correspond to a selected range of the scale. In this figure, dark blue and dark red correspond to -5 and 12 on the strip-chart amplitude scale, respectively.

To the right of each strip chart is a conventional impedance plane presentation of the vertical component of the eddy current signal plotted versus the horizontal component. The horizontal component is derived from the component of the complex eddy current signal which is in phase with the excitation coil voltage. The vertical component is derived from the component which is 90 degrees out of phase with the excitation coil voltage. The "+" sign in the figure shows the signal value which corresponds to the location of the cursor at 180 degrees in the strip chart.

49
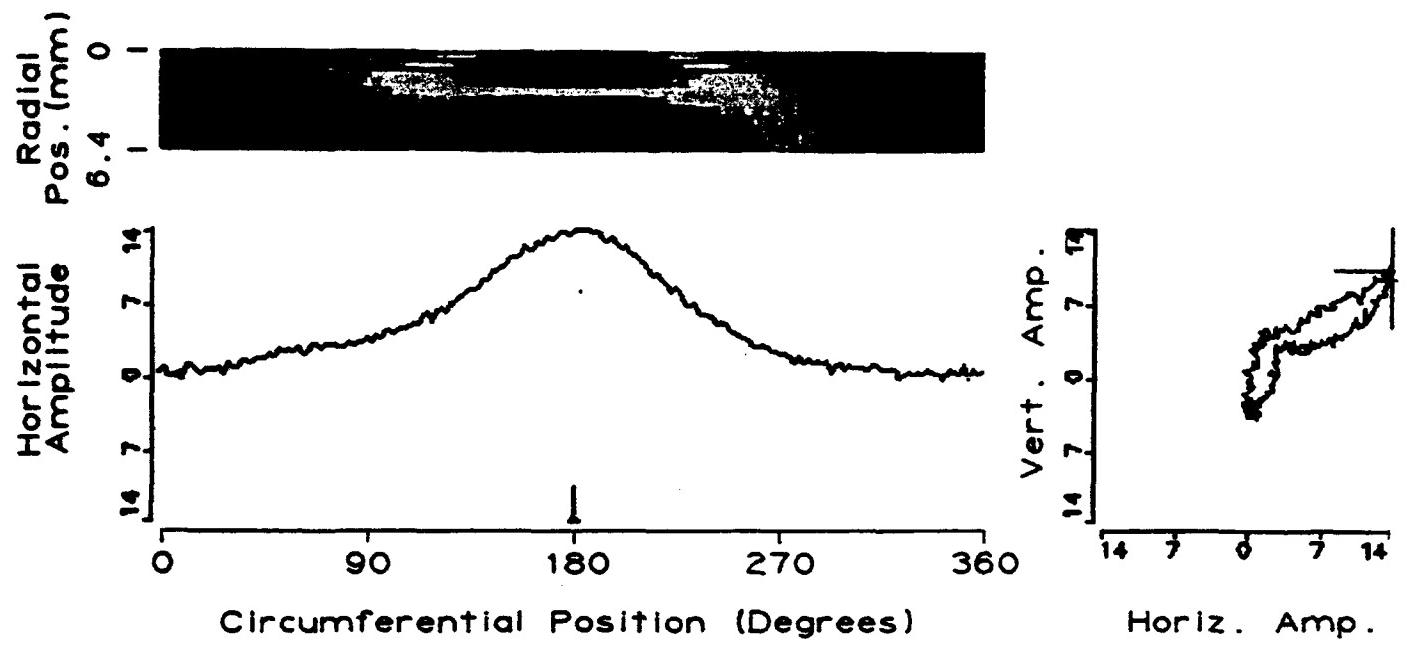
Figure 36. Example of data from two-dimensional circumferential-radial scan of fastener hole 9 in specimen A. Hole contains 3.8-mm flaw and second-layer edge at 180 degrees. Color scale shown at bottom ranges from -5 to 12 on strip-chart scale.

(NOTE: COLOR COPY AVAILABLE FROM CONTRACTOR)

5. EXPERIMENTAL RESULTS

The experimental results are described in this section. First, section 5.1 describes the results obtained with chirp excitation. Because no significant advantages were obtained with the chirp, emphasis was shifted to discrete frequency excitation. Experiments using the latter excitation approach are described in section 5.2.

In the first subsection 5.2.1 discussing discrete frequency excitation, the experiments performed to determine the best exciter and sensor configurations for circumferential scans are described. From these experiments, the 85-degree probe with a vertical sensor orientation was selected. This probe and sensor configuration was then evaluated on specimens having structural variables (subsection 5.2.2) and on specimens supplied by WL/MLLP (subsection 5.2.3). Results from the limited tests using a linear raster scan are described in subsection 5.2.4, and a table that gives an overall summary of the test results from subsections 5.2.2 through 5.2.4 is presented in subsection 5.2.5.

5.1 CHIRP EXCITATION

Examples of the chirp excitation waveform (voltage applied to the exciter coil) and the sensor coil output are shown in Figs. 37a and b. This signal was taken with the probe positioned over a 5.2-mm second-layer flaw (180-degree scan position) in the preliminary specimen with a first-layer thickness of 4.8 mm. The chirp ranges in frequency from 200 Hz to 10 kHz and is swept logarithmically so that more time (and thus energy) is spent at the lower frequencies.

5.1.1 Frequency Spectrum—An example of the frequency spectrum from an FFT of the chirp from Fig. 37b is shown in Fig. 38a. Because of the small effect of the flaw on the overall signal amplitude, the spectrum with the probe positioned over the flaw appears essentially the same as the spectrum where there is no flaw. In order to reveal the flaw signal, the spectrum at the probe starting position (zero degree) was subtracted from the spectrum obtained with the probe over the flaw (180 degrees). The result is shown in Fig. 38b. The response from the flaw is more than two orders of magnitude smaller than the overall response. The flaw response peaks at about 500 Hz, and most of the response occurs between 250 Hz and 1 kHz.

In order to view the spectrum for a circumferential scan around the fastener hole, the subtracted data were converted to a color image, where the color is representative of the FFT
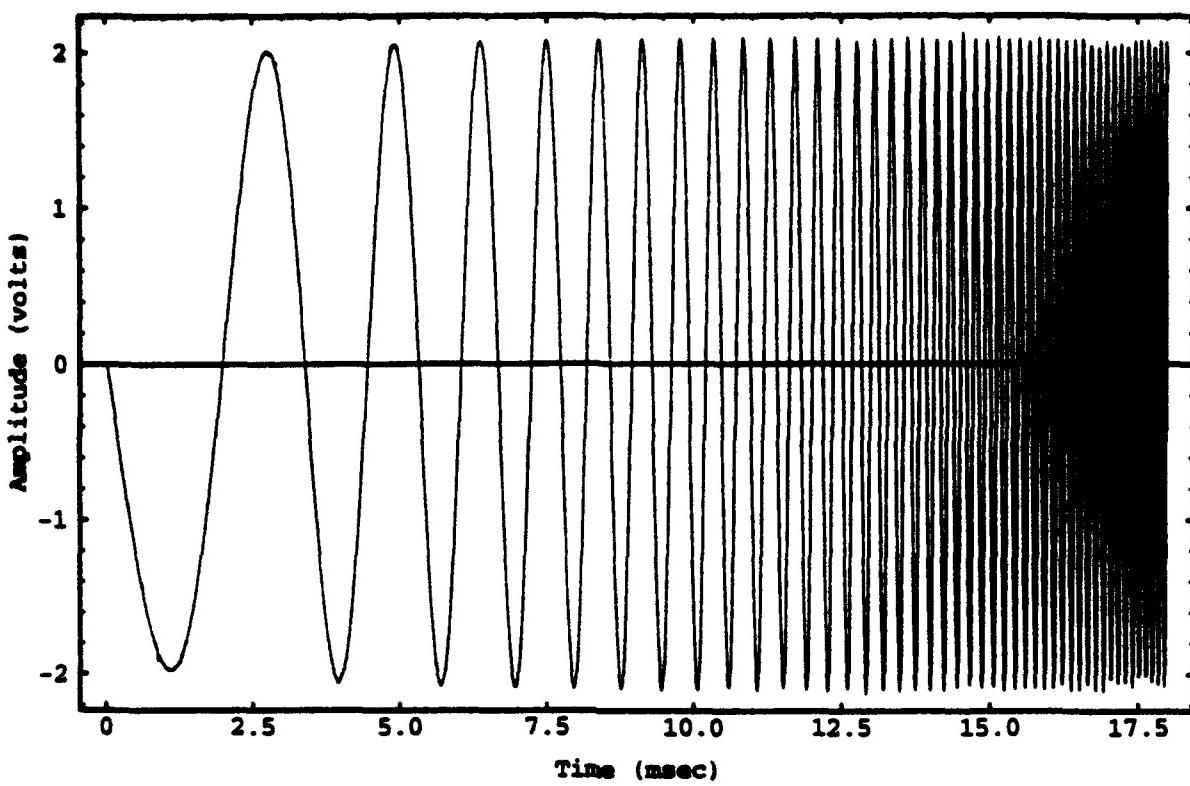
(A)
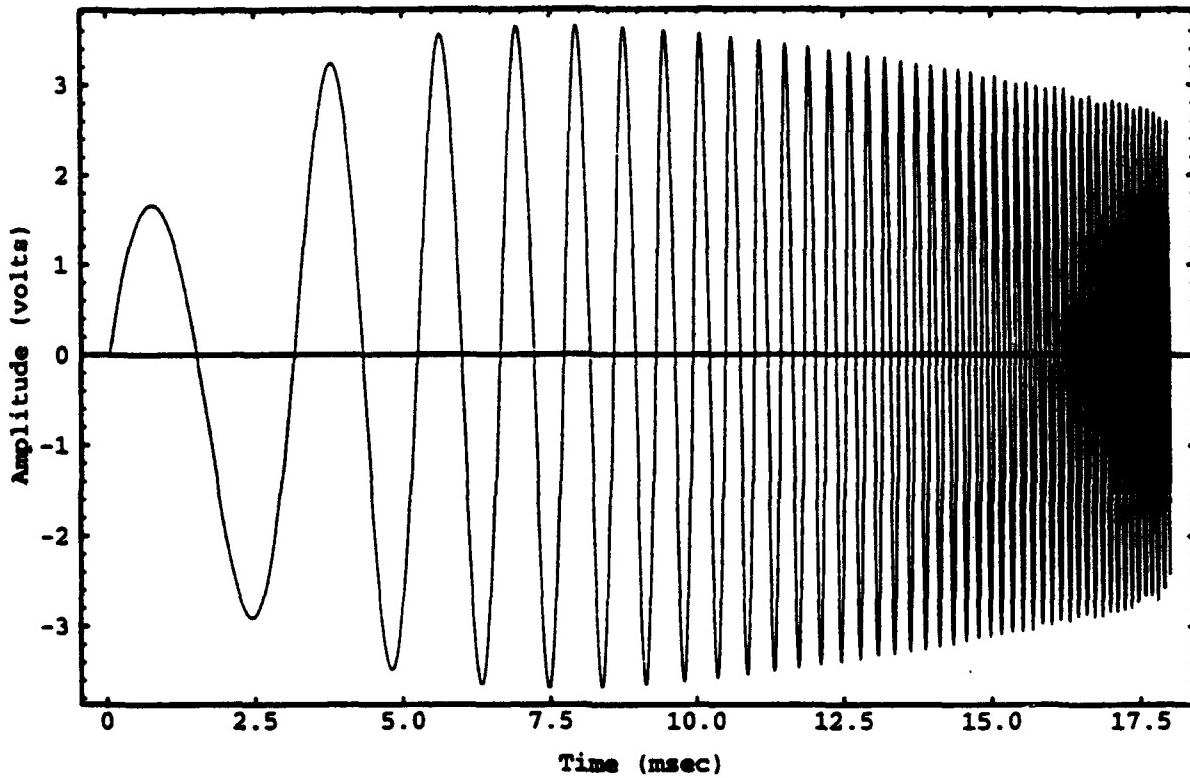
(B)

Figure 37. Examples of chirp waveform (A) excitation. (B) sensor output.
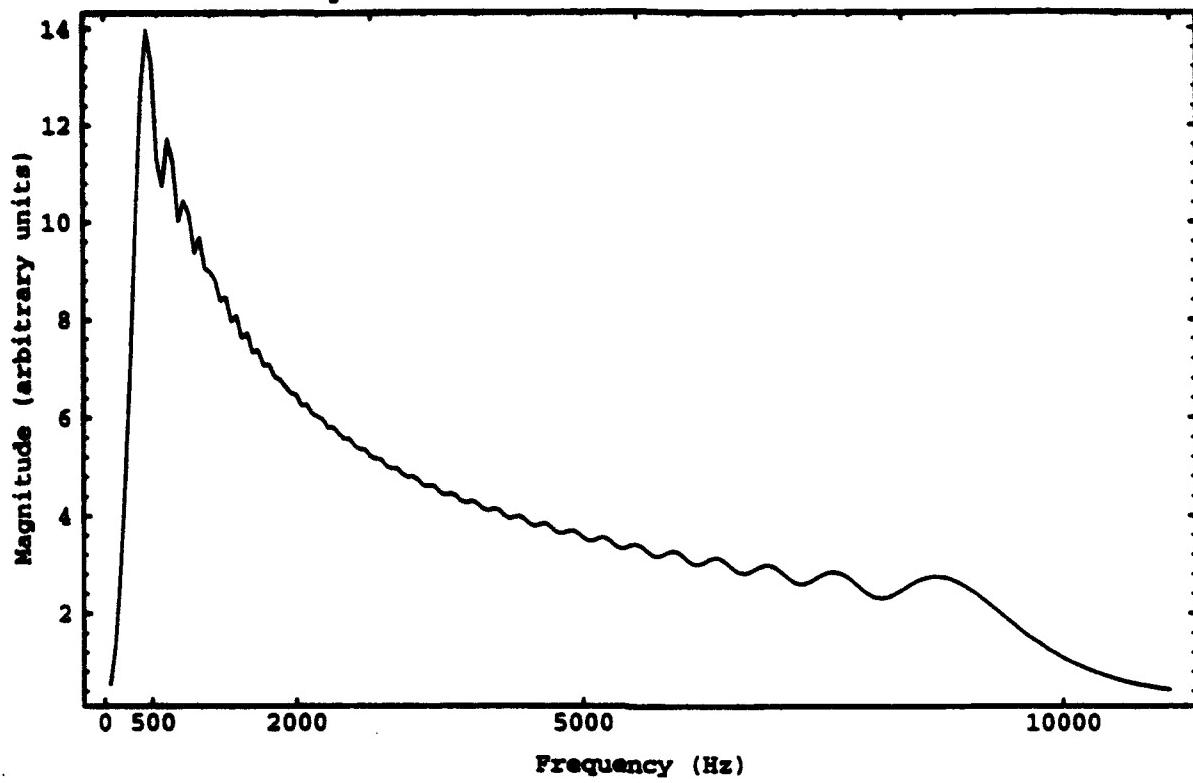
(A)
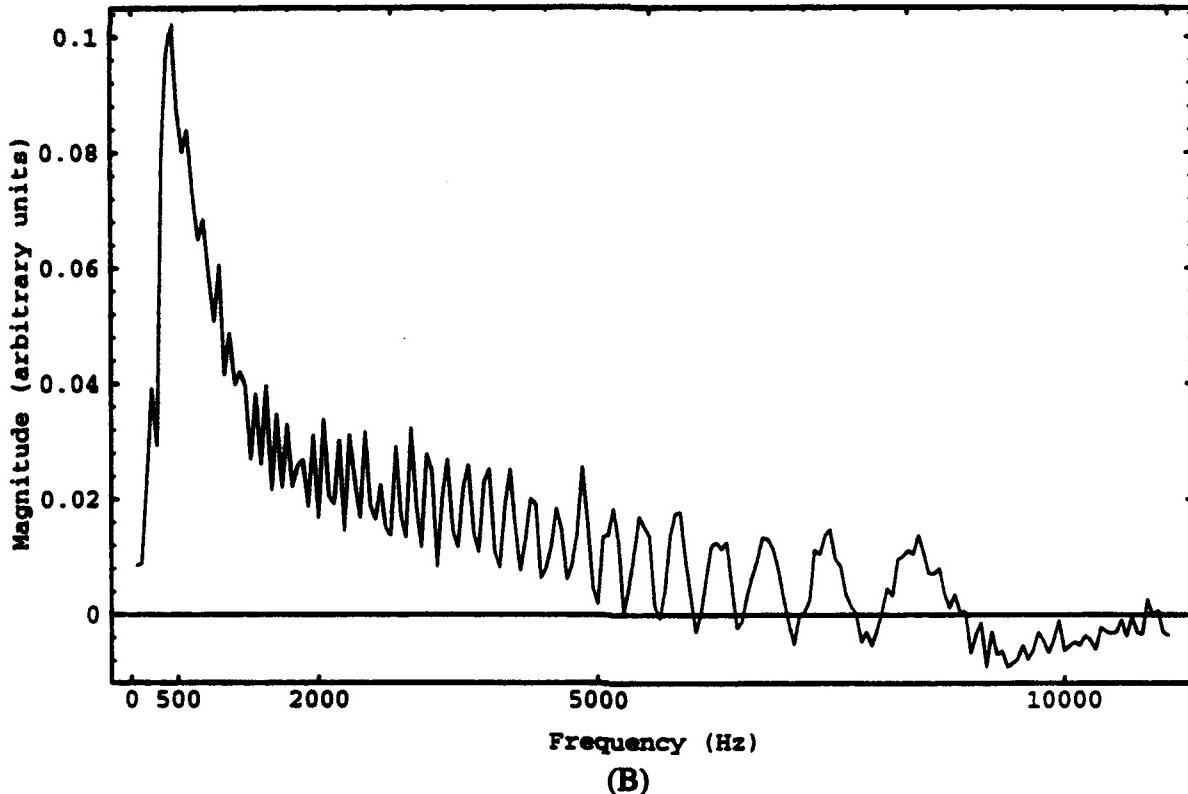
(B)

Figure 38. Frequency spectrum of chirp waveform with probe over 5.2-mm flaw and first-layer thickness of 4.8 mm: (A) overall response. (B) spectrum over flaw minus spectrum with no flaw.

53

spectrum magnitude (highest to lowest amplitudes represented by magenta, blue, green, and yellow, respectively). Fig. 39 shows the results for a circumferential scan of the preliminary specimen with a 3.7-mm-thick first layer configured with a 5.7-mm flaw (Fig. 39a), a second-layer edge (Fig. 39b), and both the flaw and edge (Fig. 39c). These data were taken with the 35-degree probe at a scan radius of 2.5 mm, which is where the best flaw response relative to the edge response was obtained. The data show some differences in the frequency response for the flaw and edge, with the flaw and flaw-plus-edge responses having a stronger signal (magenta) at low frequencies (approximately 500 Hz) and also stronger signals (blue) at somewhat higher frequencies (approximately 1 kHz) compared to the edge only. Thus, for this specimen configuration, the flaw could be distinguished from the edge.

Fig. 40 shows the spectrum for the same specimen configuration, but with a thicker first layer (4.8 mm). In Fig. 40a, the flaw appears primarily as a magenta region between approximately 150 and 200 degrees at low frequencies. In Fig. 40b, the edge also appears as a magenta region which is somewhat smaller along the frequency axis and covers a larger portion of the scan than both the flaw and flaw-plus-edge spectra. In Fig. 40c, there is also a region of high and low amplitude on each side of the flaw-plus-edge-response that extends to higher frequencies and is apparently from the probe rotation being somewhat off center from the axis of the fastener hole. (These data were taken before the centering procedure was based on the eddy current response and only physical alignment was used.) Although some differences are apparent between the responses from the three specimen configurations, they are more subtle that with the 3.7-mm-thick first layer, and it would be difficult to distinguish a flaw from an edge using the spectrum approach.

For detection of the target flaw size (2.5 mm) through the target first-layer thickness (6.4 mm), the differences between flaws and edges would be even more subtle than shown in Fig. 40, and the capability to distinguish a flaw from an edge would be even more limited. For this reason, additional development of the spectrum approach was not undertaken.

5.1.2   Impulse Response—An example of the impulse response obtained from the auto-correlation of the chirp shown in Fig. 37b is shown in Fig. 41a. As with the frequency spectrum, the effect of the flaw on the overall signal amplitude is small, and it was necessary to subtract the response at the probe starting position to reveal the flaw response. The result is shown in Fig. 41b.
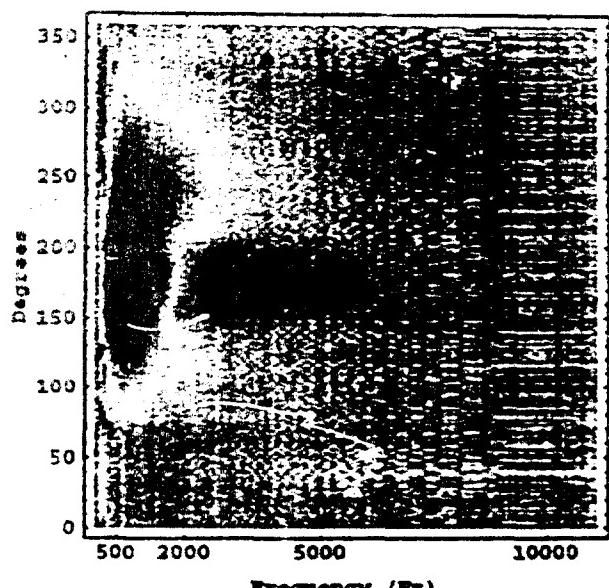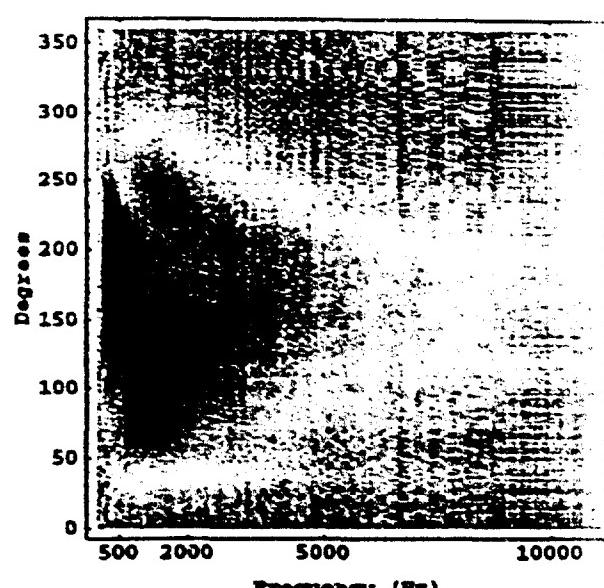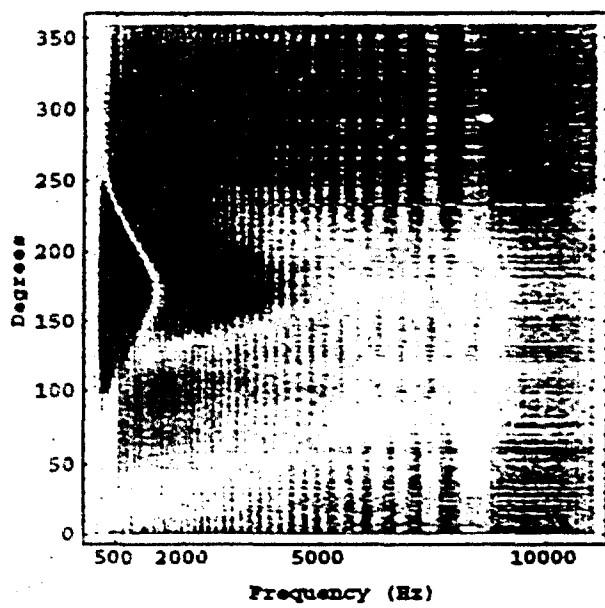
Figure 39. Images of chirp frequency spectrum vs. circumferential position for 3.2-mm first layer: (A) 5.2-mm flaw at 180 degrees; (B) edge at 180 degrees; (C) flaw and edge at 180 degrees.
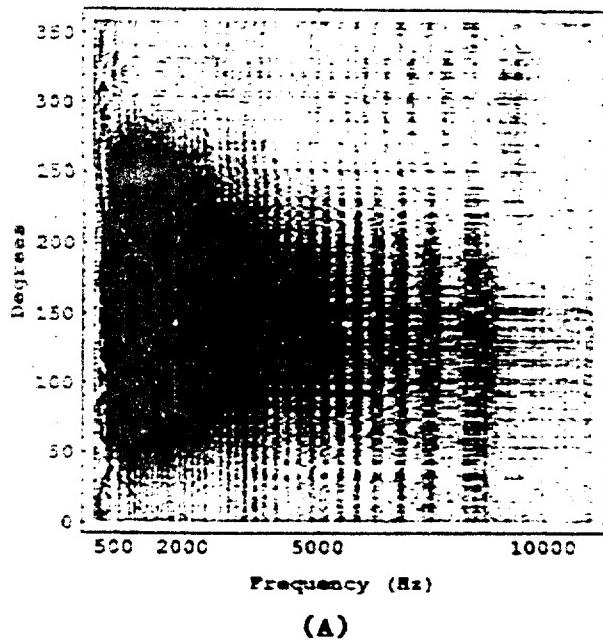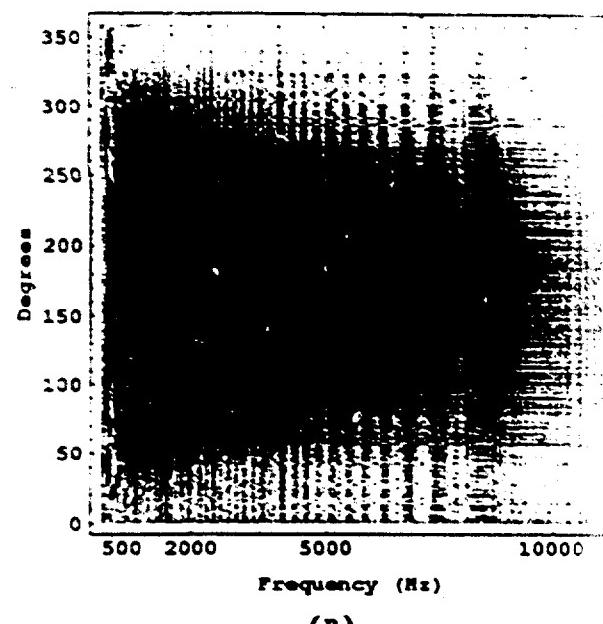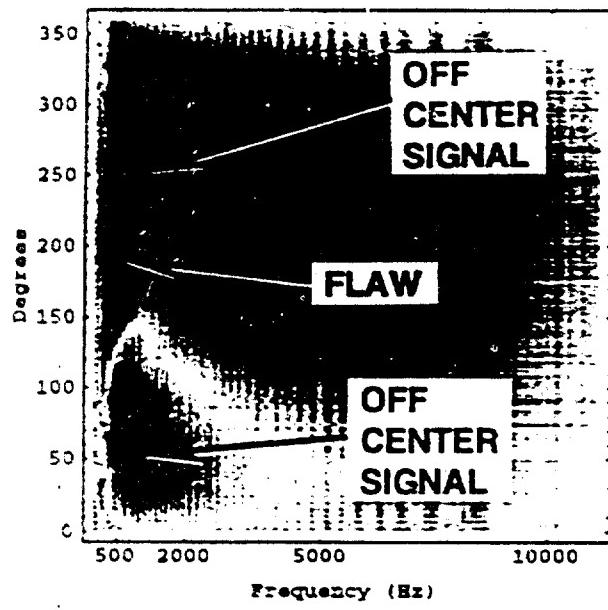
Figure 40.   Images of chirp frequency spectrum vs. circumferential position for 4.8-mm first layer: (A) 5.2-mm flaw at 180 degrees; (B) edge at 180 degrees; (C) flaw and edge at 180 degrees

(NOTE: COLOR COPY AVAILABLE FROM CONTRACTOR)
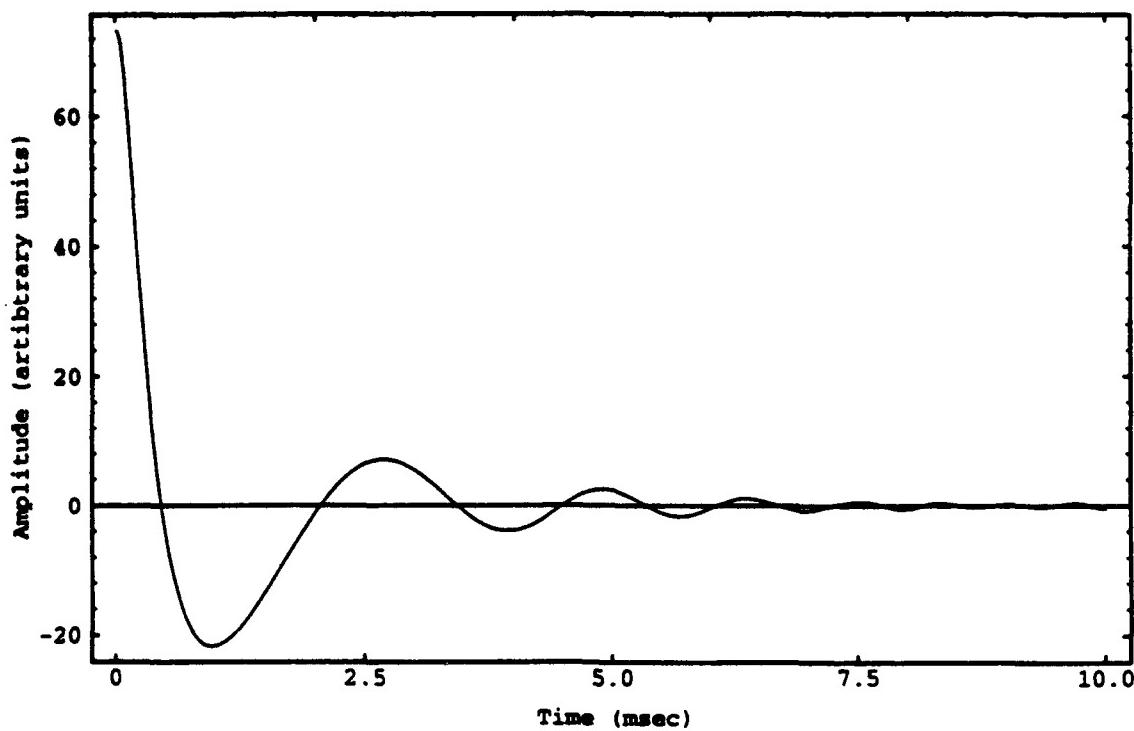
(A)
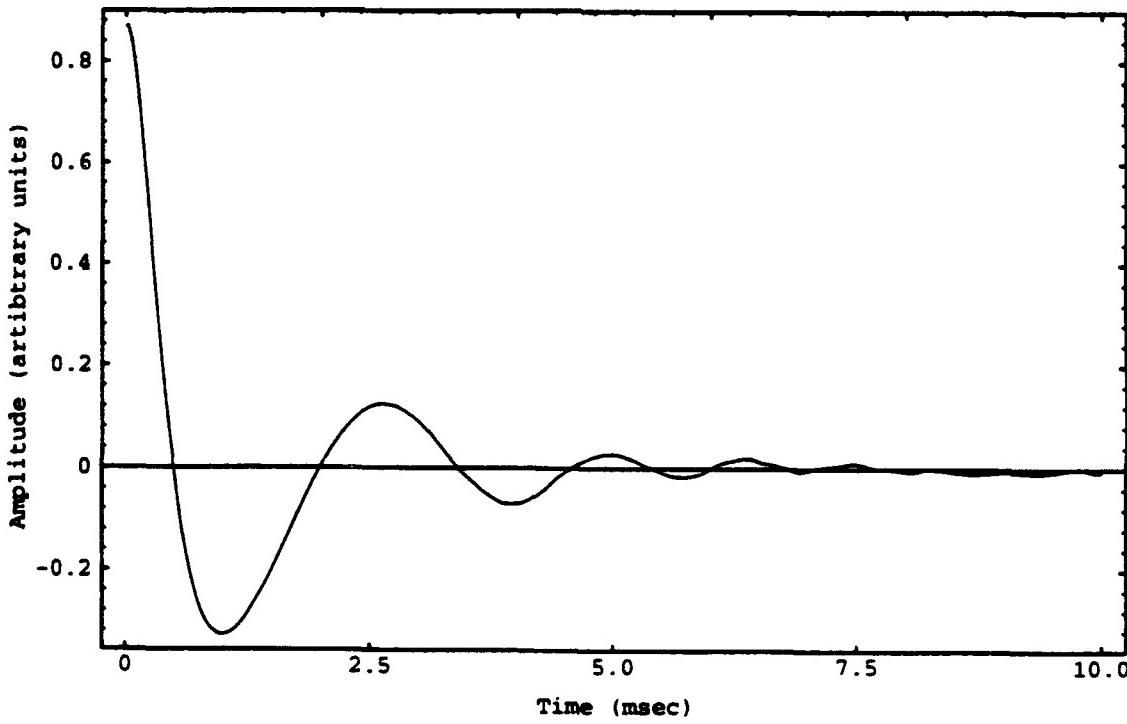
(B)

Figure 41. Impulse response obtained from autocorrelation of chirp waveform with probe over 5.2-mm flaw and first-layer thickness of 4.8 mm: (A) overall response. (B) response with flaw minus response with no flaw.

57

As with the frequency spectrum, the data were converted to a color image to view the impulse response data for a circumferential scan around the fastener hole. Again the highest-to-lowest amplitudes are represented by magenta, blue, green, and yellow. Fig. 42 shows the impulse response for the same data from which the spectrum was obtained in Fig. 40. The first-layer thickness is 4.8 mm, and the specimen is configured with a 5.7-mm flaw only (Fig. 42A), a second-layer edge only (Fig. 42B), and both the flaw and edge (Fig. 42C). The flaw and edge have similar responses (approximately centered around 180 degrees), with the highest amplitudes (magenta and dark blue) occurring at times up to about 20 msec. (As in Fig.40, the flaw-plus-edge data contain a response from off-centering of the probe.) Because of the similarity in responses, it would be difficult to distinguish a flaw from an edge, and thus the impulse response approach was not developed further.

5.2   DISCRETE FREQUENCY EXCITATION

5.2.1   Evaluation of Exciter and Sensor Configurations for Circumferential Scans—Tests were performed to evaluate the 35- and 85-degree exciter configurations and the different sensor orientations and positions. The purpose was to determine the best configuration for flaw detectability and discrimination among responses from flaws and structure. The following configurations were evaluated:

(1)   35-degree exciter with vertical sensor orientation (both air- and ferrite-core sensors) and with a sensor coil wrapped around the outer leg (which also detected the vertical component of the magnetic field) and

(2)   85-degree exciter with radial and circumferential sensors and with a vertical sensor in two radial positions with respect to the exciter (all with air-core sensors).

For simplicity, these tests were performed using a single-frequency excitation at 500 Hz, which produced the best response with the chirp spectrum (Figs. 38b and 39). Data were taken using circumferential scans with increments in the radial direction to produce two-dimensional data. The tests were performed on the simple-geometry specimens with top and bottom layer thicknesses of 4.8 and 6.4 mm, respectively and with a 5.2-mm flaw in the second layer.
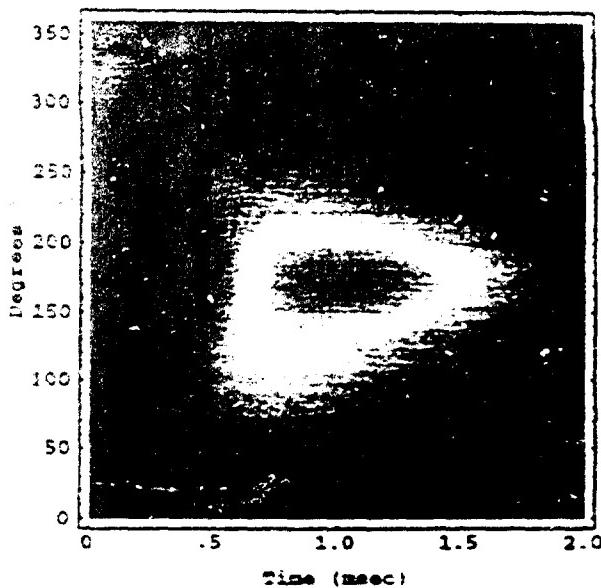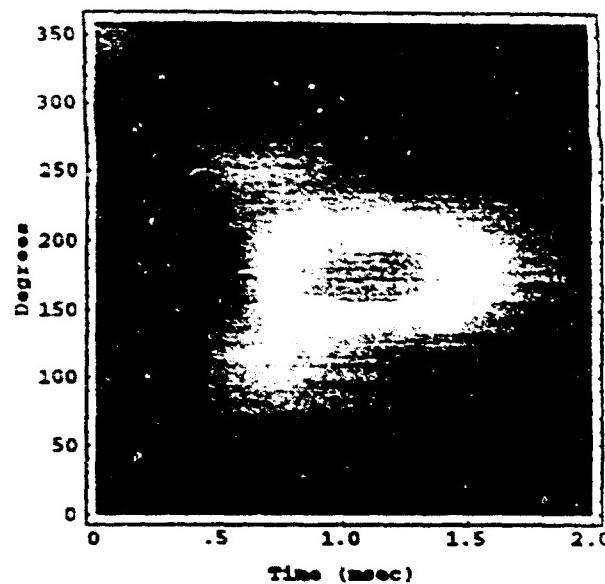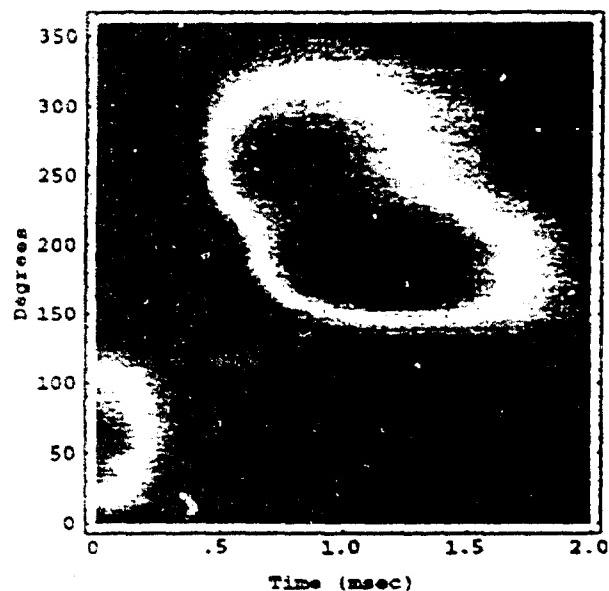
Figure 42. Images of impulse response vs. circumferential position for 4.8-mm first layer: (A) 5.2-mm flaw at 180 degrees; (B) edge at 180 degrees; (C) flaw and edge at 180 degrees.

An air-core sensor in the vertical orientation located adjacent to the outer leg of the exciter gave the best overall results. Disadvantages of the other sensor configurations were as follows. The ferrite core sensor caused additional coupling of the exciter main magnetic field into the sensor, which resulted in excessive offset in the detected signal. The sensor coil wound on the outer leg of the 35-degree probe produced very broad signals in the circumferential scan direction, so it had poor spatial resolution. The model did show that a radial sensor orientation would provide an improved flaw response compared to second-layer geometric response, but the disadvantage was the large coupling of the main magnetic field from the exciter into the sensor (since the coil axis was aligned with the field direction). To avoid saturation, the amplifier gain had to be reduced; and the resulting signal-to-noise ratio was poor. The circumferential sensor orientation produced very weak flaw signals, and the signals had a bipolar response spread over a large portion of the circumference, which reduced the spatial resolution.

A comparison of the 35- and 85-degree probe responses (both with the air-core sensor in the vertical orientation located near the outer leg of the exciter core) is shown in Figs. 43 and 44, respectively, for a first-layer thickness of 4.8 mm and a 5.2-mm flaw. The figures show color images of the responses from specimen configurations with a flaw and no edge, a second-layer edge only, and a flaw and second-layer edge. The 35-degree probe produced a distinct positive, high-amplitude signal polarity (red region) from the flaw and an arc-shaped yellow (lower amplitude) region from the edge. When both the flaw and edge were present, a region of the edge response increased in amplitude and became red. Although these patterns allowed the flaw to be distinguished from an edge, the signals overlapped. Also, the signals were somewhat noisy because of the low signal levels obtained with this probe.

With the 85-degree probe (Fig. 44), the flaw response was located at smaller radii and appeared primarily red (high-amplitude, positive signal polarity), although a small region of blue (negative polarity) also appeared at larger radii. (The background color in these images is yellow, since the color scale covers a different range to accommodate the positive polarity from the flaw signal as well as the negative polarity from the edge.) The edge response (with or without a flaw) appeared blue, is located at larger radii, and is separated from the flaw. Thus, the 85-degree probe offered better discrimination between a flaw and an edge. Also, the signal levels obtained with the 85-degree probe were larger than with the 35-degree probe, and the signals were much less noisy. This indicated that the model did correctly predict that the 85-degree probe produced a higher current density deeper in the second layer (Figs. 7 and 8 in subsection 2.1.1). Based on the better
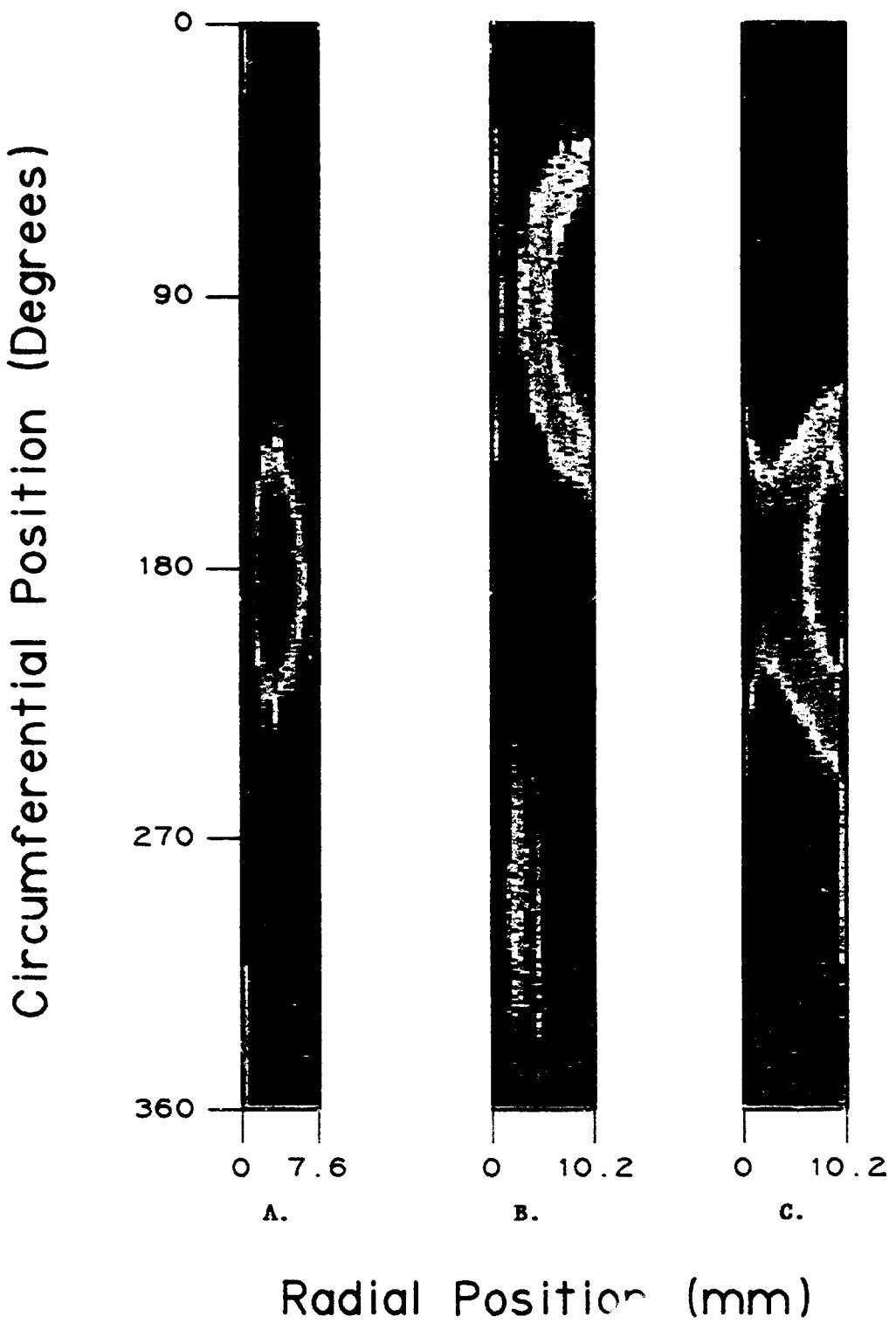
Figure 43. Images of single-frequency (500-Hz) excitation data vs. circumferential and radial position for a 4.8-mm first layer taken with 35-degree probe: (A) 5.2-mm flaw at 180 degrees, (B) edge at 180 degrees, (C) 5.2-mm flaw and edge at 180 degrees.

(NOTE: COLOR COPY AVAILABLE FROM CONTRACTOR)

61
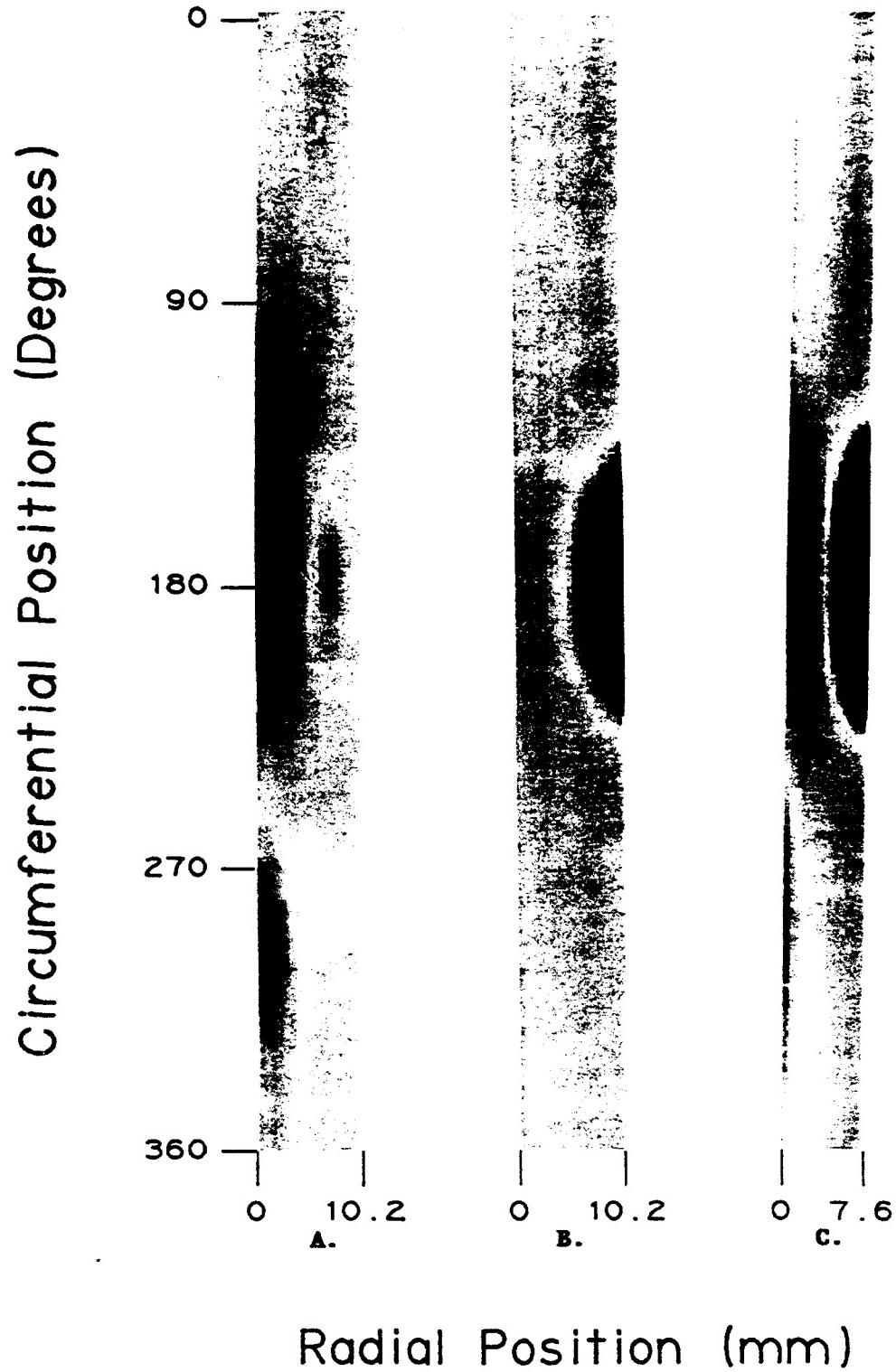
Figure 44. Images of single-frequency (500-Hz) excitation data vs. circumferential and radial position for a 4.8-mm first layer taken with 85-degree probe: (A) 5.2-mm flaw at 180 degrees, (B) edge at 180 degrees, (C) 5.2-mm flaw and edge at 180 degrees.

(NOTE: COLOR COPY AVAILABLE FROM CONTRACTOR)

results achieved with the 85-degree probe, this probe was selected for further evaluation. The results are described as follows.

5.2.2   85-Degree Probe Results for Structure Variables-Specimens A and B—Tests were performed with the 85-degree probe on specimens A and B, which contained structural variables (e.g., second-layer edge and first-layer edge). Emphasis was placed on the specimens with the thickest (6.4-mm) layers, since the thicker layers represented the most difficult case. The experimental results are presented below in different categories according to the structural variable. The results are for 6.4-mm layers and titanium fasteners unless otherwise designated. In the figures, the color scale has some differences from one structural variable to the next; however, the scale is the same for all data in a single figure. Unless otherwise designated, the data were taken at either 250 or 500 Hz and rotated in phase to produce the best results for the particular structure. As with the color scale, all conditions are the same for all the data in a given figure.

(1)   Second-Layer Edge—Data from holes 9, 10, and 11 in specimen A (with 6.4-mm-thick layers) with the closest (12.7-mm) hole-to-edge spacing are shown in Figs. 45(A), 45(B), and 45(C), respectively. The edge and the flaws are both at 180-degree circumferential location in the scan. The edge shows up as a dark blue (high-amplitude, negative signal polarity) region centered around 180 degrees at the bottom (large scan radius) of the image. The edge also produces some areas of yellow and orange (positive signal polarity) toward the bottom of the image and a region of yellow around 180 degrees near the top (small radii) of the image [Fig. 45(C)]. The 3.8-mm flaw [Fig. 45(A)] produces a distinct high-amplitude (red) region around 180 degrees near the top of the image, and the 2.5-mm flaw [Fig. 45(B)] produces a moderate-amplitude (orange) region. The 3.8-mm flaw produces a distinct peak in a strip-chart signal; and the 2.5-mm flaw also produces a distinct peak, although it is more diffuse. Both flaws are readily detectable and can be distinguished from the edge.

Another approach to presentation of the image is to remove the portion near the bottom, which contains much of the edge signal. The result, shown in Fig. 46, was made from the same data as Fig. 45 but only shows the data at small radii. The color scale is also slightly different from Fig. 45. Here, little signal from the edge is seen, and the flaw signals are distinct.

(2)   First-Layer Edge—Data from holes 17, 18, and 19 in specimen A with the intermediate (16-mm) hole-to-first layer edge spacing are shown in Figs. 47(A), 47(B), and 47(C), respectively. The edge and flaws are at 180-degree circumferential location in the image. The

63
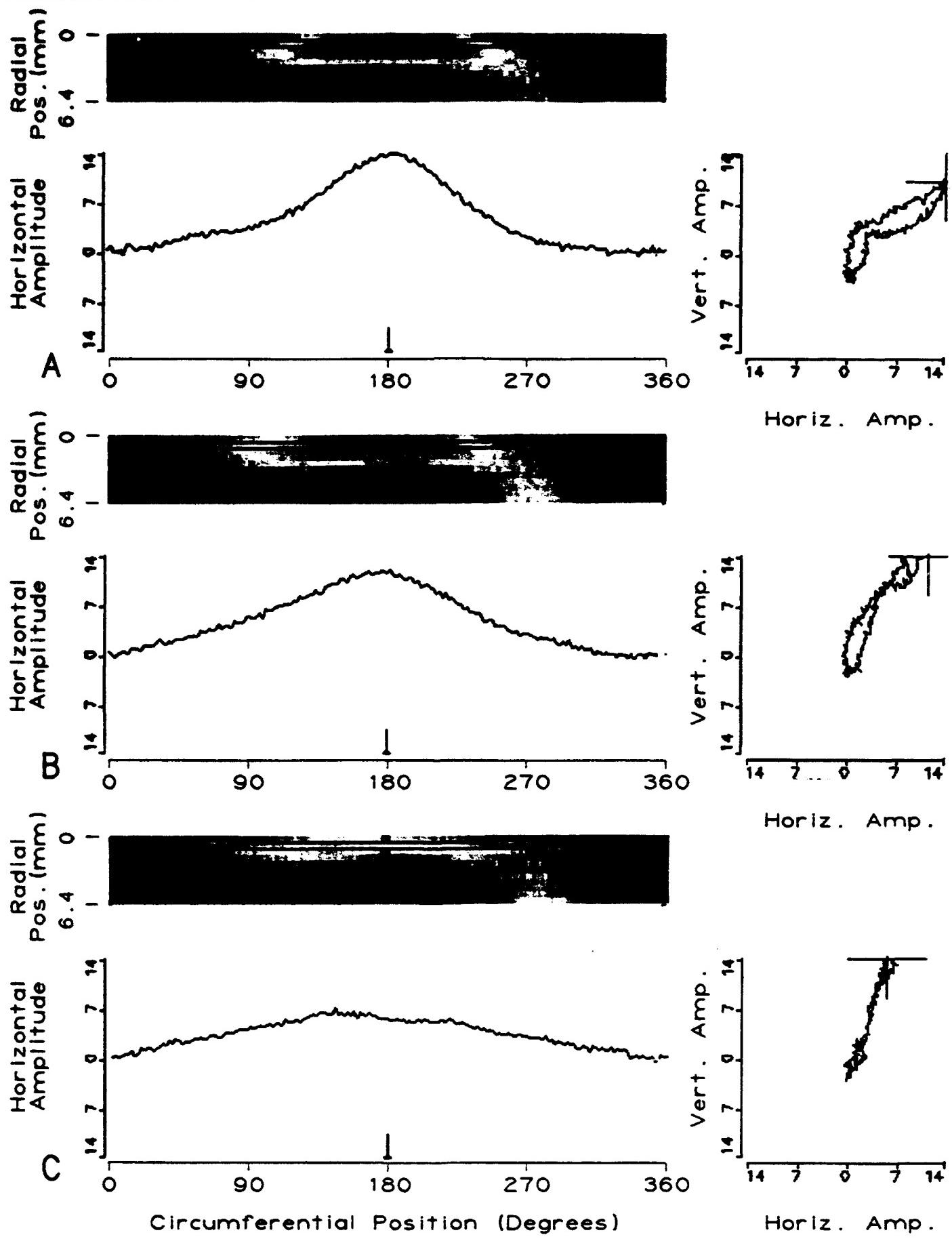
Figure 45. Data from specimen A with second-layer edge at 180 degrees: (A) hole 9 with 3.8-mm flaw at 180 degrees; (B) hole 10 with 2.5-mm flaw at 180 degrees; (C) hole 11 with edge only. Color scale ranges from -7 (blue) to 15 (red) relative to the strip-chart scale.
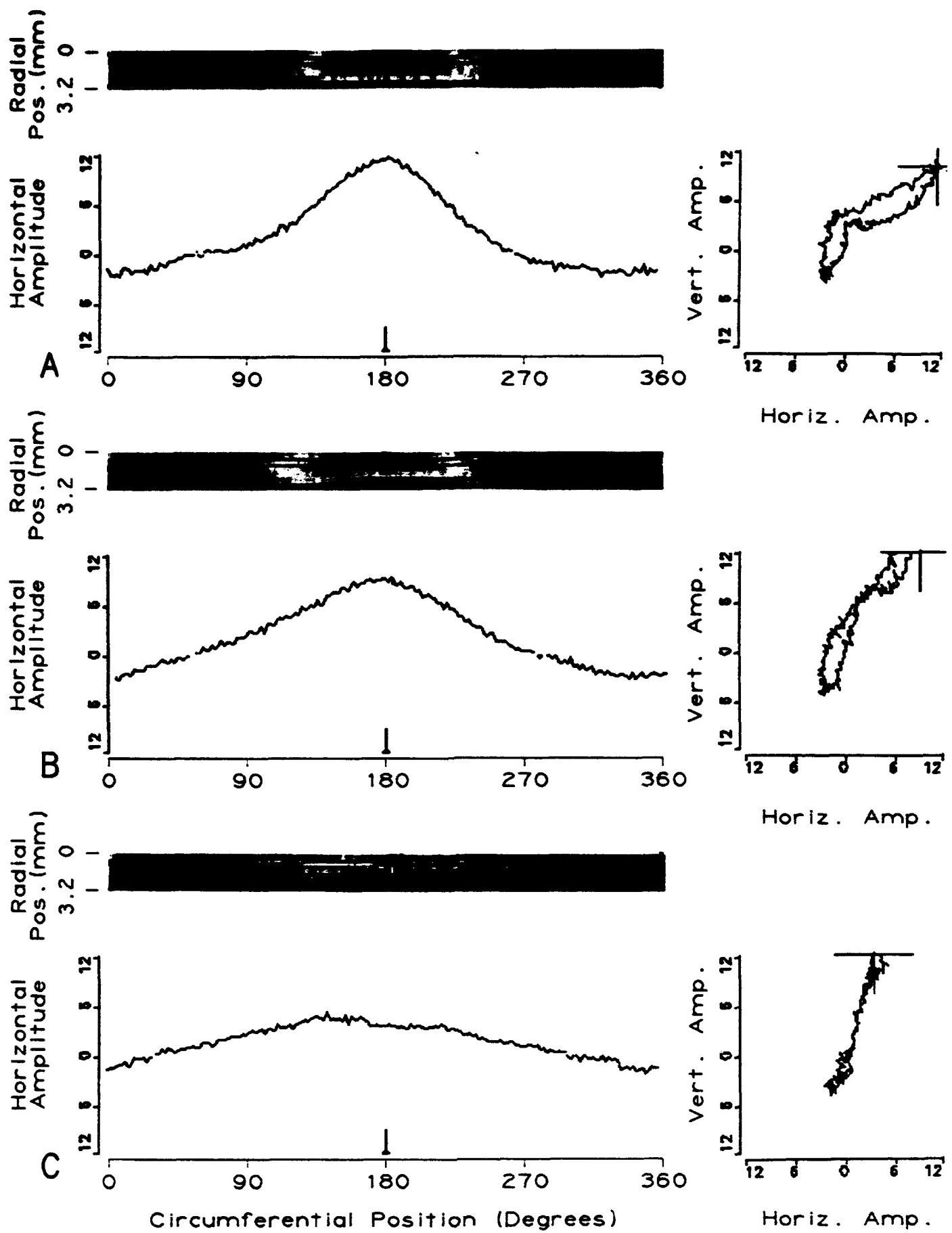
Figure 46. Data from Fig. 45 with scans at large radii removed: specimen A with second-layer edge at 180 degrees: (A) hole 9 with 3.8-mm flaw at 180 degrees: (B) hole 10 with 2.5-mm flaw at 180 degrees: (C) hole 11 with edge only. Color scale: -5 to 12.
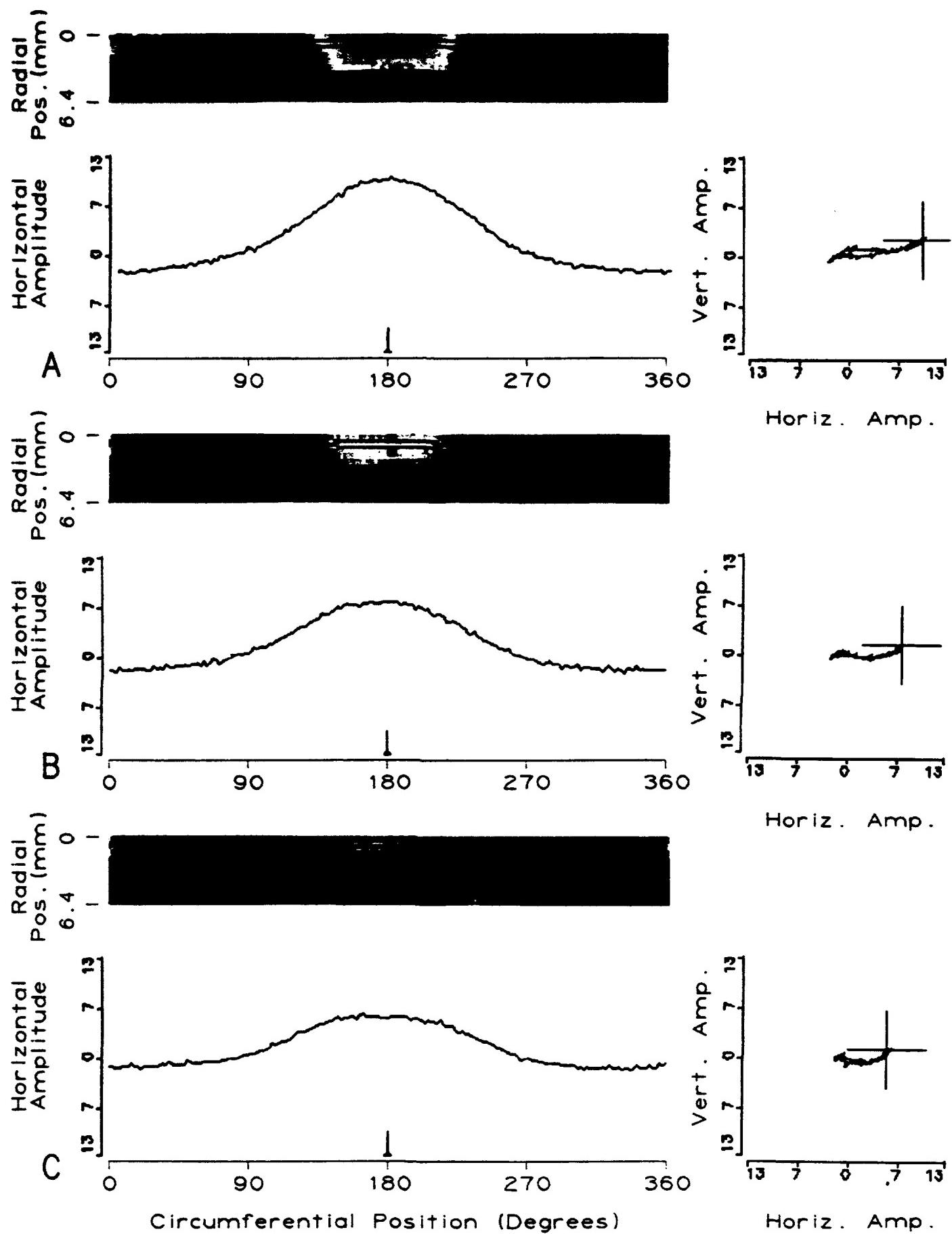
Figure 47. Data from specimen A with first-layer edge at 180 degrees: (A) hole 17 with 3.8-mm flaw at 180 degrees; (B) hole 18 with 2.5-mm flaw at 180 degrees; (C) hole 19 with edge only. Color scale: 0 to 12.

signal from the first-layer edge is much stronger than that from the second-layer edge. The color scale was adjusted somewhat to make the flaw signals more apparent. The scale ranges from 0 to 12; therefore, the entire negative portion of the signal is dark blue in the color image. The edge produces a similar pattern as did the second-layer edge, i.e., a dark blue region near the bottom of the image (large radii). The 3.8- and 2.5-mm flaws are apparent as red and orange regions in Figs. 47(A) and 47(B), respectively. Fig. 48 shows the same data as Fig. 47, but with the large radii scans removed to show the flaw signals more clearly. The strip-chart signals show peaks from the flaws, but the edge also produces a peak. The 3.8-mm flaw is significantly larger than that from the edge, but the 2.5-mm peak is only slightly greater. In practice, consistently distinguishing a 2.5-mm flaw from an edge may be difficult without additional signal processing.

The close hole-to-first layer edge spacing (holes 20, 21, and 22) was not tested in the 6.4-mm-thick specimen. However, data were taken from the 4.8-mm-thick specimen, and analysis of these data indicated that flaws would be difficult to detect with this spacing without further signal processing.

(3) Flaw Orientation (Second-Layer Edge)—Data obtained from holes 8 and 9 in specimen B with a second-layer edge (intermediate hole-to-edge spacing) and flaws oriented 90 degrees from the edge are shown in Figs. 49(A) and 49(B). In these figures, the flaw is at 90 degrees, and the edge is at 180 degrees. The 3.8-mm flaw is very apparent in Fig. 49(A) as a distinct red area in the image and a peak in the strip chart at 90 degrees. The 2.5-mm flaw also is apparent in Fig. 49(B) as a slightly orange region in the image and a peak in the strip chart at 90 degrees, but another orange region and increase in strip-chart signal level also showed up at 180 degrees where the edge is located. The origin of the signal at 180 degrees in Fig. 49(B) is not clear. The edge possibly was the cause, but the edge did not show up in the data in Fig. 49(A), which were taken under the same conditions. One possibility is off-centering of the probe. Analysis of this result will require further investigation.

(4) Adjacent Fastener Holes—Data from holes with adjacent fasteners having closer spacing than in the tests above were obtained from holes 16 and 17 in specimen B (spacing dimensions are shown in Fig. 23). Images of the data are shown in Figs. 50(A) and 50(B). The flaws are located at 90 degrees in the image. The 3.8- and 2.5-mm flaws in Figs. 50(A) and 50(B) were apparent as red and slightly orange regions, respectively, (and as positive peaks in the strip-chart signals) even though the flaws were located toward adjacent fasteners. The spacings between
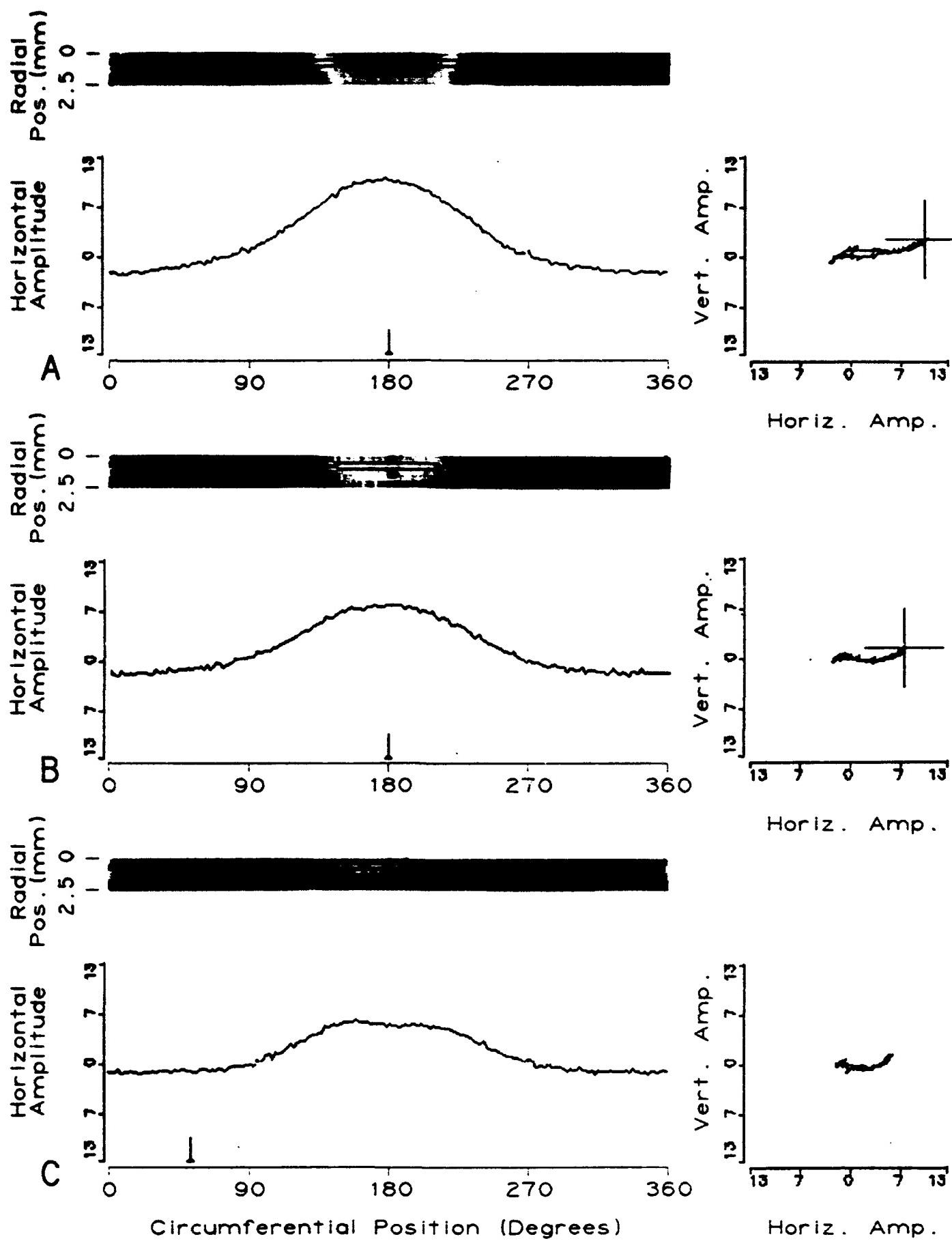
Figure 48. Data from Fig. 47 with scans at large radii removed. Specimen A with first-layer edge at 180 degrees: (A) hole 17 with 3.8-mm flaw at 180 degrees: (B) hole 18 with 2.5-mm flaw at 180 degrees: (C) hole 19 with edge only. Color scale: 0 to 12.
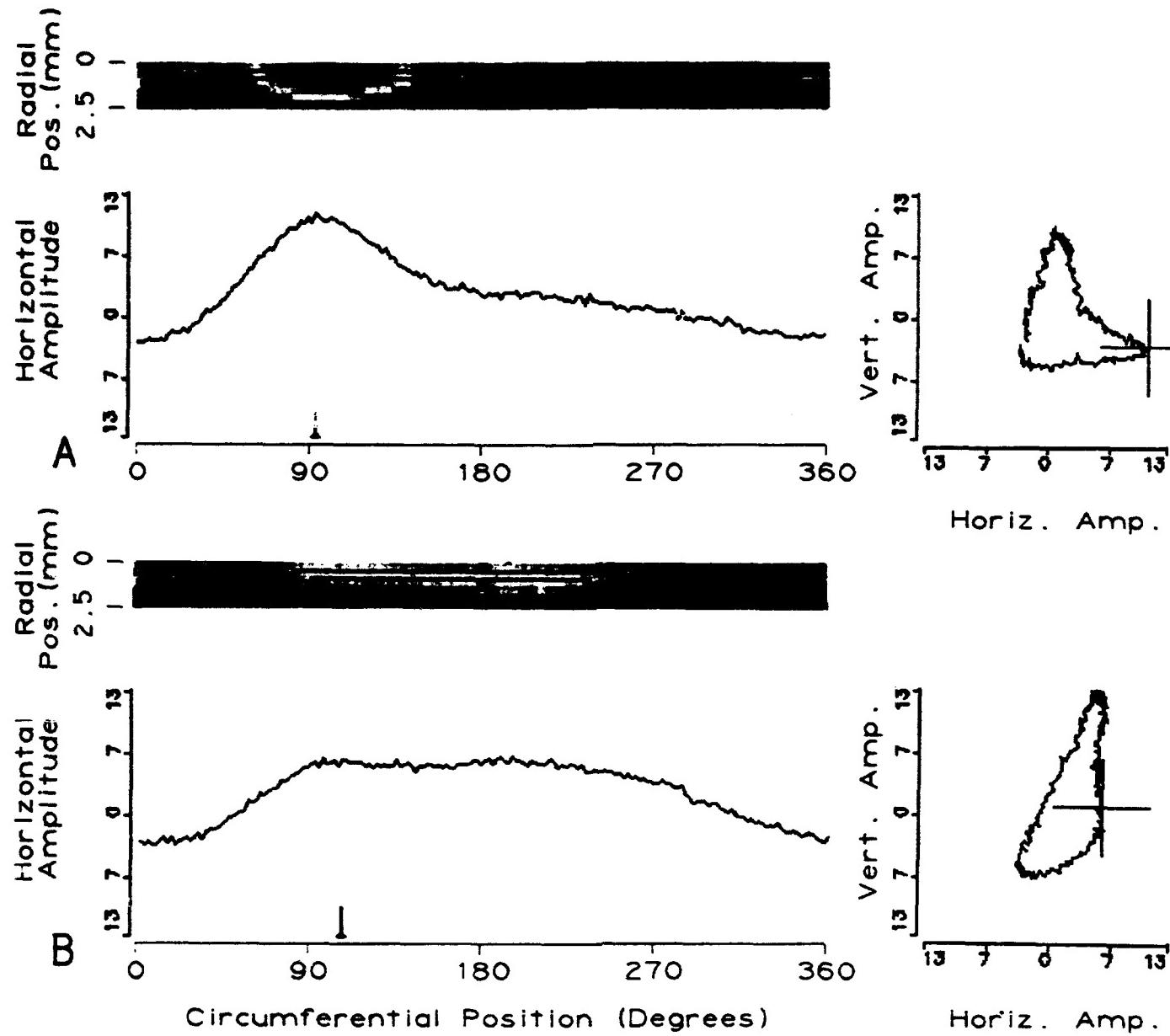
Figure 49. Data from specimen B with second-layer edge at 180 degrees and different flaw orientations: (A) hole 8 with 3.8-mm flaw at 90 degrees. (B) hole 9 with 2.5-mm flaw at 90 degrees. Color scale: -3 to 12.

(NOTE: COLOR COPY AVAILABLE FROM CONTRACTOR)
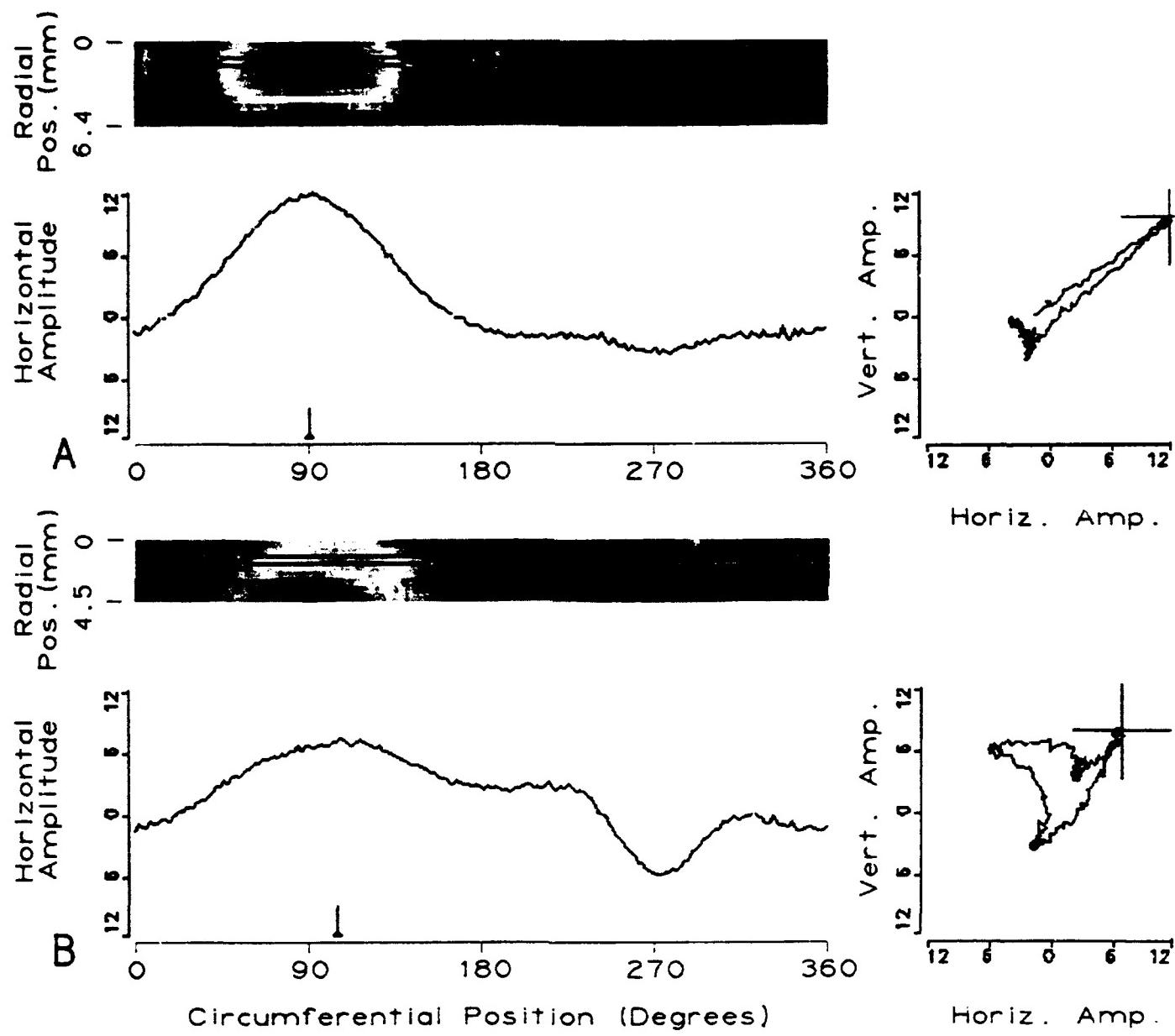
Figure 50. Data from specimen B with adjacent fasteners at 90 and 270 degrees: (A) hole 15 with 3.8-mm flaw at 90 degrees. (B) hole 16 with 2.5-mm flaw at 90 degrees. Color scale: -4 to 13.

(NOTE: COLOR COPY AVAILABLE FROM CONTRACTOR)

the holes with the flaws and adjacent holes are 22.2 and 25.4 mm for the 2.5- and 3.8-mm flaws, respectively. Figs. 50(A) and 50(B) also contain responses from adjacent holes at circumferential locations (270 degrees) where no flaws exist. Here, the hole response is dark blue (negative polarity) and can be distinguished from the positive-polarity flaw responses at 270 degrees. The hole-to-hole spacing at this location (270 degrees) was 22.2 mm for Fig. 50(A), which corresponded to the spacing at the location of the 2.5-mm flaw in Fig. 50(B). The spacing for Fig. 50(B) (at 270 degrees) was 19 mm, which was closer than the spacing at either of the flaw locations.

(5) Fastener Size—The data described in the above sections were obtained from 6.4-mm-diameter fasteners. Fastener holes of two different diameters were also tested. Figs. 51(A) and 51(B) show images of the data from holes 3 and 5 in specimen B, respectively, for 4.8- and 7.9-mm fastener holes. Both holes contained 2.5-mm flaws, which were readily apparent in the image as a red area at 180 degrees.

(6) Steel Fasteners—The modeling predicted that the segment-core probe configuration, when used with steel (magnetic) fasteners, would produce a region of high current density near each edge of the probe outer leg with a reduced density in the center (Fig. 10). An alternate probe design (Fig. 11) was shown to produce a single region of high current density under the center of the outer leg. Experimental results with the segment-core probe using the preliminary specimens indicated that the result predicted by the model occurred with very thin first layers, but with thicker layers, a response similar to one from nonmagnetic fasteners was obtained. Because of this result, and the complexity and predicted low eddy current density of the alternate probe design, the experiments proceeded with the segment-core probe.

Some difficulty was encountered with steel fasteners, primarily because the magnetic response of the steel fastener caused errors in centering the probe (using the centering procedure described in subsection 3.4.2) over the fastener. The magnetic response was nonuniform, and in some cases, residual magnetic fields were present in the fastener. This resulted in the centering error where the probe was actually located off true center, even though the centering procedure indicated it was centered. Evidence of the centering problem was apparent if the probe were centered when a titanium fastener was located in the hole. If the titanium fastener were replaced with a steel one, the centering operation would place the probe in a physically different location. In some cases, some improvement could be made by demagnetizing the fastener before centering. The spurious signals caused by off-centering would tend to mask the flaw signals.
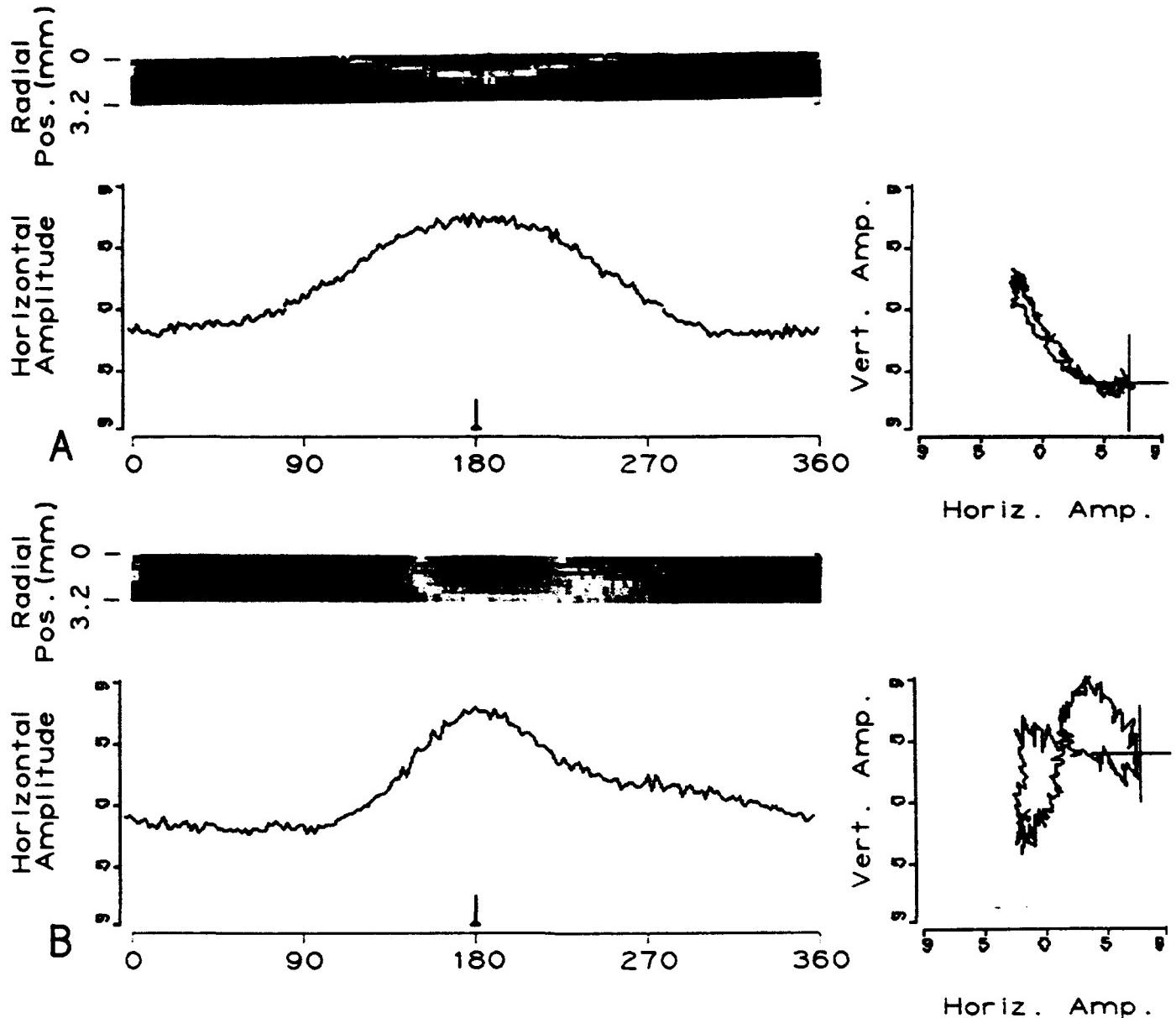
Figure 51. Data from holes in specimen B with different fastener sizes: (A) hole 3, 4.8-mm diameter with 2.5-mm flaw at 180 degrees. (B) hole 5, 7.9-mm diameter with 2.5-mm flaw at 180 degrees. Color scale: (A) -1 to 6. (B) -2 to 7.

(NOTE: COLOR COPY AVAILABLE FROM CONTRACTOR)

As described in subsection 3.2.1, the use of a conductive shield was investigated as a means of reducing the direct flux path between the fastener head and sensor coil. We believed that the flux path from the center leg through the fastener head and to the outer leg (as well as the sensor) could aggravate the centering problem. The problem occurred because the magnetic fastener head would make this a much more preferable path than with a nonmagnetic fastener. Variations in the magnetic response of the fastener head would then make a large contribution to the sensed signal through this path.

The probe was modified by adding a copper ring concentric with the center leg of the exciter core and located between the center leg and the sensor. This did not significantly help the centering situation, but did reduce the direct coupling of the exciter magnetic field into the sensor. With this coupling reduced, the amplifier gain could be increased as well as the ratio of flaw-signal amplitude to electronic noise amplitude.

Tests were conducted using the conductive shield with steel fasteners in holes 9, 10, and 11 in specimen A (Fig. 52) with 6.4-mm-thick layers; these holes are located near a second-layer edge. Figs. 52A, 52B, and 52C show data obtained from these three fastener holes, respectively. In these color images, the 3.8-mm flaw (Fig. 52A) showed up well as a red/orange region at 180 degrees in the scan (the location of the flaw and the second-layer edge). The hole with the 2.5-mm flaw (Fig. 52B) showed an orange region, which looked similar to a flaw response, except it was not located at the flaw position at 180 degrees. The unflawed hole also showed as a yellow region, which could be caused by the second-layer edge except it is not at the edge location. Also, the portion of the image from small scan radii (primarily R=0) showed a large color variation from red/orange to blue (especially for holes 9 and 10). This indicated a large fluctuation in signal when the probe was near the fastener; these signal fluctuations were not related to the presence of flaws.

Examination of the strip-chart signals from the fourth scan row (R=1.9 mm, location of the small rectangle in the image) showed signal shapes resembling a sine wave. We believe this is a result of the probe rotation being off the fastener center, as noncentered scans have been shown to give a sinusoidal response. For an off-center scan of a flawed hole, the result was a sinusoidal-shaped signal with the flaw signal superimposed on it. Depending on where the flaw-signal peak occurred with respect to the positive peak in the sinusoid, the flaw may or may not be detected above the sinusoidal background signal.
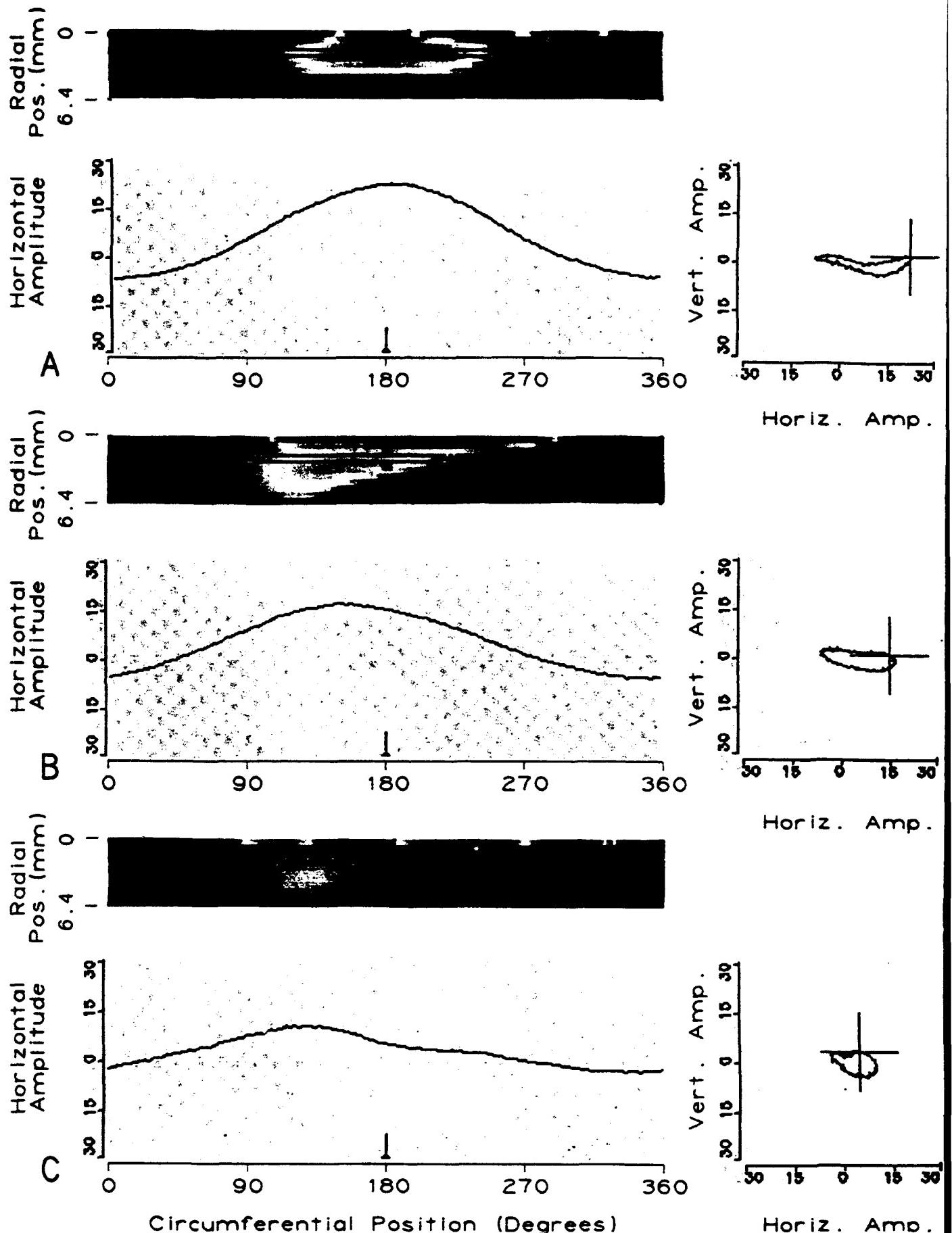
Figure 52. Color image, single-scan strip-chart and single-scan impedance data from specimen A with steel fasteners and second-layer edge at 180 degrees: (A) hole 9 with 3.8-mm flaw at 180 degrees, (B) hole 10 with 2.5-mm flaw at 180 degrees, (C) hole 11 with edge only. Color scale: -8 to 30 relative to the strip-chart scale.

(NOTE: COLOR COPY AVAILABLE FROM CONTRACTOR)

Mixing was applied to the data in Fig. 52 using a combination of data taken at 500 Hz and 2 kHz, and the results are shown in Fig. 53. Although the scale in Fig. 52 is different from that in Fig. 53 because of the mixing, the scale is consistent for all of the images in each figure. The unflawed hole response in Fig. 53C is now flatter in the strip chart, as expected; and the corresponding color image shows no distinct signal. The 3.8-mm flaw signal is very pronounced in both the strip chart and color image in Fig. 53A, and it has a sharper peak than in Fig. 52A. The signal-to-background ratio (ratio of the signal amplitude from the flawed hole to that from the unflawed hole) was approximately 2.6 to 1. The 2.5-mm flaw also produced a recognizable signal with a signal-to-background ratio of 2 to 1. These results indicated that two-frequency mixing can effectively remove the off-centering signals caused by the steel fasteners.

5.2.3   85-Degree Probe Results for WL/MLLP Specimens

(1)   Specimen A3-19—Tests were performed on three unflawed and one flawed fastener hole in specimen A3-19. This specimen consisted of a 4-mm-thick first layer and a 2.5-mm-thick second layer, and hole 6 contained a 2.6-mm fatigue crack in the bottom surface of the second layer. The hole-to-hole spacing was 19 mm, which is closer than the closest spacing in specimen B (22.2 mm). The eddy current response is dominated by the signals from the adjacent fasteners, which produce large peaks in the strip-chart signal (and corresponding red regions in the image) at 90 and 270 degrees in the scan. The closer spacing of these fasteners contributes to the large signals. The signal from the flaw is present at 180 degrees in the response in Fig. 54C and shows up in the strip chart as a definite increase in the signal level at 180 degrees compared to the unflawed holes (Figs. 54A, 54B, and 54D). Unfortunately, because of the large signals from the adjacent fasteners, the flaw signal is not as distinct as in the other specimens described previously because its signal level is not greater than the fastener signals. Other contributing factors may be that the flaw response is reduced because the flaw is a crack instead of a notch and that more of the crack interfacial area is located toward the bottom side of the second layer.

In the color image, the flaw does appear as a change to orange color at 180 degrees compared to the unflawed holes, which are blue to green. Thus the flaw can be detected by comparing the response to adjacent holes but cannot be detected absolutely without this comparison.

Two-frequency mixing was investigated as a means for reducing the adjacent fastener signals, but the results did not provide improvement. Because the same mix coefficients are
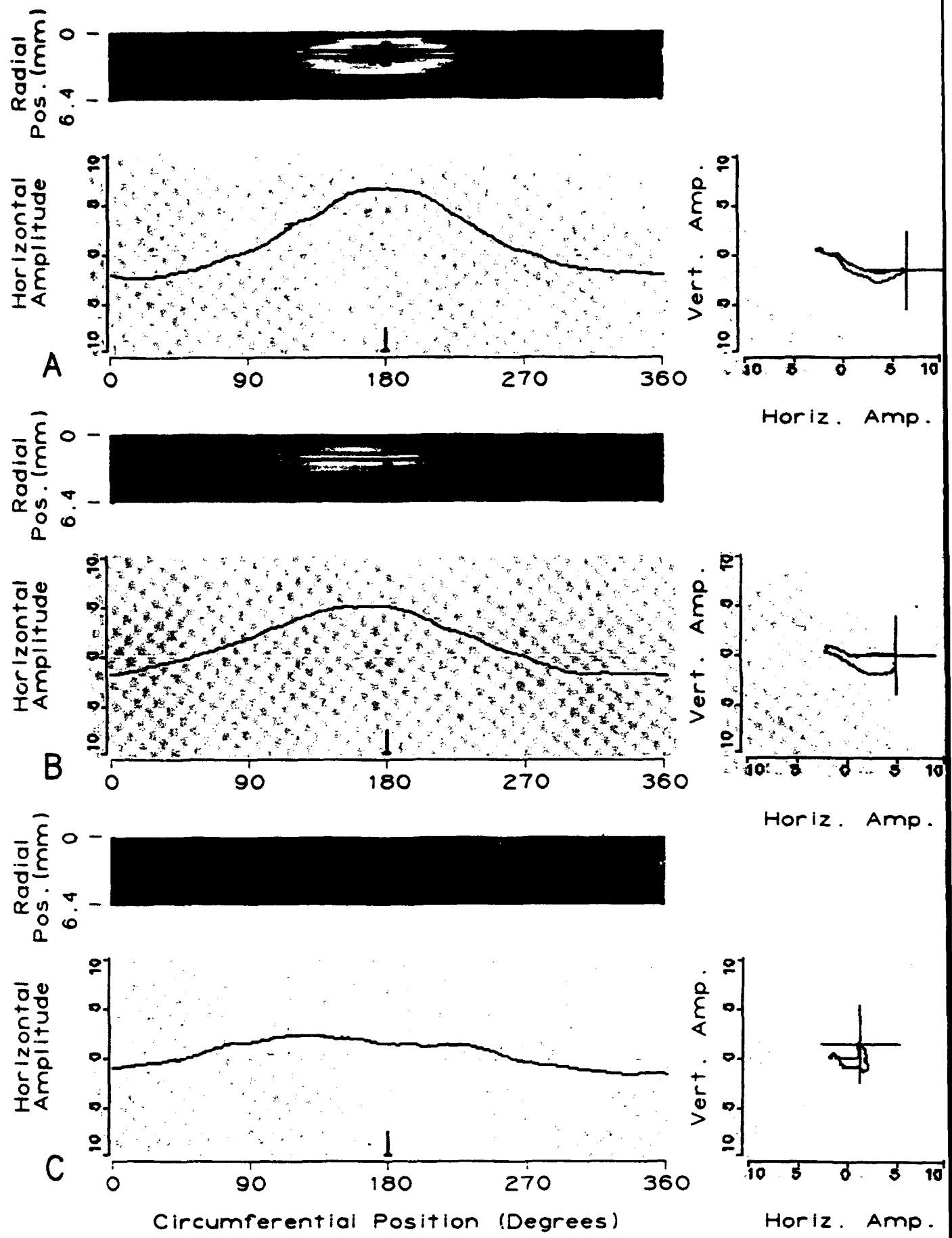
Figure 53. Data from specimen A with steel fasteners and second-layer edge at 180 degrees after two-frequency mixing: (A) hole 9 with 3.8-mm flaw at 180 degrees, (B) hole 10 with 2.5-mm flaw at 180 degrees, (C) hole 11 with edge only. Color scale: -4 to 11.
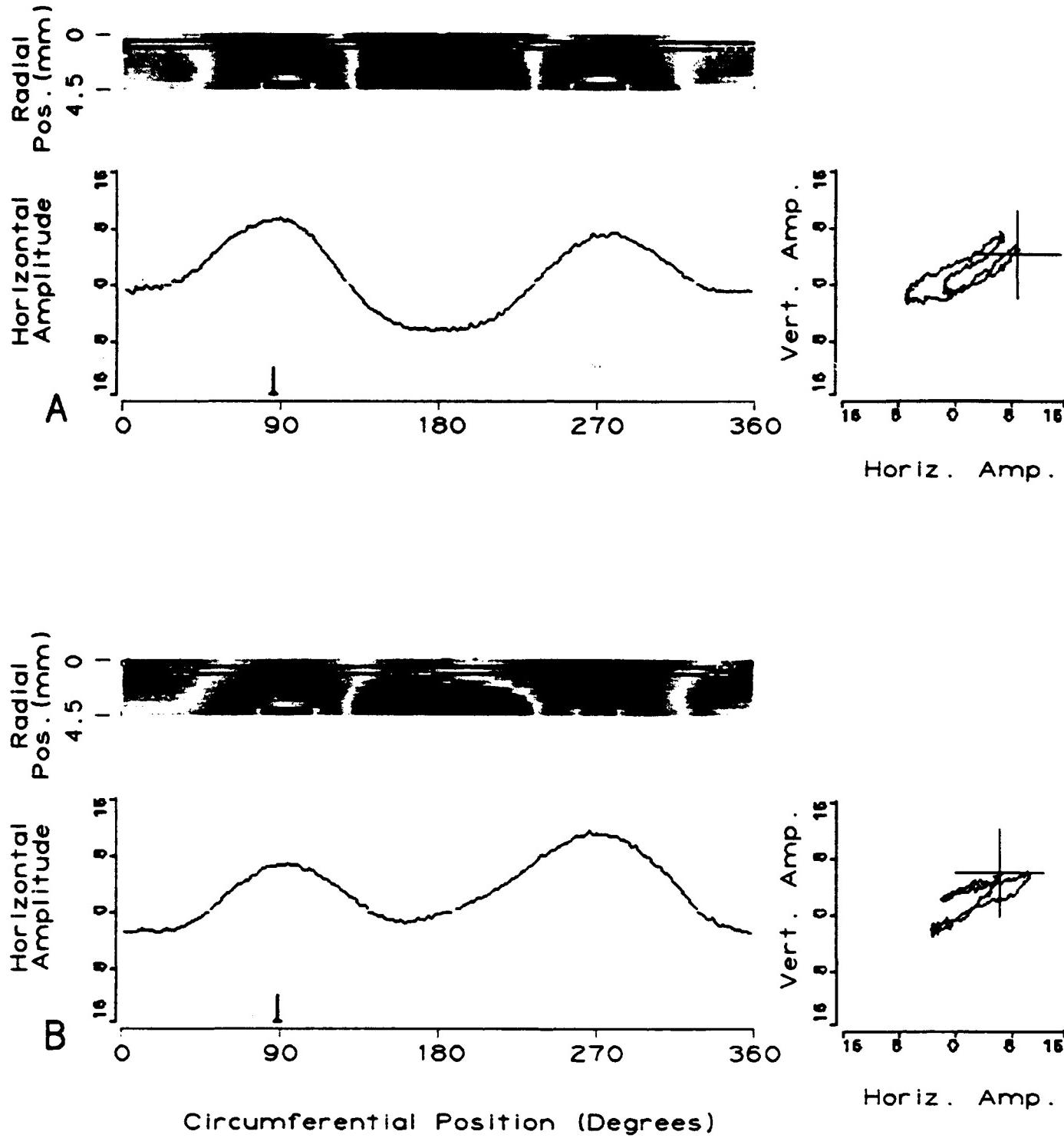
Figure 54. Data from specimen A3-19 with adjacent fasteners at 90 and 270 degrees: (A), (B), and (D) no flaws. (C) 2.6-mm crack in bottom surface of second layer at 180 degrees. Color scale: -16 to 13.

Figure 54 (Cont'd). Data from specimen A3-19 with adjacent fasteners at 90 and 270 degrees: (A), (B), and (D) no flaws. (C) 2.6-mm crack in bottom surface of second layer at 180 degrees. Color scale: -16 to 13..

(NOTE: COLOR COPY AVAILABLE FROM CONTRACTOR)

applied to all of the scans in the image, the variation in response from one scan to the next may be too large for a single mix to accommodate. A more effective approach may be to apply a separate mix to each scan and then to combine the result into a single image. This approach is more complex, but each mix would not have to accommodate the large variation from scan to scan.

(2) Specimen B3-20—Specimen B3-20 consisted of a 6.9-mm-thick first layer and a 4.5-mm-thick second layer. Hole 4 contained a 2.5-mm crack in the faying surface of the second layer. This hole and hole 3, which was unflawed, were scanned. The flaw was not apparent in the data. Possible reasons for lack of sensitivity to the flaw are the same as in the previous section, and also the first layer was thicker than in the SwRI specimens.

(3) Specimen B2-17—Specimen B2-17 had the same layer thicknesses as specimen B3-20, but the flaws were located in the first-layer countersink surface. Fig. 55 shows the data from hole 6, which contained a 2.5-mm crack. The crack was readily apparent as the very strong positive signal (distinct red region in the image) at 180 degrees. This was the smallest flaw in the specimen. This flaw was detected with both 250-Hz and 2-kHz excitation frequencies (2-kHz response shown in Fig. 55). Because the signal appears in the high-frequency response (where the second-layer flaw appeared at lower frequencies only), the flawed layer can be readily determined.

(4) Specimen A1-4—Specimen A1-4 contains a 0.71-mm crack in the faying surface of the first layer. This specimen was not scanned because it was not likely that the very small crack would be detected.

5.2.4   Linear Raster Scan with Cup-Core Probe—The linear raster scan approach is similar to the circumferential-radial scan, except that the probe is scanned linearly instead of circumferentially and indexed perpendicular, not radial, to the scan direction. The scans start at a position away from the fastener hole and are indexed so that they pass over the hole and finally to the opposite side. The advantage of this approach is that it is not necessary to align the scan with respect to the fastener hole.

With this scanning approach, a large signal is obtained when the probe scans over the fastener; and the fastener hole is very pronounced in the image. Flaw signals appear as a distortion in the shape of the pattern from the hole. Limited data were taken in order to demonstrate the feasibility of this approach.
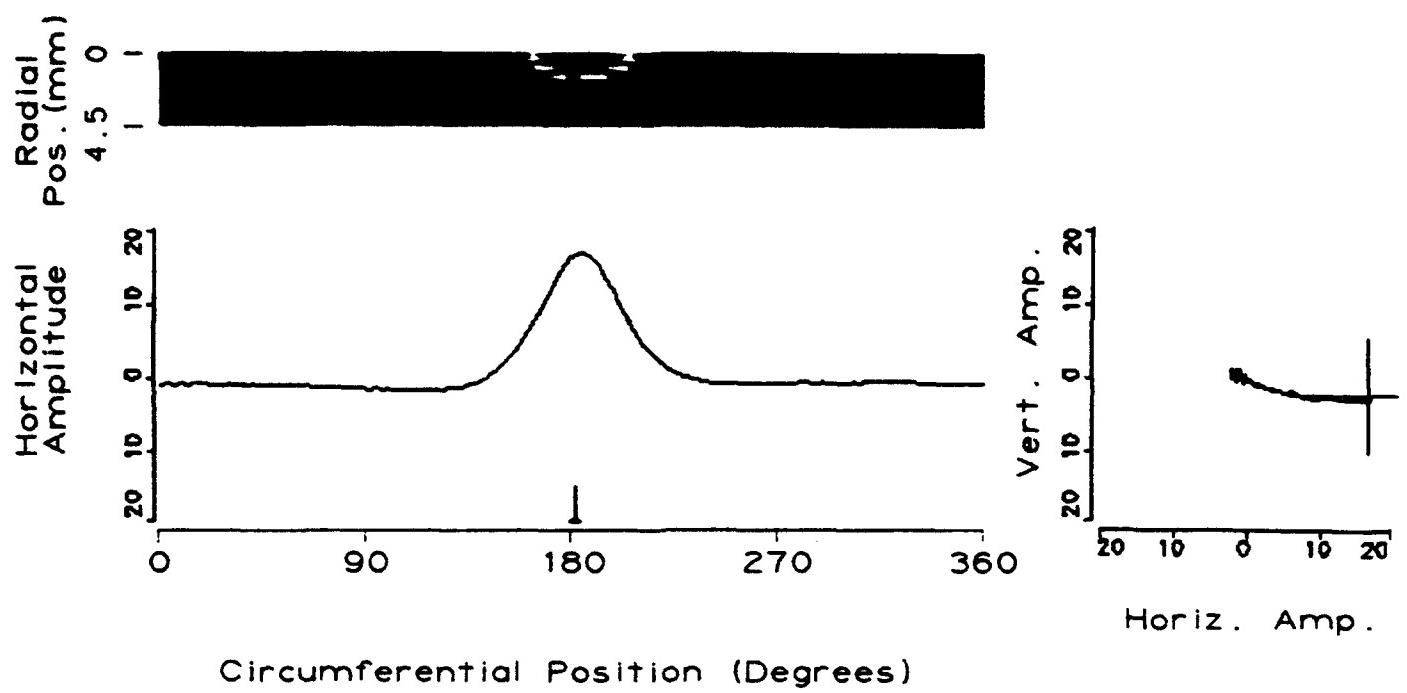
Figure 55. Data from hole 6 in specimen B2-17 with a 2.5-mm crack in the countersink surface of the first layer at 180 degrees. Color scale: -5 to 20.

(NOTE: COLOR COPY AVAILABLE FROM CONTRACTOR)

Fig. 56 shows images generated from a linear raster scan of the preliminary specimen, as shown in Fig. 31; the top layer thickness was 3.2 mm. The data were taken with excitation frequencies of 500 Hz and 2 kHz, and the data at these frequencies were mixed to reduce the effect of the edge and hole geometries. The image in Fig. 56(A) is from a fastener hole with a 5.2-mm flaw at the right side of the hole. The round spot in the image is from the response to the hole, and the bulging of the image to the right side is from the flaw. Figs. 56(B) and 56(C) are with a second-layer edge only and a second-layer edge plus the flaw. The edge shows up primarily as a band of dark blue, and the flaw causes a more pronounced bulging in the hole response, as shown in Fig. 56(C).

5.2.5   Summary of Test Results—An overall summary of the results obtained on the SwRI and WL/MLLP specimens is given in Table 2. The table gives the specimen and flaw characteristics for the tests performed and states the extent of flaw detectability. In most cases, the project goal of detecting a 2.5-mm second-layer flaw through a first-layer thickness of 6.4 mm was achieved. This included structure geometries containing second-layer edges, first-layer edges, adjacent fasteners, different fastener sizes, different flaw orientations around the hole, and fasteners of different materials (titanium and steel). In the case of a first-layer edge, where detection of a 2.5-mm flaw was marginal, a 3.8-mm flaw was readily detectable. In specimens supplied by WL/MLLP, where adjacent fasteners were spaced more closely, a 2.5-mm flaw was detected through a 4.5-mm first layer, although the response was dominated by signals from the adjacent fasteners. In this case, it was necessary to compare the signal pattern to those from other fasteners to determine the presence of the flaw. In a similar specimen with a 6.9-mm first layer, a 2.5-mm flaw was not detected. Also, a 2.5-mm first-layer flaw was detected.

A.   B.   C.
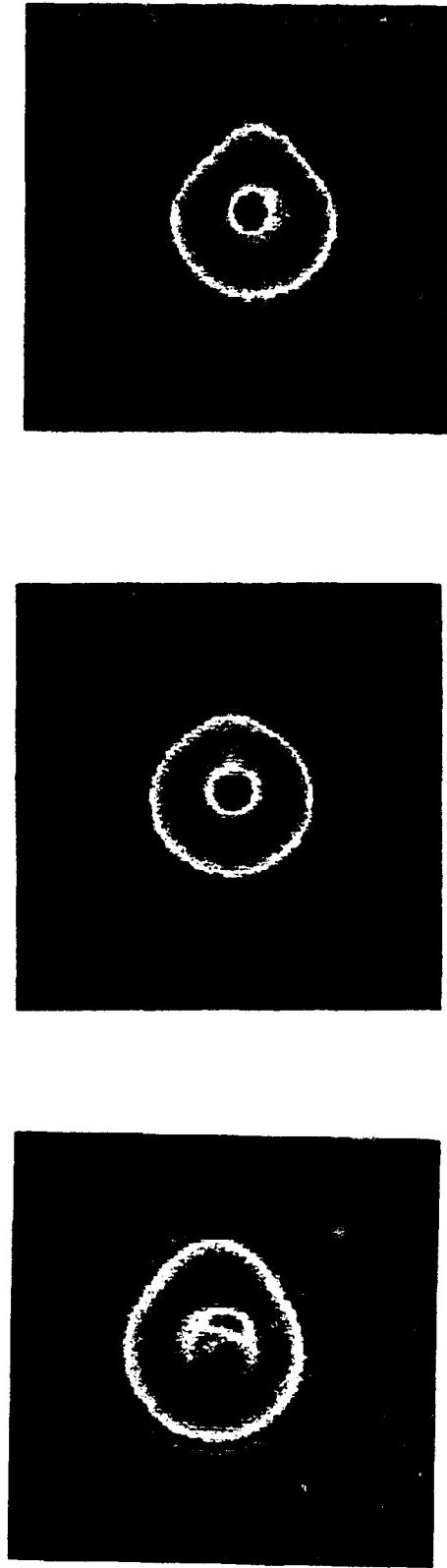
Figure 56. Images of mixed 500-Hz and 2-kHz data from linear raster scan for 3.2-mm first layer: (A) 5.2-mm flaw at right side of fastener hole; (B) edge at right side of fastener hole; (C) flaw and edge at right side of fastener hole. The images represent scans of a 5.1-cm-square region.

(NOTE: COLOR COPY AVAILABLE FROM CONTRACTOR)

82

TABLE 2. Summary of Test Results

CIRCUMFERENTIAL SCANS

Specimen	1st Layer Thickness	2nd Layer Thickness	Edge Location	Fastener-to-Edge Spacing	Fastener Size	Fastener Material	Fastener-to-Fastener Spacing	Flaw Orientation	Flaw Location	Flaw Type	Flaw Size	Flaw Detected*	Comments
A	6.4	6.4	2nd Layer	12.7	6.4	Ti	31.7	Toward Edge	2nd Layer	Notch	3.8 / 2.5	Y / Y	
A	6.4	6.4	2nd Layer	12.7	6.4	Steel	31.7	Toward Edge	2nd Layer	Notch	3.8 / 2.5	Y / Y	Required 2-frequency mix.
Prelim.	4.8	6.4	2nd Layer	12.7	6.4	Ti	---	Toward Edge	2nd Layer	Notch	5.2	Y	
A	6.4	6.4	2nd Layer	12.7	6.4	Ti	31.7	90° from Edge	2nd Layer	Notch	3.8 / 2.5	Y / Y	Response contains spurious signal of similar magnitude as flaw.
A	6.4	6.4	1st Layer	16.0	6.4	Ti	31.7	Toward Edge	2nd Layer	Notch	3.8 / 2.5	Y / M	
B	6.4	6.4	---	---	6.4	Ti	25.4	Toward Adjacent Fastener	2nd Layer	Notch	3.8	Y	
B	6.4	6.4	---	---	6.4	Ti	22.2	Toward Adjacent Fastener	2nd Layer	Notch	2.5	Y	
B	6.4	6.4	---	---	4.8	Ti	38.1	90° from Adjacent Fastener	2nd Layer	Notch	2.5	Y	
B	6.4	6.4	---	---	7.9	Ti	38.1	90° from Adjacent Fastener	2nd Layer	Notch	2.5	Y	
A3-19	4.0	2.5	1st and 2nd Layer	24.8	6.4	Ti	19.0	Toward Edge	2nd Layer Bottom Surface	Crack	2.6	M	Flaw signal present, but adjacent fastener signals dominate.
A1-4	4.0	2.5	1st and 2nd Layer	24.8	6.4	Ti	19.0	Toward Edge	1st Layer Faying Surface	Crack	0.71	See Comment	Specimen not scanned, but detection not probable.
B3-20	6.9	4.5	1st and 2nd Layer	24.8	6.4	Ti	19.0	Toward Edge	2nd Layer Faying Surface	Crack	2.5	N	
B2-17	6.9	4.5	1st and 2nd Layer	24.8	6.4	Ti	19.0	Toward Edge	1st Layer Countersink Surface	Crack	2.5	Y	Could be distinguished from 2nd layer flaw

LINEAR RASTER SCAN

Specimen	1st Layer Thickness	2nd Layer Thickness	Edge Location	Fastener-to-Edge Spacing	Fastener Size	Fastener Material	Fastener-to-Fastener Spacing	Flaw Orientation	Flaw Location	Flaw Type	Flaw Size	Flaw Detected*	Comments
Prelim.	3.2	6.4	2nd Layer	12.7	6.4	Ti	---	Toward Edge	2nd Layer	Notch	5.2	Y	

NOTES:
Dimensions are in mm.
Dimensions for fastener spacing are to fastener centerline.
*Y-Yes; M=Yes, but marginal; N=No

83

6. ADDITIONAL REQUIREMENTS FOR A FIELD INSPECTION SYSTEM

The breadboard system configured for use in this project consisted primarily of existing laboratory equipment, instrumentation, and computers and was not intended as a field-usable system. For the laboratory equipment to be developed into such a system, items such as the inspection scanning approach and procedures would need to be addressed as well as the components.

Two inspection modes were demonstrated: (1) a high-sensitivity mode that uses circumferential scans and (2) a lower sensitivity mode that uses linear raster scans. The circumferential mode could be used where a single scan is made at a fixed increment, but more information for discriminating between flaws and structure is obtained using two-dimensional scanning where circumferential scans are made at multiple radial positions. Circumferential scanning requires careful centering of the probe over the fastener, and can only scan a single fastener at a time. The linear mode requires only coarse positioning with the fastener located in a scan window and could allow scanning of several fasteners at a time.

A field system, therefore, could take any or all of the following forms, depending on the desired characteristics: (1) circumferential scanning with the probe at a single radial position, (2) circumferential scanning with radial incrementing, and (3) linear raster scanning. Regardless of the form, the system would consist of the following components: (1) probe, (2) mechanical scanner, and (3) instrumentation, which are described below.

6.1 PROBE

6.1.1 Circumferential Scan—The 85-degree segment probe design developed in this project would be used for both circumferential scan modes. For durability and protection, the probe would be potted in epoxy and mounted in a holder, which would attach to the scanner. This probe could be used for both nonmagnetic and magnetic fasteners, but it would be beneficial to investigate an improved probe design for magnetic fasteners that could possibly improve the centering capability.

6.1.2 Linear Scan—For the linear raster scan mode, the cup-core probe developed in this project would be used. A smaller version should also be designed to improve resolution. As with the segment probe, the probe would be potted in epoxy and mounted in a holder which would attach to the scanner.

6.2 MECHANICAL SCANNER

6.2.1 **Circumferential Scan**—A motor-driven, rotating probe head for circumferentially scanning the probe would be necessary. For the single-scan mode, the probe would be mounted at a fixed radius. For multiple scans at different radii, a mechanism would be needed to place the probe at a fixed radius (while scanning circumferentially) for centering and then to scan circumferentially for one revolution at a given radius, increment to a new radius and scan for one revolution, and repeat the process for up to 10 different radii. This could be accomplished with a cam-type arrangement; the cam would be disengaged for the centering operation and then engaged to perform the radial incrementing.

6.2.2 **Linear Scan**—The linear scan would require a scanning system to perform a linear raster scan; that is, the probe would be scanned linearly and incremented in the transverse direction. A small scanner could be developed to perform this motion over an area of several square inches; it would be interchangeable with the instrumentation for the circumferential scan.

An alternate approach that, in concept, appears very attractive for implementing the linear scan would be to use the McDonnell Douglas MAUS III system which is currently being developed for WL/MLLP. The MAUS III has a hand-held scanner, which is moved forward manually and provides a side-to-side linear probe motion; the result is a linear raster scan. An eddy current probe (such as the linear-scan cup-core probe developed in this project) could be readily mounted on the scanner. Also, the system contains eddy current instrumentation and signal-processing capability, which provide a color image of the scan area in a similar format as used in this project. Provided that the eddy current instrumentation and signal-processing capability of the MAUS III is compatible with the second-layer requirements, it should be relatively straightforward to use this system as a platform for second-layer inspection.

6.3 INSTRUMENTATION

The same instrumentation would be applied to the circumferential and linear-scan inspections. The instrumentation would consist of multifrequency eddy current instrumentation (frequency range of 250 Hz to 5 kHz) capable of reflection coil operation, preamp for the sensor-coil signal, analog-to-digital converter, and notebook-type computer. A breadboard system capable of field use could be configured primarily from off-the-shelf instrumentation for additional testing, as described in the recommendations section.

6.4 REQUIREMENTS FOR TITANIUM SKIN INSPECTION

Inspection of titanium alloy aircraft skin (as opposed to the 7075-T6 aluminum alloy tested in this project) would require adjustments because of the much lower conductivity of the titanium (about a factor of 30). To maintain the same skin depths as in the aluminum, the excitation frequencies must be increased by about a factor of 30. The same probe configurations could be used, but the coils would require redesigning for the higher frequency.

One factor could change the current distribution around the fastener somewhat and, thus, possibly alter the flaw and structure responses. This factor is associated with the conductivity of the skin compared to that of the fastener. For aluminum skin and a titanium fastener, the current would tend to flow in the aluminum (where the flaw is located) instead of in the fastener because its conductivity is much higher than that of the fastener. This can be seen in the modeling results in this report. For the case of titanium skin and a titanium fastener, both materials have the same conductivity; thus the current would not flow preferentially in the skin. More current may flow in the fastener, however; and the current density in the flaw region may be reduced—possibly resulting in a reduced response from the flaw. Some additional study would be needed to determine the severity of this effect.

7. CONCLUSIONS

(1) The best flaw detection and discrimination among flaws and structure was obtained using an 85-degree segment probe with an air-core sensor positioned next to the exciter outer leg and oriented to detect the magnetic-field component vertical to the specimen surface.

(2) Although chirp excitation was shown to be viable, it did not offer significant advantages over multiple, discrete frequency excitation, which allowed simpler instrumentation and signal analysis.

(3) Two-dimensional scanning using circumferential scans around the fastener and increments in the radial direction, combined with color imaging of the data, improved discrimination between flaws and structure. This approach takes advantage of the capability of the human eye to recognize patterns from flaw and defect signals.

(4) Although two-dimensional scanning is the preferred scan mode and provides more spatial information to help distinguish flaws and structure, flaw detection can also be accomplished using only a single circumferential scan at a fixed radius and examining the "strip-chart" presentation of the signal. The optimum radius for a single scan was shown to be with the center leg of the probe moved somewhat off the fastener centerline.

(5) In the breadboard evaluation, the project goal of detecting a 2.5-mm second-layer flaw through a first-layer thickness of 6.4 mm was achieved in eight of the nine specimen configurations (with this layer thickness) evaluated. The evaluation included structure geometries containing second-layer edges, first-layer edges, adjacent fasteners, different fastener sizes, different flaw orientations around the hole, and fasteners of different materials (titanium and steel). In the case of a first-layer edge, where detection of a 2.5-mm flaw was marginal, a 3.8-mm flaw was readily detectable. In additional specimens supplied by WL/MLLP, where adjacent fasteners were spaced more closely, a 2.5-mm crack was detected through a 4.5-mm first layer by comparing the signal patterns from adjacent holes. This was necessary because of the strong signals from adjacent fasteners. In a similar specimen with a 6.9-mm first layer, a 2.5-mm flaw was not detected. Also, a 2.5-mm first-layer flaw was detected.

(6) Limited data taken with a symmetrical, cup-core probe using linear raster scans and color imaging showed the potential for a rapid inspection that requires essentially no probe alignment, except to position the fastener within the scan window. Although raster scanning may not achieve the same sensitivity as circumferential scanning, this approach would provide a much simpler and faster inspection.

8. RECOMMENDATIONS

(1) Validate the circumferential scan technique on a larger specimen set consisting of actual aircraft structure. This will allow additional verification of the technique before development into an actual inspection system. The validation could be accomplished in the laboratory with the existing breadboard using small specimens cut from aircraft structure or Air Force NDI test specimens representative of different aircraft structure. Alternately, a portable scanning head for the breadboard system could be developed and used on larger specimens and on actual aircraft.

(2) Develop a smaller probe that would provide higher resolution and sensitivity for the linear raster scan approach. Because only limited effort was devoted to design of this probe, a revised design should provide improved results.

(3) Investigate the feasibility of combining the linear raster scan technology developed in this program with the McDonnell Douglas MAUS III system (currently being developed for WL/MLLP). This system could provide the mechanical scanning, and possibly the instrumentation, needed to implement a high-speed second-layer inspection.

(4) Develop an improved multifrequency mixing approach, possibly using a separate mix for each scan radius, to better remove the signals from adjacent first-layer structure such as edges and adjacent fastener holes.

(5) Investigate an improved probe design for magnetic fasteners. The approach would be to reduce the amount of magnetic flux that is induced in the fastener so that variations in fastener response have a reduced effect on the EC signal.

(6) Determine the aircraft and structures requiring second-layer inspection and determine where the technology developed in this project could be applied.

9. REFERENCES

1. Beissner, R. E., and Fisher, J. L., "Use of a Chirp Waveform in PUlsed Eddy Current Crack Detection," in Review of Progress in Quantitative NDE, Volume 6A (D. O. Thompson and D. E. Chimenti, eds.), (Plenum Press, New York, 1987), pp. 467-472.

2. Fisher, J. L., and Beissner, R. E., "Pulsed Eddy Current Crack Characterization Experiments," in Review of Progress in Quantitative NDE, Volume 5 (D. O. Thompson and D. E. Chimenti, eds.), (New York, Plenum Press, 1986), pp. 199-206.

3. Henning, H. F., Nonsinusoidal Waves in Radar and Radio Communication (Academic Press, New York, 1981).

APPENDIX

Description of WL/MLLP Specimens A1-4, A3-19, B2-17, and B3-20

SPECIMEN IDENTIFICATION

XX XX

— Specimen Number

— Cracked Surface

1. Top Sheet, Faying
   Surface

2. Top Sheet, CSK Surface

3. Bottom Sheet, Outside
   Surface (for Combination
   A)

   Bottom Sheet, Faying
   Surface (for thickness
   Combination B)

4. Bottom Sheet, Faying
   Surface (for thickness
   Combination A)

   Bottom Sheet, Outside
   Surface (for thickness
   Combination B)

5. No Cracks

— Thickness Combination

A. Top Sheet = 0.156 = t_1

   Bottom Sheet = 0.100 = t_2

B. Top Sheet = 0.270 = t_1

   Bottom Sheet = 0.176 = t_2

HOLE
NUMBERS

TOP SHEET
COUNTERSUNK

BOTTOM
SHEET

SPECIMEN
IDENTIFICATION

FIGURE 1.   SPECIMEN CONFIGURATION

KEY TO CODES IN TABLES I AND II

X.XXXX

— L – Left Side of Hole
  Cracked

— R – Right Side of Hole
  Cracked

— Crack Length, Inch

S – Hole Contains Steel Fastener

TABLE A-1

CRACK LENGTH AND CRACK LOCATION AND STEEL FASTENER LOCATION DATA FOR NDI STANDARDS
HAVING 0.100-INCH AND 0.156-INCH THICKNESS COMBINATION

SPECIMEN IDENTIFICATION	CRACK LENGTH AND CRACK LOCATION AND STEEL FASTENER LOCATION AT HOLE NUMBER									
	1	2	3	4	5	6	7	8	9	10
A1-1			0.036R	S	0.038L					
A1-2 * M		0.029L	0.032L			S			0.027L	
A1-3 * O								0.027L	0.030R	
A1-4	0.028R	S								S
A1-5					0.027R				0.029L	S
A1-6		S	0.050L		0.049L		0.046L			
A1-7			S		0.046R			0.048R		
A1-8 * M				0.050L						S
A1-9 * M	0.052L		S					0.047L		S
A1-10						0.052R			0.049L	
A1-11	S						0.070L			
A1-12	S		0.062R	0.073L						S
A1-13 * M		0.067L	0.068R				0.071L			
A1-14	S	0.069R		0.074R			0.065L			S
A1-15 * M						0.073R				S
A1-16	S		0.110R			0.107L		0.102L		
A1-17		S		0.104R		0.110R				
A1-18 * M	S		0.096L		0.100L	0.101L				
A1-19 * M		S		0.098L						
A1-20									0.098L	S
A1-21	S			0.120R		0.120L		0.117L		
A1-22 * M			0.125L			0.120L				
A1-23 * M		S	0.115L							0.120L

TABLE A-1 (cont'd)

CRACK LENGTH AND CRACK LOCATION AND STEEL FASTENER LOCATION DATA FOR NDI STANDARDS
HAVING 0.100-INCH AND 0.156-INCH THICKNESS COMBINATION

SPECIMEN IDENTIFICATION	CRACK LENGTH AND CRACK LOCATION AND STEEL FASTENER LOCATION AT HOLE NUMBER									
	1	2	3	4	5	6	7	8	9	10
A2-17* M							0.100L			0.102L
A2-18	S	S				0.092L		0.095L	S	0.092R
A2-19			0.107R			0.100R			0.101R	
A2-20	S									S
A3-1	0.030L				0.029R					
A3-2*			0.030R			S		0.030R		
A3-3*			0.029R			S				
A3-4*	0.029R		0.031L		S					
A3-5						0.026L		0.029R	S	0.030L
A3-6		0.054L			S		0.049R			
A3-7*					S			0.051L	0.049L	
A3-8*									0.050L	
A3-9	0.057L	S		0.046R			0.056L			
A3-10	S		0.051R					0.048R		
A3-11	S					S		0.064R		0.065R
A3-12*		0.072R							0.071L	
A3-13*	0.068L					0.071R				
A3-14	S		0.065R				S			
A3-15		0.079R			0.069R				0.071L	
A3-16				0.097R		0.103L		S		S
A3-17	0.112R			0.094L			0.105R			S
A3-18* M								S		0.105R
A3-19			0.100L			0.101L		0.101L	S	

94

CRACK LENGTH AND CRACK LOCATION AND STEEL FASTENER LOCATION DATA FOR NDI STANDARDS
HAVING 0.175-INCH AND 0.270-INCH THICKNESS COMBINATION

SPECIMEN IDENTIFICATION	1	2	3	4	5	6	7	8	9	10
B1-25			0.128L		B		0.114W			
B1-26	S		0.142R							
B1-27		S		0.158L				0.145R		
B1-28			S	0.138R	0.195R			0.148L		
B1-29				0.138R	0.145R	S				
B1-30				0.165L	S	0.153R			0.142R	
B2-1		0.030R					0.028L			
B2-2 ✩		S		S	0.029L	0.030L	0.028L		0.028L	
B2-3	0.031L									S
B2-4 ✩	0.034L	S				0.028L	0.028L			
B2-5				S		0.030R			0.029L	
B2-6			0.054L		0.048R		S			
B2-7 ✩							0.049L	0.049R		S
B2-8		S				0.049R		S		
B2-9		S			0.048L					
B2-10		0.057R	0.051R					S		0.051R
B2-11		S	0.069R				S			
B2-12				0.074R	0.063L	0.069R			0.080L	
B2-13	0.072L				S				0.068R	S
B2-14				0.071L	0.070R		S			
B2-15					S	0.100W	S			0.071R
B2-16		0.099L				0.100N		/	S	
B2-17				S		0.097L	0.096L		S	
B2-18			0.095L	S			S	S		0.100L
B2-19	0.026R		0.095L							

95

TABLE A-2 (cont'd)

CRACK LENGTH AND CRACK LOCATION AND STEEL FASTENER LOCATION DATA FOR NDI STANDARDS HAVING 0.176-INCH AND 0.270-INCH THICKNESS COMBINATION

SPECIMEN IDENTIFICATION	CRACK LENGTH AND CRACK LOCATION AND STEEL FASTENER LOCATION AT HOLE NUMBER									
	1	2	3	4	5	6	7	8	9	10
B3-14 *				0.069R			S			
B3-15 *		0.105L			0.073R	S	0.072L		0.069R	
B3-16 *								S	S	
B3-17			0.096L			0.099R			0.095L	
B3-18 *			0.099R		S			0.096R		0.096L
B3-19 *						S				
B3-20 *				0.099R		S		0.099R		0.096R
B3-21		0.127L		S	0.117L		0.121L			
B3-22 *		0.124L			S		S			
B3-23 *	0.125L	0.122R						0.122L		
B3-24 *		S				0.118R				
B3-25 *		S				0.119R		0.124R		
B3-26			S			0.158R		0.142L		
B3-27			S	S			0.146L	0.145L		
B3-28				0.146L		0.152R				
B3-29				S	0.147R	0.149R	S			
B3-30			0.143R					0.031L		
B4-1					S	S	S			
B4-2	0.028R	0.030R				S				
B4-3		0.027L	S				0.027L			
B4-4		0.029L	0.032L		0.028R					
B4-5		0.029R			S		0.031L			
B4-6		0.050R			S	0.055R				
B4-7	0.059R		0.040L							

96

TABLE A-2 (cont'd)

CRACK LENGTH AND CRACK LOCATION AND STEEL FASTENER LOCATION DATA FOR NDI STANDARDS HAVING 0.176-INCH AND 0.270-INCH THICKNESS COMBINATION

SPECIMEN IDENTIFICATION	CRACK LENGTH AND CRACK LOCATION AND STEEL FASTENER LOCATION AT HOLE NUMBER									
	1	2	3	4	5	6	7	8	9	10
B5-1										8
B5-2						8				
B5-3					8			8		
B5-4							8			
B5-5										

B5-6 thru 15 (10 extra)

*Completed first batch before modified assembly procedure.

97